

# Materials Science & Engineering A

## The complex interaction between microstructural features and crack evolution during cyclic testing in heat-treated Al-Si-Mg-Cu cast alloys

--Manuscript Draft--

<b>Manuscript Number:</b>	MSEA-D-21-01066R4
<b>Article Type:</b>	Research Paper
<b>Keywords:</b>	aluminium alloys; electron microscopy; characterisation; casting methods; fatigue
<b>Corresponding Author:</b>	Toni Bogdanoff Jönköping University: Jonkoping University Jönköping, SWEDEN
<b>First Author:</b>	Toni Bogdanoff
<b>Order of Authors:</b>	Toni Bogdanoff Lucia Lattanzi Mattia Merlin Ehsan Ghassemali Anders E.W. Jarfors Salem Seifeddine
<b>Abstract:</b>	<p>The study aimed to investigate crack initiation and propagation at the micro-scale in heat-treated Al-7Si-Mg cast alloys with different copper (Cu) contents. In-situ cyclic testing in a scanning electron microscope coupled with electron back-scattered diffraction and digital image correlation was used to evaluate the complex interaction between the crack path and the microstructural features. The three-nearest-neighbour distance of secondary particles was a new tool to describe the crack propagation in the alloys. The amount of Cu retained in the <math>\alpha</math>-Al matrix after heat treatment increased with the Cu content in the alloy and enhanced the strength with a slight decrease in elongation. During cyclic testing, the two-dimensional (2D) crack path appeared with a mixed propagation, both trans- and inter-granular, regardless of the Cu content of the alloy. On fracture surfaces, multiple crack initiation points were detected along the thickness of the samples. The debonding of silicon (Si) particles took place during crack propagation in the Cu-free alloy, while cracking of Si particles and intermetallic phases occurred in the alloy with 3.2 wt.% Cu. Three-dimensional tomography using focused ion beam revealed that the improved strength of the <math>\alpha</math>-Al matrix changes the number of cracked particles ahead of the propagating crack with Cu concentration above 1.5 wt.%.</p>

Toni Bogdanoff  
Jönköping University  
Gjuterigatan 5  
55318 Jönköping, Sweden  
+46 722066640  
Toni.Bogdanoff@ju.se

Professor E. J. Lavernia  
Editor-in-chief  
*Materials Science and Engineering A*

Jönköping, 23 February 2021

Dear Professor Lavernia

I am pleased to submit an original research article entitled "The complex interaction between the microstructure feature on the crack initiation and propagation in a heat-treated Al-Si-Mg-Cu alloys" by Toni Bogdanoff, Lucia Lattanzi, Mattia Merlin, Ehsan Ghassemali, Anders E.W. Jarfors, Salem Seifeddine for consideration for publication in the *Materials Science and Engineering A* journal. We previously investigated the addition of Cu to Al-Si-Mg alloys and this manuscript builds on our recent work to investigate the role of microstructure in the as-cast condition.

In this manuscript, we provide new insight into the influence of microstructure on crack nucleation and propagation in Cu-added AlSi7Mg alloys after heat treatment. The results from *in-situ* cyclic tests in the scanning electron microscope (SEM) coupled with digital image correlation (DIC) are deepened further with 3D tomography with focused ion beam (FIB) milling. The latter enables to investigate the volume of material involved in crack propagation and gives a three-dimensional insight. These additional results enable to improve the two-dimensional observation of polished surfaces.

We believe that this manuscript is appropriate for publication by *Materials Science and Engineering A* because it characterises the relation between the microstructure of the alloy and its mechanical properties. Furthermore, the innovative experimental procedures employed are versatile for the study of different alloys.

This manuscript is original and is not under consideration for publication elsewhere. We have no conflict of interest to disclose.

Thank you for your consideration.

Best regards,

Toni Bogdanoff  
Department of Materials and Manufacturing  
Jönköping University

E-mail addresses

Lucia Lattanzi: [lucia.lattanzi@ju.se](mailto:lucia.lattanzi@ju.se)

Mattia Merlin: [mattia.merlin@unife.it](mailto:mattia.merlin@unife.it)

Ehsan Ghassemali: [ehsan.ghassemali@ju.se](mailto:ehsan.ghassemali@ju.se)

Anders E.W. Jarfors: [anders.jarfors@ju.se](mailto:anders.jarfors@ju.se)

Salem Seifeddine: [salem.seifeddine@ju.se](mailto:salem.seifeddine@ju.se)

Reply to reviewers' comments

The authors gratefully acknowledge the reviewers for their time and for their valuable comments to improve the manuscript. Detailed responses to the comments are reported below for Reviewer 4.

**Reviewer #4**

The authors revised the manuscript based on the previous comments. The manuscript looks good and could be considered for publication in MSEA.

The authors gratefully acknowledge your time and effort for reviewing the manuscript.

Minor comments:

A. Authors should check the manuscript for English grammar errors and/or for repeating usage of some expressions

The manuscript was revised accordingly and updated where possible.

1. Line 29 (grammar was/were)

"The three-nearest-neighbour distance of secondary particles was a new tool to describe the crack propagation in the alloys."

2. Line 36-37 – occurred

"The debonding of silicon (Si) particles took place during crack propagation in the Cu-free alloy, while cracking of Si particles and intermetallic phases occurred in the alloy with 3.2 wt.% Cu."

3. Lines 68-70 – because

"Peak ageing generally occurs within the transition from coherent to semi-coherent precipitates when the optimal number density combined with optimal precipitate spacing is reached [18]."

4. Line 81 – increase

"A higher Cu/Mg ratio by increasing Cu content improves both strength and elongation."

5. Line 149 - "measure alloying elements"

"Electron Back-Scattered Diffraction (EBSD - Hikari Plus, Eden Instruments), Wavelength Dispersive X-ray Spectroscopy (WDS - Teks HP, Edax), and Energy Dispersive X-ray Spectroscopy (EDS - Octane Pro, Edax) were employed in a SEM (Lyra3, Tescan) to determine the AGS, quantify the element composition in the primary  $\alpha$ -Al matrix, and identify the secondary phases, respectively."



6. Line 164 - STRENGTH (?) of Al matrix

"The influence of Cu on the  $\alpha$ -Al matrix strength was also assessed using Vickers microhardness (HV0.01) measurements (FM-110, Future Tech Corp)."

7. Lines 187-188 – tested

"Two samples of each alloy were tested, and one extra sample of Alloys Cu 0 and Cu 3.0 was investigated for Focused Ion Beam (FIB) slicing."

8. Line 292 started

"Figure 6g-h shows that the nucleation sites were observed at the grain boundaries (dashed yellow lines, over-imposed from the EBSD maps) in Alloy Cu 3.0."

9. Lines 400-401 (grammar)

"These insights on crack propagation from subsurface material also support the appearance of the secondary cracks visible in Figure 8b."

10. Lines 416-417 (grammar)

"This outcome aligns with the FIB sections in Figures 10 and 11, which showed cracks originating in the subsurface area."

B. The reference for lines 136-138 is missing

Added reference [5].

C. Figs 2,5,9: the color used for as-cast condition looks too pale on black/white printing

We have updated figures 2, 5, and 9.

But I still have one non-critical concern about the content of the manuscript. The authors few times mentioned the "strengthening role/effect" of "retained" Cu in Al matrix, which was not properly studied here. The effect is referred to microstructural features, which "were not observed and need different investigation approach" (lines 299-300). Those features are coherent or semi-coherent precipitates, their amount and density indeed define a strength of Al matrix. It is understandable that in as-cast Al alloys coherent and semi-coherent precipitates are often ignored due to small dimensions. However in scientific work I usually expect (or hope) that the authors pay more attention on tiny precipitates, especially when in summary they wrote that this study "provides a deeper understanding of relationships between crack development and microstructure features"

Thank you for your valuable comment; we agree that sub-micron precipitates influence the strength of the Al matrix. Studying the effect of these precipitates on the cracking behavior of Al

cast alloys is an interesting research objective that is required to be studied using other techniques such as in-situ TEM. However, in the present study, the main goal was focused on the micro-scale features and their effect on cracking behavior during cyclic loading. The strengthening role of sub-micron precipitates in Al-Si-Cu alloys is well known and reported in the literature (some of the more recent references 12-14), which is strengthening the matrix, by which the crack propagation during loading could be affected. We are thankful for this insightful comment and consider it for future work to look at the effect of sub-micron microstructural features on cyclic crack initiation and propagation. To clarify this fact, at the end of the introduction, we updated:

Line 119-122: "To the best of the knowledge of the authors, no similar detailed investigations have been performed to evaluate the crack propagation at the micro-scale level on the heat-treated Cu-added Al-Si-Mg alloys during cyclic loading."

The abstract was also slightly adjusted to highlight the study at the micro-scale.

1 **The complex interaction between microstructural features and crack**  
2 **evolution during cyclic testing in heat-treated Al-Si-Mg-Cu cast alloys**

3 Toni Bogdanoff <sup>a</sup>, Lucia Lattanzi <sup>a,b</sup>, Mattia Merlin <sup>b</sup>, Ehsan Ghassemali <sup>a</sup>, Anders E.W. Jarfors

4 <sup>a</sup>, Salem Seifeddine <sup>a</sup>

5 <sup>a</sup> Department of Materials and Manufacturing, Jönköping University, Box 1026, 55111 Jönköping,

6 Sweden

7 <sup>b</sup> Department of Engineering, University of Ferrara, Via Giuseppe Saragat 1, 44122 Ferrara, Italy

8 Corresponding author: Toni Bogdanoff, +46 722066640

9 Email addresses: toni.bogdanoff@ju.se (T. Bogdanoff), lucia.lattanzi@ju.se (L.

10 Lattanzi), mattia.merlin@unife.it (M. Merlin), ehsan.ghassemali@ju.se (E.

11 Ghassemali), anders.jarfors@ju.se (A. Jarfors), salem.seifeddine@ju.se (S. Seifeddine)

12

13

14

15

16

17

18

19

20

21

22

23 **ABSTRACT**

24 The study aimed to investigate crack initiation and propagation [at the micro-scale](#) in  
25 heat-treated Al-7Si-Mg cast alloys with different copper (Cu) contents. In-situ cyclic  
26 testing in a scanning electron microscope coupled with electron back-scattered  
27 diffraction and digital image correlation was used to evaluate the complex  
28 interaction between the crack path and the microstructural features. The three-  
29 nearest-neighbour distance of secondary particles [was a new tool](#) to describe the  
30 crack propagation in the alloys. The amount of Cu retained in the  $\alpha$ -Al matrix after  
31 heat treatment increased with the Cu content in the alloy and enhanced the strength  
32 with a slight decrease in elongation. During cyclic testing, the two-dimensional (2D)  
33 crack path appeared with a mixed propagation, both trans- and inter-granular,  
34 regardless of the Cu content of the alloy. On fracture surfaces, multiple crack  
35 initiation points were detected along the thickness of the samples. The debonding of  
36 silicon (Si) particles [took place](#) during crack propagation in the Cu-free alloy, while  
37 cracking of Si particles and intermetallic phases occurred in the alloy with 3.2 wt.%  
38 Cu. Three-dimensional tomography using focused ion beam revealed that the  
39 improved strength of the  $\alpha$ -Al matrix changes the number of cracked particles ahead  
40 of the propagating crack with Cu concentration above 1.5 wt.%.

41

42 **Keywords:** aluminium alloys; electron microscopy; characterisation; casting  
43 methods; fatigue.

44

## 45 1. INTRODUCTION

46 Nowadays, the automotive sector strives for lightweight solutions for reducing gas  
47 emissions and fuel consumption [1-2]. Besides, the components of electric vehicles  
48 must meet additional requirements regarding reduced weight and optimised  
49 mechanical performance. For these reasons, it is crucial to perfectly match the  
50 selection of materials to the operational life of components [3]. Hypoeutectic Al-Si  
51 cast alloys are a valid candidate for fulfilling these requirements, particularly with  
52 the right combination of alloying elements, such as magnesium (Mg) and copper  
53 (Cu), and post solidification treatments. The addition of Mg and Cu combined with  
54 proper heat treatment provides a good compromise between the ductility of Al-Si-  
55 Mg alloys and the strength of Al-Si-Cu systems [4-6]. For this reason, over the last  
56 two decades, the literature has addressed the addition of Cu to Al-Si-Mg cast alloys  
57 for both as-cast [4-7] and heat-treated conditions to obtain high strength [8-19].  
58 The T6 heat treatment is typically applied to Al-Si-Mg and Al-Si-Cu-Mg alloys and  
59 consists of solution treatment, quenching, and ageing. These steps lead to dispersed  
60 precipitates that hinder dislocation movements and improve the strength of the  
61 material. In Al-Si-Mg alloys, the precipitation sequence during ageing results in an  
62 incoherent  $\beta$ -Mg<sub>2</sub>Si phase [17]. The addition of Cu changes the precipitation  
63 sequence of the alloy, inducing Cu-based precipitates, as reported in the literature  
64 [12-14]. For a Cu content greater than 1.5 wt.%, the incoherent  $\theta$ -Al<sub>2</sub>Cu phase ends  
65 the precipitation sequence and suppresses the  $\beta$ -Mg<sub>2</sub>Si phase [17]. The strength  
66 improvement is due to a sufficient number of precipitates of appropriate size and

67 spacing. Peak ageing generally occurs within the transition from coherent to semi-  
68 coherent precipitates **when** the optimal number density combined with optimal  
69 precipitate spacing **is reached** [18]. Natural ageing before artificial ageing is  
70 beneficial for Al-Si-Mg alloys because it promotes a microstructure with a lower  
71 number density of coarser particles compared to the directly artificially aged alloy  
72 [18,19].

73 As a consequence of heat treatment, the addition of Cu improves the Yield Strength  
74 (YS) and Ultimate Tensile Strength (UTS) of Al-Si-Mg alloys. Caceres *et al.* [16]  
75 investigated the influence of Si, Cu, and Mg on the tensile properties of heat-treated  
76 Al-Si-Mg-Cu systems. They concluded that to achieve the optimal mechanical  
77 response, Cu content should be limited to 3 wt.% when Mg content is above 1 wt.%.  
78 Zheng *et al.* [15] investigated Al-6Si-Cu-Mg alloys with Cu/Mg ratios from 1 to 4.  
79 They reported that the precipitation sequence depends on the Cu content and the  
80 Cu/Mg ratio: a low-ratio alloy tends to preferentially form the precursor of  $\beta$   
81 precipitates, whereas a high-ratio alloy will lead to the formation of Q and  $\theta$   
82 precursors. **A higher Cu/Mg ratio** by increasing Cu content improves both strength  
83 and elongation.

84 The effect of T6 heat treatment also influences the fatigue response of the material. In  
85 particular, crack propagation is characterised by significantly more branching and  
86 crack deflection compared to the as-cast condition due to crack-tip shielding and  
87 lower crack growth rates [20]. For this reason, Lados *et al.* [21-23] have been focusing  
88 their attention on the influence of microstructural features on long and small fatigue

89 crack growth in heat-treated Al-Si-Mg alloys. About the  $\alpha$ -Al matrix strength, they  
90 reported that the crack growth rate is higher for naturally-aged samples than for T6  
91 ones in upper Region II and lower Region III of the Paris curve. On the other hand,  
92 in upper Region III, naturally-aged material showed improved fatigue crack growth  
93 resistance due to the ductile tearing in the  $\alpha$ -Al matrix.

94 From this background, an in-depth understanding of crack initiation and  
95 propagation on the microstructural scale is crucial for developing high-performance  
96 alloys, especially for the transportation sector. In addition, structural components  
97 like suspension systems must withstand dynamic loading [24-26], and it is crucial to  
98 assess the role of the heat-treated microstructure in either promoting or shielding  
99 crack propagation.

100 The present work aimed to identify the microstructural features that significantly  
101 influence the crack initiation and propagation of a Cu-added Al-7Si-Mg alloy after  
102 T6 heat treatment. The Cu additions were selected for specific reasons: 0.5 wt.% is  
103 the Cu content in the EN-AC 45500 alloy, 1.5 wt.% is the content for the best  
104 strength-ductility compromise [4-6, 27], 3 wt.% is the Cu content in the EN-AC 46500  
105 alloy. Directional solidification enabled the control of cooling rate and grain size  
106 with a limited number of defects [5] to focus specifically on the role of Cu-related  
107 features. In-situ cyclic testing using a Scanning Electron Microscope (SEM) and  
108 Digital Image Correlation (DIC) highlighted the interaction between crack  
109 development and microstructural features. The distance between Si particles and  
110 Cu-rich phases, quantified with the three-nearest neighbour (3NN) distance, is an

111 important parameter to consider because it significantly affects the crack  
112 propagation of these alloys. Tortuosity is an additional tool to describe the crack  
113 path numerically. The results from our previous work on the same alloys before heat  
114 treatment [28] were the starting point to comprehensively understand the influence  
115 of heat treatment in the present study. Besides, previous work [28] shed light on the  
116 role of Cu-related microstructural features, highlighting that Cu is beneficial for  
117 material strengthening up to a threshold limit for ductility. The results lead to  
118 assessing the mechanical response of the heat-treated alloys, typically employed in  
119 service condition of structural cast components. To the best of the knowledge of the  
120 authors, no similar detailed investigations have been performed to evaluate the  
121 crack propagation [at the microscale level](#) on the heat-treated Cu-added Al-Si-Mg  
122 alloys during cyclic loading. This understanding will benefit the design of structural  
123 components in vehicles with optimised performance.

## 124 **2. EXPERIMENTAL PROCEDURE**

### 125 *2.1 Preparation and characterisation of alloys*

126 Pure Al ingots, pure Si, and an Al-50Mg master alloy were melted in a boron nitride-  
127 coated crucible to prepare four Al-Si-Mg alloys with different Cu concentrations. Cu  
128 contents were obtained with the addition of an Al-50Cu master alloy. After the  
129 completion of melting, grain refiner (Al-5Ti-1B) and modifier (Al-10Sr) master  
130 alloys were also added to achieve the intended contents of 650–700 ppm of titanium  
131 (Ti) and 200–250 ppm of strontium (Sr). Table 1 presents the chemical composition of



132 each alloy, which was evaluated with an optical emission spectrometer

133 (Spectromaxx CCD LMXM3, Spectro Analytical Instruments).

134 Table 1 - Nominal chemical composition [wt.%] of the investigated alloys.

Alloy	Si	Mg	Cu	Fe	Ti	Sr	Al
Cu 0	6.80	0.38	0.00	0.10	0.07	0.03	Balance
Cu 0.5	7.01	0.37	0.51	0.09	0.07	0.02	Balance
Cu 1.5	7.14	0.38	1.61	0.09	0.07	0.02	Balance
Cu 3.0	6.98	0.36	3.23	0.17	0.08	0.02	Balance

135 Cylindrical rods (length 150 mm, diameter 9 mm) were cast, re-melted, and drawn  
136 from a directional solidification furnace raising at ~6 mm/s. This technique produces  
137 a low-defect material because the solidification front pushes oxides and porosities  
138 towards the top of the samples [5]. It also enabled a targeted average Secondary  
139 Dendrite Arm Spacing (SDAS) of 10  $\mu\text{m}$  and targeted Average Grain Size (AGS) of  
140 90  $\mu\text{m}$ . Solution treatment was performed at 495 °C for 1 hour, followed by  
141 quenching in water at 50 °C. After 24 hours of natural ageing, artificial ageing  
142 followed at 210 °C for 1.5 hours. The parameters for the T6 heat treatment were  
143 selected according to the work of Sjölander and Seifeddine [29]. The heat-treatment  
144 parameters were selected to reach the peak strength of the Cu-added alloys and also  
145 applied to the Cu-free alloy, considered as a reference alloy.

146 Electron Back-Scattered Diffraction (EBSD - Hikari Plus, Eden Instruments),  
147 Wavelength Dispersive X-ray Spectroscopy (WDS - Teks HP, Edax), and Energy  
148 Dispersive X-ray Spectroscopy (EDS - Octane Pro, Edax) were employed in a SEM  
149 (Lyra3, Tescan) to determine the AGS, [quantify the element composition](#) in the

150 primary  $\alpha$ -Al matrix, and identify the secondary phases, respectively. Optical  
151 microscope (GX71, Olympus) and SEM (EVO MA15, Zeiss) were employed for  
152 microstructural investigations. Quantitative image analysis (ImageJ) on Si and Cu-  
153 containing particles was conducted to measure the 3NN distance, area, aspect ratio  
154 ( $Feret_{min}/Feret_{max}$ ) and circularity ( $4*\pi*area/perimeter^2$ ), as defined by the ISO 9276-  
155 6:2008 standard. The 3NN distance, as developed in [30], of secondary particles was  
156 measured using the x and y coordinates of each particle centroid. The field of view  
157 (FOV) in the micrographs constituted the reference system for the coordinates. Crack  
158 tortuosity was applied to describe the crack propagation, which is a dimensionless  
159 ratio between the actual crack length and its equivalent straight path. It quantifies  
160 the crack path deviation from linearity: it is equal to 1 for perfectly linear paths and  
161 higher than 1 for tortuous paths. SDAS and AGS were evaluated according to  
162 Method D from Vandersluis *et al.* [31] and the Heyn's linear intercept method from  
163 the ASTM E112 standard, respectively.

164 [The influence of Cu on the  \$\alpha\$ -Al matrix strength](#) was also assessed using Vickers  
165 microhardness (HV0.01) measurements (FM-110, Future Tech Corp). Tensile test  
166 specimens with a gauge length of 50 mm and a diameter of 6 mm were machined  
167 from the heat-treated rods. Tensile testing (Z100, Zwick Roell) was carried out at  
168 room temperature, following the ASTM E8 standard, with a constant cross-head  
169 speed of 0.5 mm/min. A minimum of four samples was tested for each condition  
170 with a clip-on extensometer to measure the strain.

## 171 ***2.2 In-situ cyclic testing and related techniques***

172 Miniature Compact-Tension (CT) samples were cut using electric discharge  
173 machining with a 0.25 mm wire. The miniaturised CT sample dimensions, shown in  
174 Figure 1a, were designed based on the ASTM E647-00 standard guidelines.  
175

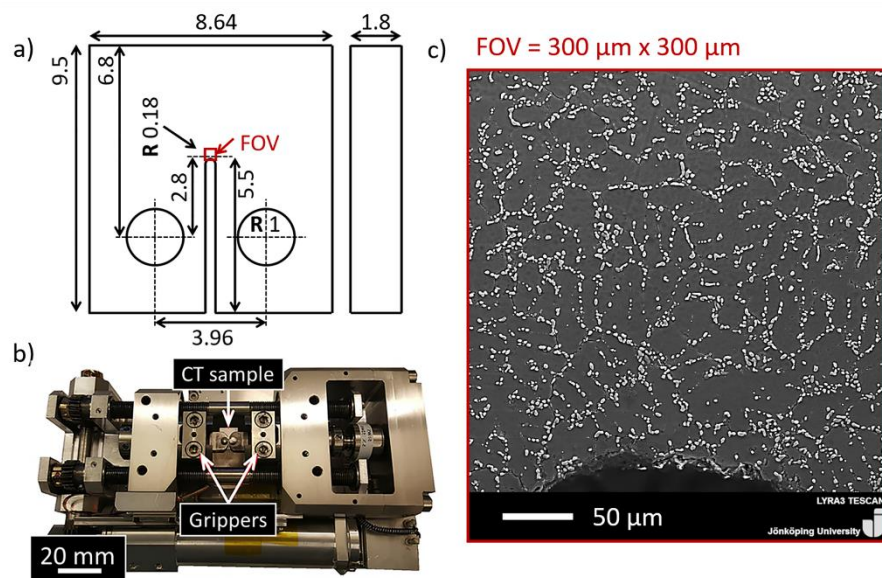


Figure 1 - a) Dimensions of the Compact-Tension (CT) sample in mm; b) miniature stage for in-situ cyclic tests; c) Field Of View (FOV) of the sample, showing the Silicon (Si) particles that formed the random pattern for subsequent Digital Image Correlation (DIC).

176 The FOV size was 300 μm x 300 μm, and it comprehended the notch tip to  
177 investigate local strain development (Fig. 1c). CT samples were electropolished (15 V  
178 for 5 s) to produce a mirror finish for SEM observations, EBSD, and DIC. EBSD maps  
179 were acquired before and after the in-situ fatigue tests to analyse the interaction  
180 between the crack and grain boundaries. In-situ cyclic tests were performed on a  
181 tensile/compression module (Kammrath & Weiss) (Fig. 1b) inside a SEM (Lyra3,  
182 Tescan) at room temperature. Before cyclic loading, the monotonic tension load to  
183 failure of the CT samples showed that the critical stress intensity factor ( $K_{Ic}$ )

184 increased with Cu content, as is shown in Table 2. The selected  $\Delta K = (1 - R) \cdot K_{\max}$  is  
 185 reported in Table 2 for each alloy, with a constant load ratio (R) of 0.2. The selected  
 186  $K_{\max}$  value is 70 % of the  $K_c$  for each alloy. The speed of loading was 8  $\mu\text{m/s}$  ( $\sim 0.1$   
 187 Hz). Two samples of each alloy were tested, and one extra sample of Alloys Cu 0  
 188 and Cu 3.0 was [investigated](#) for Focused Ion Beam (FIB) slicing.

189 Table 2 - Parameters of cyclic testing.

Alloy	$K_c$ [MPa $\cdot\sqrt{\text{m}}$ ]	Preload [N]	$P_{\max}$ [N]	$K_{\max}$ [MPa $\cdot\sqrt{\text{m}}$ ]	$\Delta K$ [MPa $\cdot\sqrt{\text{m}}$ ]
Cu 0	39.3	364	312	27.4	21.9
Cu 0.5	44.4	410	354	31.1	24.9
Cu 1.5	47.6	441	379	33.3	26.7
Cu 3.0	50.2	463	400	35.2	28.1

190 DIC was performed with the MatchID commercial software (MatchID Nv) to obtain  
 191 the strain distribution on the deformed micrographs at different cycles. Eutectic Si  
 192 particles (Fig. 1c) constituted the natural random pattern for DIC, representing a  
 193 time- and cost-saving alternative to artificial patterns. Table 3 presents the  
 194 correlation parameters used for the DIC analysis, following the work of Kasvayee *et*  
 195 *al.* [32]. The resolution of the strain distribution enabled the evaluation of the role of  
 196 grain boundaries in strain development.

197 Table 3 - Correlation parameters used for digital image correlation (DIC).

Parameter	Value
Pixel size [ $\mu\text{m}$ ]	0.24
SS = Subset size [pixel]	111
ST = Step size [pixel]	11
Correlation criterion	Zero-normalised sum of squared differences
Shape function	Quadratic

Interpolation function	Bi-cubic polynomial
Displacement standard deviation [pixel]	0.1
SW = Strain window size [pixels]	15
SSR = Strain spatial resolution [pixels]	173
SSR = SS + [(SW- 1)*ST]	

198 Three-Dimensional (3D) tomography using FIB (Cobra, Orsay Physics)-SEM (Lyra3,  
 199 Tescan) was used to observe the crack path in detail, providing more information  
 200 than was obtained using Two-Dimensional (2D) investigations. A location ahead of  
 201 the propagating crack was selected in an unloaded state, and a rough milling of ~1.7  
 202  $\mu\text{m}$  at 30 kV made a trench around the Area Of Interest (AOI). Fine polishing and  
 203 slicing of the AOI were conducted using a FIB current of ~30 nA at 30 keV. The  
 204 thickness of each slice was 120 nm and captured around 300 SEM images at 5 keV  
 205 using a high-sensitivity in-beam back-scattered electrons detector.

## 206 3. RESULTS AND DISCUSSION

### 207 3.1 Microstructural characterisation

208 The microstructural investigations of the alloys confirmed that the SDAS and AGS  
 209 were in the 8.8 - 11  $\mu\text{m}$  and 82 - 107  $\mu\text{m}$  ranges, respectively. These parameters  
 210 validate that all alloys were in the same conditions of grain refinement and  
 211 solidification. The morphology of Si particles plays a crucial role in the mechanical  
 212 properties of the alloys, and the solution treatment spheroidised and coarsened  
 213 them. Figure 2a compares the values of the area, aspect ratio and circularity of Si  
 214 particles in all the considered alloys.

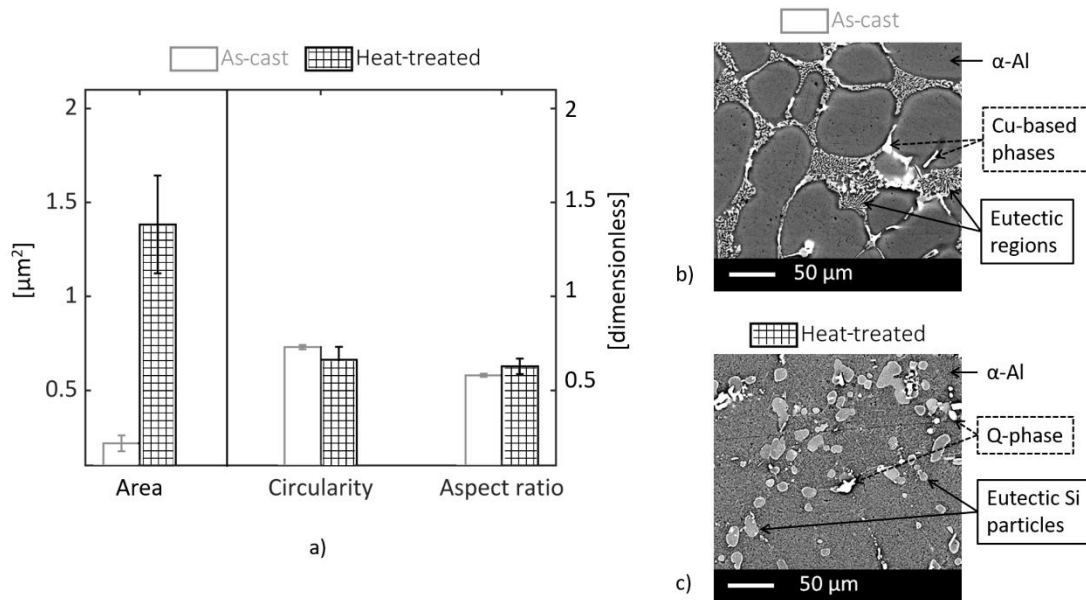


Figure 2 – Evolution of the eutectic Si particles after heat treatment: a) values of the area ( $\mu\text{m}^2$ , left y-axis) and geometrical parameters (dimensionless, right y-axis) of Si particles in the alloys; examples of microstructure for Alloy Cu 3.0 b) before and c) after heat treatment. As-cast data are reported from previous work [28]

215 The average area of the Si particles was significantly larger than in previous work  
 216 [28], up to seven times due to coarsening during heat treatment. This evolution is  
 217 evident from comparing the microstructure of Alloy Cu 3.0 before (Fig. 2b) and after  
 218 heat treatment (Fig. 2c). On the other hand, aspect ratio and circularity were not  
 219 altered much by heat treatment, as the modified Si particles already had a round  
 220 morphology in the as-cast condition [28].

221 The Si and Mg content in the centre of the primary dendrites measured by WDS  
 222 showed a slight decrease with the addition of Cu: Si changed from  $0.94 \pm 0.03$  to  $0.84$   
 223  $\pm 0.01$  wt.%, Mg went from  $0.32 \pm 0.01$  to  $0.27 \pm 0.01$  wt.%. The latter WDS  
 224 measurements confirmed the dissolution of the  $\text{Mg}_2\text{Si}$  phase in the Alloys Cu 0 and  
 225 Cu 0.5. Figure 3b presents the Cu content in the  $\alpha$ -Al dendrites measured by WDS.

226 The result for Alloy Cu 0.5 is 0.52 wt.%, and the comparison with Table 1 shows that  
 227 Cu-based phases were completely dissolved. However, traces of the Q-Al<sub>5</sub>Mg<sub>8</sub>Cu<sub>2</sub>Si<sub>6</sub>  
 228 phase were still present after heat treatment in alloys with Cu contents of 1.5 wt.%  
 229 and 3.2 wt.% (the latter depicted in Fig. 3a), while  $\theta$ -phase was dissolved. The  
 230 calculated Cu content in the remaining Q-phase (identified by EDS) summed with  
 231 the Cu content in the primary  $\alpha$ -Al matrix (measured using WDS) agree with the  
 232 overall Cu content in each alloy (Fig. 3b). This phenomenon occurred because the  
 233 solution treatment at 495 °C for one hour did not entirely dissolve the Q-phase. The  
 234 complete dissolution of the Q phases requires either a two-step solution treatment,  
 235 as presented by Wang *et al.* [33] and Toschi [34], or a treatment period longer than  
 236 one hour [35,36].

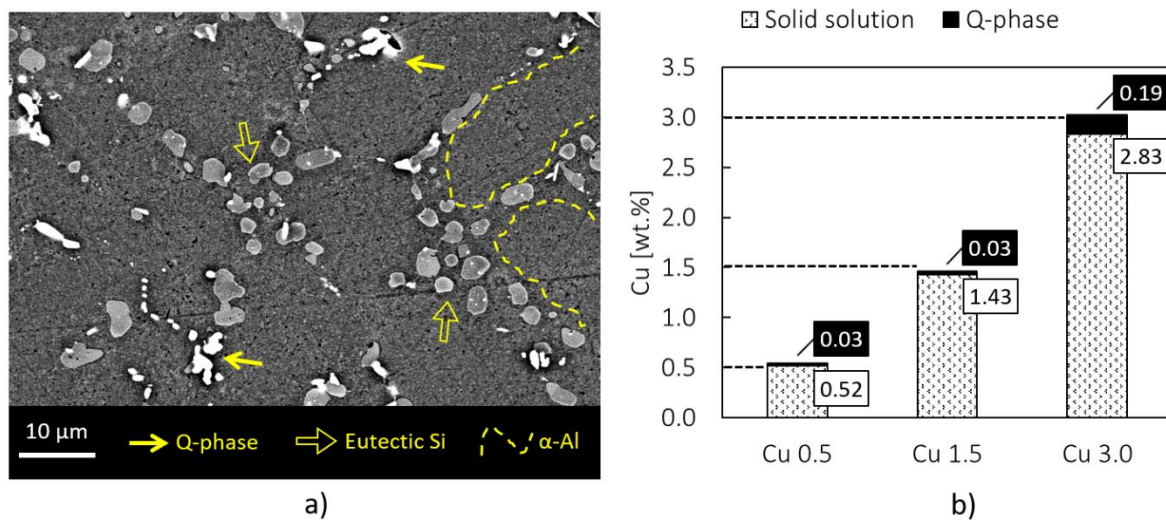


Figure 3 – a) Microstructure of heat-treated Alloy Cu 3.0; b) Cu content in solid solution and undissolved Q-phase. The latter is calculated according to the theoretical Cu content in the Q-Al<sub>5</sub>Mg<sub>8</sub>Cu<sub>2</sub>Si<sub>6</sub> phase (~20 wt.%). Dashed lines represent the overall Cu content in each alloy.

237 The heat treatment also influenced the relative distance between the secondary  
 238 phases, i.e. eutectic Si particles and Cu-based phases. Figure 4 summarise the 3NN  
 239 distance measurements.

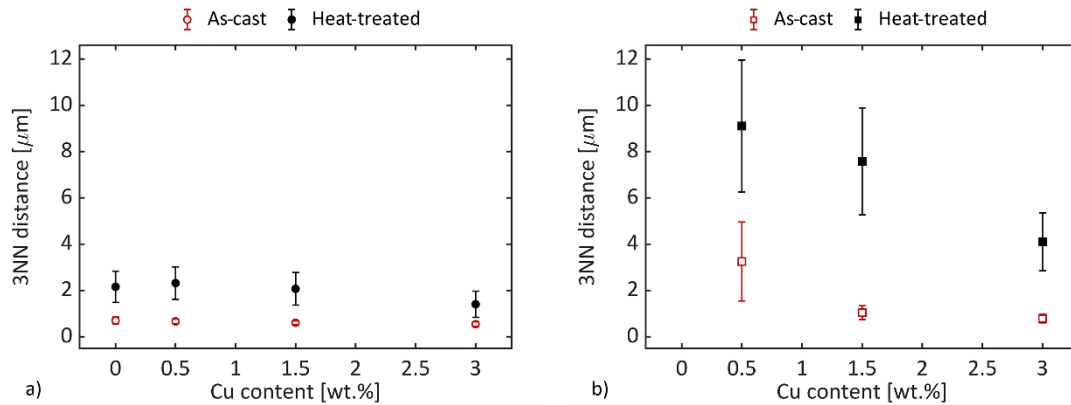


Figure 4 - Three-Nearest-Neighbour (3NN) distance of particles: a) eutectic Si; b) Q phase. The error bars represent the standard deviation.

240 Si particles (Fig. 4a) presented an average 3NN distance of 0.63 μm before heat  
 241 treatment, independent of Cu content. After heat treatment, the distance was in the  
 242 1.40 – 2.32 μm range due to the coarsening effect. On the other hand, the 3NN  
 243 distance of Q phases (Fig. 4b) decreased from 3.55 μm in Alloy Cu 0.5 to 0.78 μm in  
 244 Alloy Cu 3.0 before heat treatment. This decreasing trend mirrored the more  
 245 significant number of intermetallic particles, resulting in a closer distance to each  
 246 other. After heat treatment, the decreasing trend shifted to higher values, from 9.10  
 247 μm in Alloy Cu 0.5 to 4.10 μm in Alloy Cu 3.0 due to the partial dissolution of Q  
 248 phases.

### 249 3.2 Static mechanical properties



250 The mechanical properties showed an improvement in YS (Fig. 5a) and UTS (Fig. 5b)  
251 and a decrease in elongation (Fig. 5c) with increasing Cu concentration. The YS  
252 improved from 3 to 35 % as Cu increased from 0.5 to 3.2 wt.%, while UTS increased  
253 from 10 to 47 %. However, the reduction in elongation was negligible compared to  
254 the reduction in previous work [28], indicating the detrimental role of the Cu-rich  
255 phases. Nevertheless, the heat treatment was beneficial, particularly for alloys with  
256 Cu contents of greater than 1.5 wt.%, and in general, it homogenised the elongation  
257 response of the alloys.

258 The enhancement in YS and UTS was related to the precipitation hardening, also  
259 reported by Zheng *et al.* [15]. Comparing the increasing trend of YS and UTS after  
260 heat treatment with the WDS measurements (Fig. 3b), it is clear that the  
261 strengthening role of the Cu retained in the primary  $\alpha$ -Al matrix was coupled with  
262 the partial dissolution of the Q phases and the total dissolution of the  $\theta$  phases  
263 during heat treatment. The percentage increment in YS (Fig. 5a) mirrored the  
264 percentage improvement in HV0.01 of the primary  $\alpha$ -Al matrix (Fig. 5d), from 1 to 36  
265 %, as Cu increased from 0.5 to 3.2 wt.%. Figure 5d shows that the hardness of the  $\alpha$ -  
266 Al matrix varied in the range of  $98 \div 130$  HV0.01 for the heat-treated alloys, and the  
267 strengthening after heat treatment was related to the Cu retained in the  $\alpha$ -Al matrix  
268 (Fig. 3b).

269 The limited variation of Si morphology (aspect ratio and circularity in Fig. 2a) and  
270 3NN distance (Fig. 4a) after heat treatment was common to all of the alloys, and it  
271 underlines that the mechanical response was primarily affected by the Cu-based

272 phases in this study. The decreasing 3NN distance between Q phases (Fig. 4b)  
 273 reflected the elongation trends in both conditions. Elongation decreased with Cu  
 274 content steeply before heat treatment [28] and slightly after heat treatment, from 11  
 275 to 8 %. Similarly, the average 3NN distance of the Q phases lies in the 9 - 4  $\mu\text{m}$  range  
 276 in the heat-treated condition, while in the as-cast condition, the range was 3.5 - 1  $\mu\text{m}$   
 277 (Fig. 4b). This correlates well with the significant drop in elongation in previous  
 278 work [28].

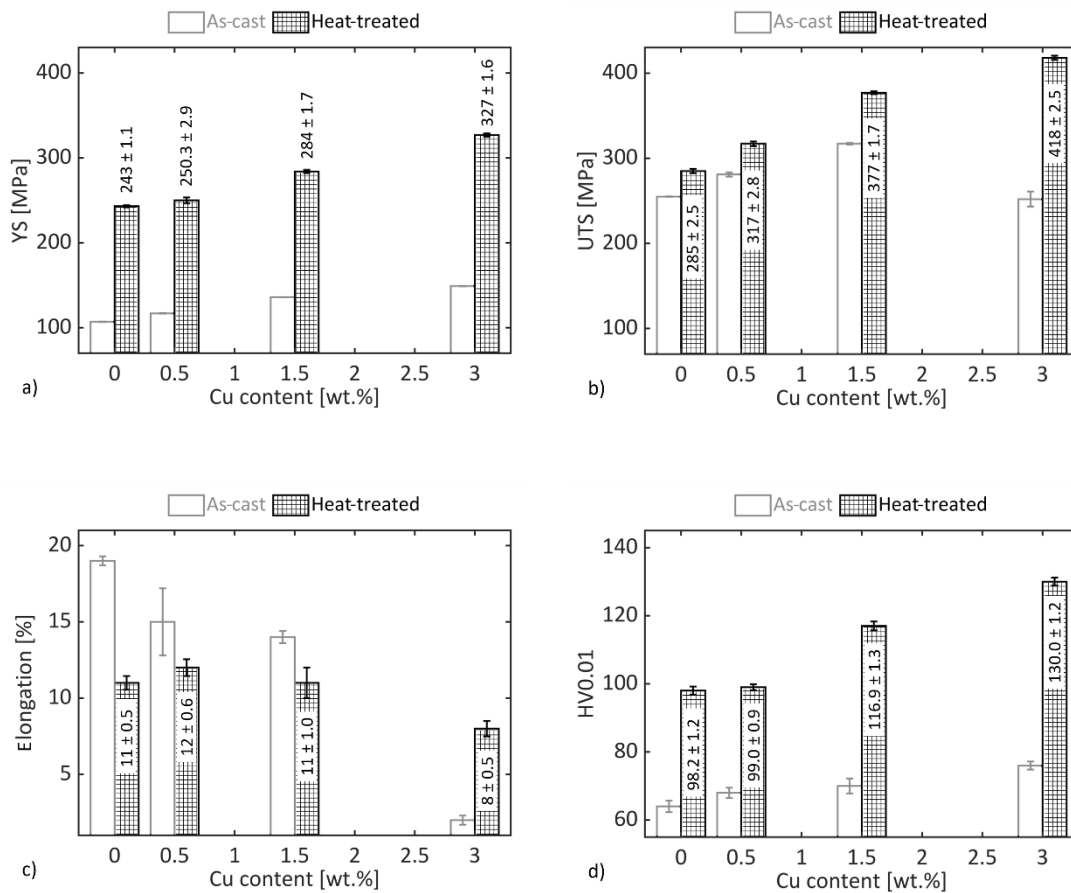


Figure 5 - Mechanical properties of the heat-treated alloys: a) Yield Strength (YS); b) Ultimate Tensile Strength (UTS); c) percentage elongation; d) Vickers microhardness (HV0.01) of the primary  $\alpha$ -Al matrix. The as-cast values from previous work [28] are depicted for direct comparison.

### 279 3.3 In-situ cyclic tests – 2D observations

280 Table 4 shows the results of the in-situ cyclic tests belong to the low-cycle fatigue  
281 regime, as the samples survived 340 - 1500 cycles. The addition of Cu content did not  
282 determine the fatigue life of the samples, as the results are randomly distributed  
283 within this range.

284 Table 4 – Summary of the in-situ cyclic tests on heat-treated CT samples.

Alloy	Sample	Cycles survived
Cu 0	A	800
	B	1500
	C	1253 (stopped for FIB milling)
Cu 0.5	A	690
	B	340
Cu 1.5	A	740
	B	1065
Cu 3.0	A	730
	B	925
	C	640 (stopped for FIB milling)

285

#### 286 3.3.1 Crack initiation

287 The fatigue crack initiation in heat-treated conditions of a hypo-eutectic Al-Si cast  
288 alloy results from micro-scale defects or discontinuities at the surface and subsurface  
289 levels. A 2D perspective indicated that the crack initiation appeared in the primary  
290 dendrite in the Cu-free alloy (Fig. 6a-b and highlighted in Fig. 7a); Cu additions  
291 moved it to the interdendritic regions (Fig. 6c-h). Figure 6g-h shows that the  
292 nucleation sites **were observed** at the grain boundaries (dashed yellow lines, over-  
293 imposed from the EBSD maps) in Alloy Cu 3.0. Figure 6h shows two cracks that  
294 originated from the same point and follow the grain boundaries. On the other hand,

295 Figure 6a-f shows cracks in the grain centre in all of the investigated specimens with  
296 lower Cu concentrations. From observing the polished surfaces, it can be concluded  
297 that crack nucleation occurred in the grain for Cu contents up to 1.5 wt.% and  
298 aligned with the grain boundary for Alloy Cu 3.0. Moreover, defects or  
299 discontinuities **at the sub-micron scale**, such as precipitates, that can act as initiation  
300 sites were not observed in this work and need different investigative approaches.

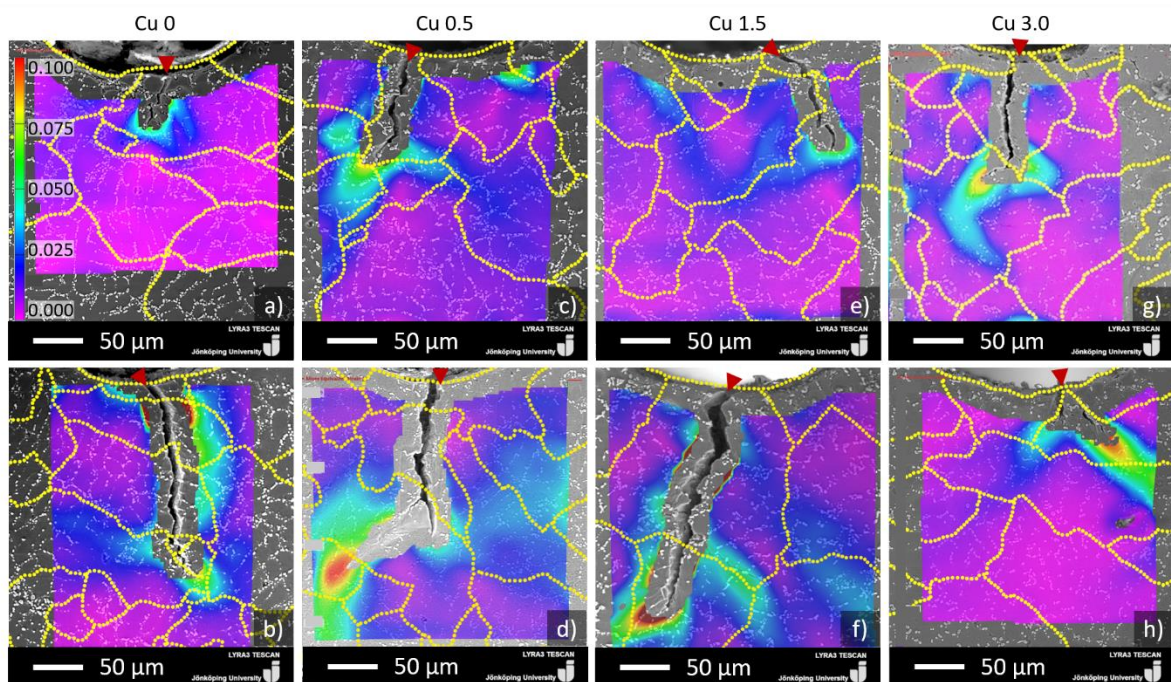


Figure 6 - Crack propagation in all heat-treated alloys combining EBSD and Digital Image Correlation (DIC): a-b) Alloy Cu 0; c-d) Alloy Cu 0.5; e-f) Alloy Cu 1.5; g-h) Alloy Cu 3.0. The dashed yellow lines represent grain boundaries, super-imposed from EBSD, and red arrows point to the initiation sites. The colour bar represents the von Mises equivalent strain and is valid for all the frames.

### 301 3.3.2 Crack propagation

302 Crack propagation is generally expected to follow the least resistance path, offered  
303 by weak or damaged microstructural features ahead of the crack tip. The EBSD maps  
304 generated were super-imposed on the SEM micrograph, and the dashed yellow lines  
305 in Figure 6 represent the grain boundaries.

306 In Alloy Cu 0 (Fig. 6b), the crack propagated along trans-granular paths for the first  
307 150  $\mu\text{m}$  in the FOV, then continued following the grain boundaries. The propagation  
308 followed a mixed path that crossed the dendrite arms and followed the eutectic Si  
309 particles.

310 Crack propagation shifted slightly to the interdendritic regions with the Cu addition  
311 of 0.5 wt.% (Fig. 6c-d). This shift occurred due to the enhanced strength in  $\alpha\text{-Al}$   
312 matrix strength due to the retained Cu, evidenced by WDS measurements in Figure  
313 3b and hardness values in Figure 5d. The DIC results for Alloy Cu 0.5 highlighted  
314 that increment of strain concentration occurred at the grain boundaries. However,  
315 the main propagation path was trans-granular.

316 In Alloy Cu 1.5 (Fig. 6e-f), the propagation is mainly trans-granular with some  
317 intergranular segments, despite the increased strain concentration at the grain  
318 boundaries.

319 Concerning Alloy Cu 3.0 (Fig. 6g-h), the 2D perspective showed that crack growth  
320 tended to follow the grain boundaries. Figure 6g shows that the propagation later  
321 continued across the grains. In Figure 6h, two cracks are propagated under the  
322 dashed yellow lines along the grain boundaries and determined the higher strain  
323 highlighted by the DIC.

324 The crack propagation appears to be mixed on the surface, most as trans-granular  
325 and some inter-granular paths were present in all alloys. DIC in Figure 6 highlighted  
326 that grain boundaries could determine localised strain, and it can ease crack  
327 propagation by determining the occurrence of intergranular segments (Fig. 6h).  
328 More often, the highest strain path is not determined by the grain boundaries (Fig.  
329 6d). Other works [37,38] concluded that grain boundaries serve to distribute  
330 deformation in the microstructure, aligning with what is observed about crack  
331 propagation in Figure 6. Han *et al.* [38] investigated short fatigue crack growth in Al-  
332 7Si-0.4Mg alloy and reported that the grain boundaries deaccelerate crack  
333 propagation by a shielding effect. Nevertheless, the role of grain boundaries is based  
334 only on limited 2D data in the present study, and more investigation is required for a  
335 comprehensive assessment.

336 The increased Cu content in the  $\alpha$ -Al matrix, as precipitates, provide significant  
337 obstacles for the dislocation movement, as shown by Roy *et al.* [17] and Saito *et al.*  
338 [14]. This phenomenon transfers the propagation from the  $\alpha$ -Al matrix in Alloy Cu 0  
339 (yellow arrows in Fig. 7a) to the eutectic regions in Alloy Cu 3.0 (red arrows in Fig.  
340 7b), with an increased number of damaged Si particles and Q phases. This  
341 phenomenon is related to the primary matrix strengthening observed previously  
342 (Fig. 5d) in the present work. Similar behaviour was observed in Alloy Cu 1.5,  
343 whereas the propagation changed from trans-dendritic to inter-dendritic.

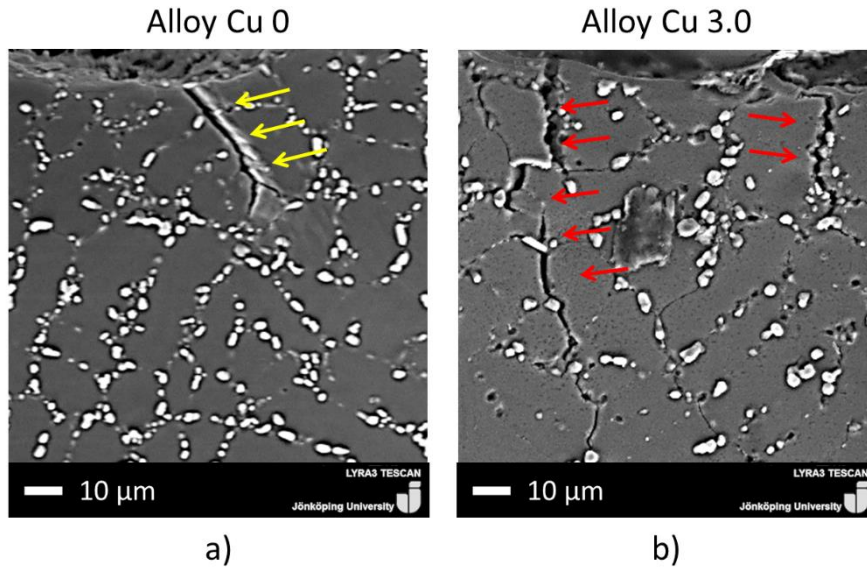


Figure 7 – Examples of crack path: a) trans-dendritic in Alloy Cu 0, pointed by yellow arrows; b) inter-dendritic in Alloy Cu 3.0, pointed by red arrows.

344 Another significant change was the presence of multiple secondary cracks appearing  
345 in the FOV during cyclic loading, indicated by arrows in Figure 8. These secondary  
346 cracks followed the Si particles and Q phases (Fig. 8a) and opened up as cyclic  
347 loading continued (Fig. 8b). The cracks followed the interdendritic regions and  
348 connected the secondary phases due to the reduced 3NN distance between the Q  
349 phases, as shown in Figures 8c and d.



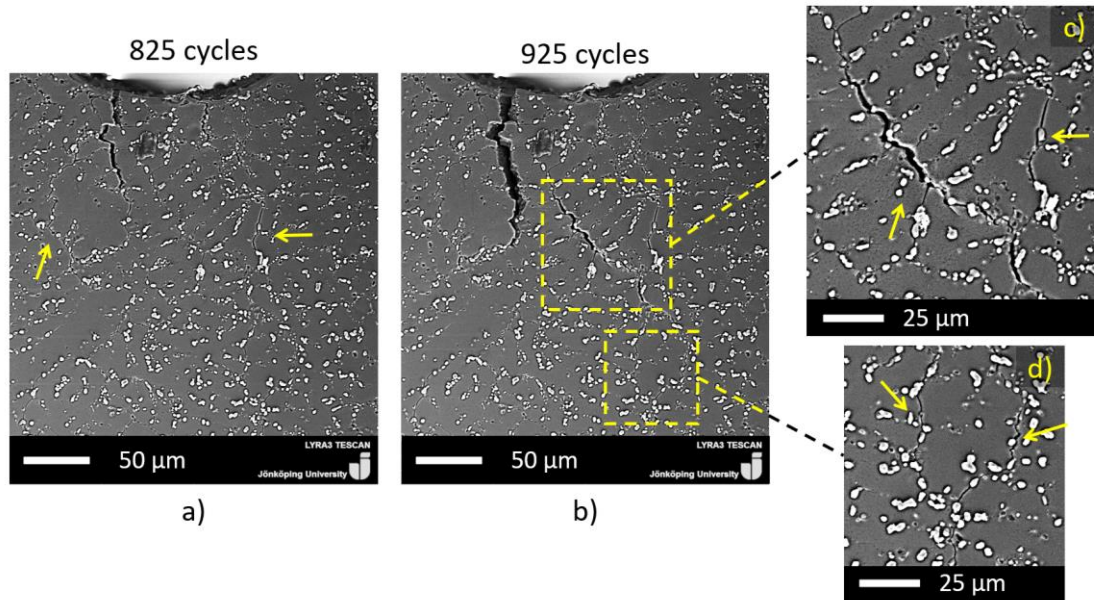


Figure 8 - Development of secondary cracks (indicated by yellow arrows) in heat-treated Alloy Cu 3.0: a) 825 cycles; b) 925 cycles; c-d) magnified micrographs of secondary cracks in (b).

350 Secondary cracks were not evident in the FOV of Alloy Cu 0 and Cu 0.5. Moreover,  
 351 some cracks were detected in Cu 1.5, and many secondary cracks developed in Alloy  
 352 Cu 3.0 (Fig. 8). The  $\alpha$ -Al matrix strength governed the stress concentrations in the  
 353 alloy and, consequently, the propagation behaviour. Inter-dendritic secondary  
 354 cracks developed along the lateral dendrite tips with increasing  $\alpha$ -Al matrix  
 355 strength. The material within the FOV was involved in dissipating the deformation  
 356 that resulted from the cyclic loading, not only the primary crack but also the  
 357 secondary cracks in the interdendritic regions (Fig. 8c-d). This increasing trend of  
 358 secondary crack development aligns well with the decreasing 3NN distance between  
 359 Cu-based phases (Fig. 4b), which enabled the connection between small cracks.  
 360 The influence of the strengthened  $\alpha$ -Al matrix on the evolution of the crack path can  
 361 also be assessed with crack tortuosity. Figure 9 shows that tortuosity varied within



362 1.1-1.2 for the heat-treated alloys, a more limited range than what found in previous  
 363 work [28]. Given the constant values of AGS and SDAS for the alloys in all  
 364 conditions, the evolution of tortuosity with the Cu content accords well with the  
 365 elongation results in Figure 5c.

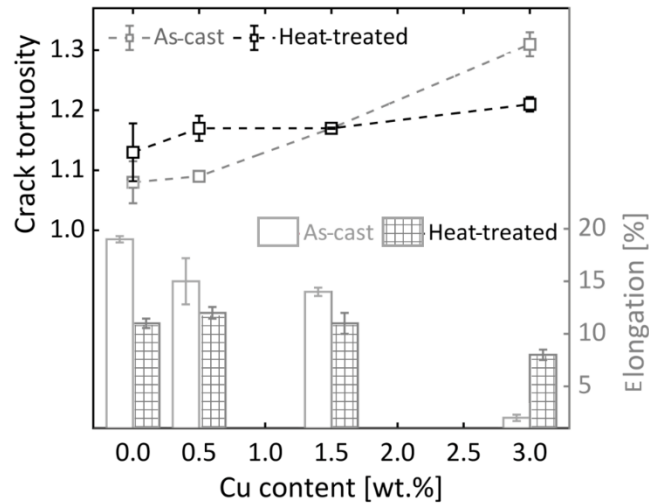


Figure 9 - Comparison of crack tortuosity and elongation trends in the as-cast and heat-treated conditions. The trend lines are meant to guide the eye. The as-cast values from previous work [28] are depicted for direct comparison.

366 In the heat-treated alloys, the constant crack tortuosity trend was related to a  
 367 constant ductility trend. The values for tortuosity for Alloy Cu 1.5 were the same  
 368 before [28] and after heat treatment, with a limited difference in elongation (Fig. 9).  
 369 In previous work [28], Alloy Cu 3.0 had a rapid failure without any previously  
 370 detectable deformation. However, after heat treatment, the crack propagation was  
 371 not sudden and could be followed in the FOV during in-situ cyclic loadings at all  
 372 levels of Cu concentration. Furthermore, the improved elongation (Fig. 5c) coupled  
 373 with the enhanced hardness of the primary  $\alpha$ -Al matrix (Fig. 5d) compared to  
 374 previous work [28] highlights that Cu-containing alloys benefit from an excellent

375 balance between strength and ductility with heat treatment. With this condition, the  
376 damage is progressive during cyclic loading rather than sudden, as was previously  
377 reported [28].

378

### 379 *3.4 In-situ cyclic tests – 3D evaluations*

#### 380 *3.4.1 FIB slicing*

381 The 3D evaluation using FIB slicing of the extreme conditions, Alloys Cu 0 and Cu  
382 3.0, was performed to investigate the development of secondary cracks in Figure 8.

383 Figures 10a and d show the AOI (white rectangles) for the FIB sections investigated

384 of Alloy Cu 0 (Fig. 6a) and Cu 3.0 (Fig. 6h). A 2D perspective showed that crack

385 propagation stopped at the grain boundary during the cyclic testing of Alloy Cu 0.

386 At the beginning of the FIB sections (Fig. 10b), no crack was visible in the thickness

387 but was evident on the surface (white arrow). The bright phases in Section 1 (black

388 arrows in Fig. 10b) are Fe-containing phases, as confirmed by EDS measurements.

389 Moreover, investigating the sections moving toward the crack showed a limited

390 amount of cracked or debonding phases. In Section 170 (Fig. 10c), a crack opened

391 from the underlying volume (red arrows), indicating crack initiation below the

392 surface.

393 As the Cu concentration increased to 3.2 wt.% (Fig. 10d), multiple cracks were visible

394 on the surface of the sample. The white arrow in Figure 10e points to the surface

395 crack, which extended to the material underneath. In the FIB sections, a significant

396 amount of cracked and debonded phases was present ahead of the crack tip

397 compared to Alloy Cu 0. Moreover, the sections toward the crack (Section 250 in Fig.  
 398 10f) clearly shows that the crack propagated from below (red arrows) in the Cu  
 399 phases, which were close to each other 4  $\mu\text{m}$  on average (Fig. 4b).  
 400 These insights on crack propagation from subsurface material **also support the**  
 401 **appearance of the** secondary cracks visible in Figure 8b. These might be the final  
 402 parts of cracks that developed underneath, from coalescence between cracked  
 403 particles, and ultimately reached the polished surface appearing as secondary cracks.

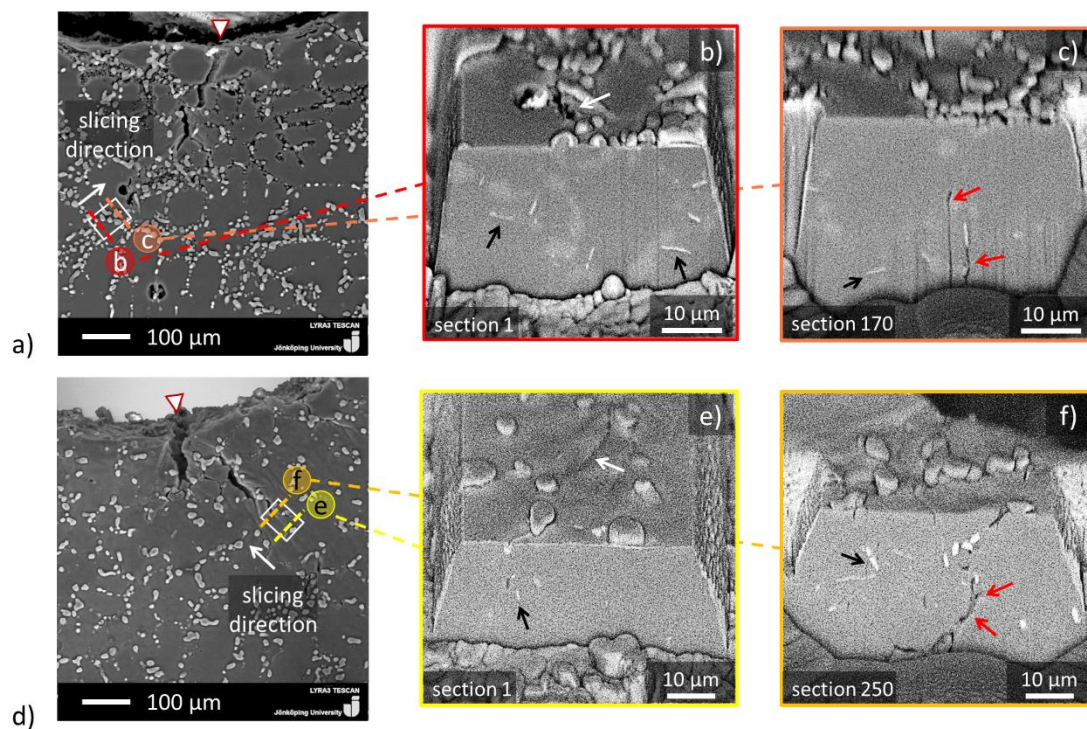


Figure 10 - FIB sections used to investigate the material around the crack in heat-treated alloys. a) Alloy Cu 0, test stopped at 1253 cycles; b) and c) show related sections; d) Alloy Cu 3.0, test stopped at 640 cycles; e) and f) show related sections. The black arrows point to Fe compounds, the white arrows point to superficial cracks, and the red arrows point to the crack coming from underneath.

404 Figure 11b and d shows the 3D reconstruction of the volume removed by FIB slicing,  
 405 showing cracks as red and intermetallic phases as blue in the alloys. Moreover, the  
 406 arrows in the 2D view Figure 11a and c follow the same colour legend. Alloy Cu 0

407 (Fig. 11a) has few cracks in the investigated AOI, while Alloy Cu 3.0 (Fig. 11c)  
 408 contains significantly more cracks. In Alloy Cu 0 (Fig. 11b), the crack appears from  
 409 below, as visualised in Fig 10c. In alloy Cu 3.0 (Fig. 11d), more connected  
 410 microcracks are observed in the AOI. Furthermore, the 3D reconstruction confirms  
 411 that cracks are frequently visible in connection with intermetallic phases, as  
 412 previously observed in 2D slicing (Fig. 10f).

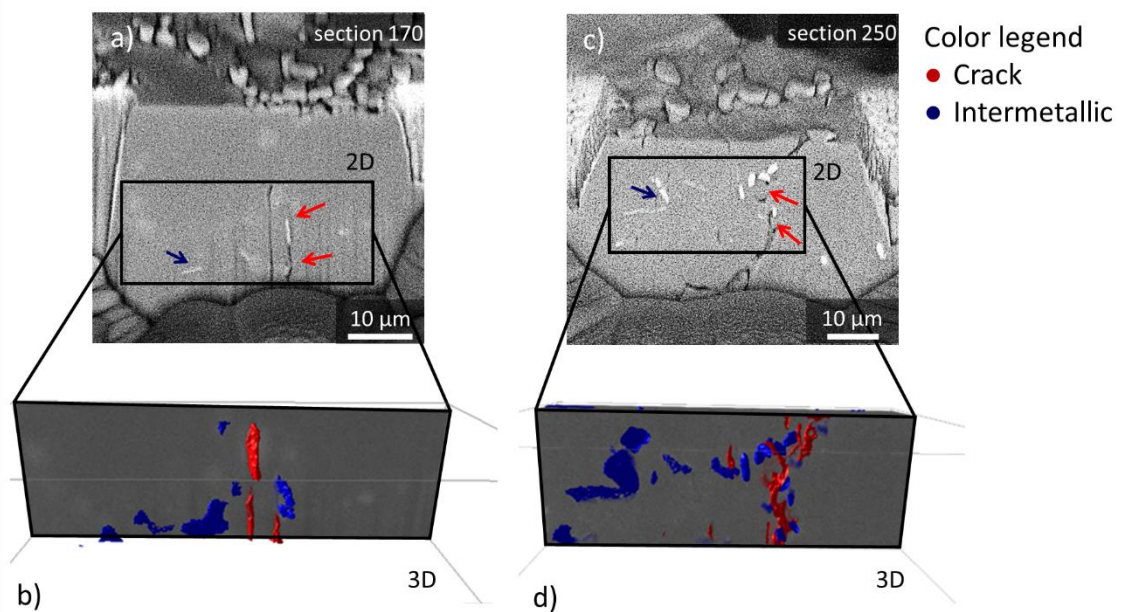


Figure 11 – 3D reconstruction of the FIB sections of the crack in heat-treated alloys. a) FIB section of Alloy Cu 0, test stopped at 1253 cycles, and b) related 3D reconstruction; c) FIB section in Alloy 3.0 Cu, test stopped at 640 cycles, and d) related 3D reconstruction. The red arrows show the cracks, and the blue arrows show the intermetallic phases.

### 413 3.4.2 Fracture surface analyses of CT samples

414 Investigations of fracture surfaces showed that initiation sites were distributed along  
 415 with the thickness of the CT samples. [This outcome aligns with the FIB sections in](#)  
 416 [Figures 10 and 11, which showed cracks originating in the subsurface area.](#) The  
 417 supposed initiation points observed in the 2D view in Figures 6a and h are a later

418 stage of the crack propagation because of the triaxial stress state. The crack  
419 propagation zone (highlighted with the dashed yellow line in Fig. 12a and d) was  
420 distinct from the final fracture zone in the investigated alloys. Moreover, all of the  
421 samples show shear lips (solid yellow lines in Fig. 12a and d, showing Alloys Cu 0  
422 and Cu 3.0) with significant height differences. Magnified views are depicted in  
423 Figures 12c and 12f for Alloys Cu 0 and Cu 3.0, respectively. The fracture  
424 morphology of shear lips indicated a ductile behaviour, and similar dimples  
425 characterised the entire final failure zone in all of the alloys.

426 In Alloy Cu 0, the fracture surface at the notch showed that initiation started at two  
427 locations, each with a different crack propagation orientation. The magnified view of  
428 the propagation zone (Fig. 12b) shows Si particles rising from the surface. This  
429 feature suggests that the Si particles were debonded and pulled out from the  $\alpha$ -Al  
430 matrix during crack propagation.

431 In Alloy Cu 3.0, the initiation started at multiple points, and several cracks appeared  
432 in the propagation zone. In the enlarged view (Fig. 12e), a mixture of debonded Si  
433 particles and cracking around particles are visible; these occurred due to the  
434 enhanced strength of the  $\alpha$ -Al matrix. The difference from previous work [28] was  
435 significant for the alloy with 3.2 wt.% Cu, in which a rapid failure occurred due to  
436 the presence of a significantly greater quantity of Q and  $\theta$  phases. However, the  
437 reduction in the number of Cu-rich particles in Alloy Cu 3.0 after heat treatment  
438 changed the propagation behaviour of the alloy, and the crack path was visible in  
439 Figure 6g-h.



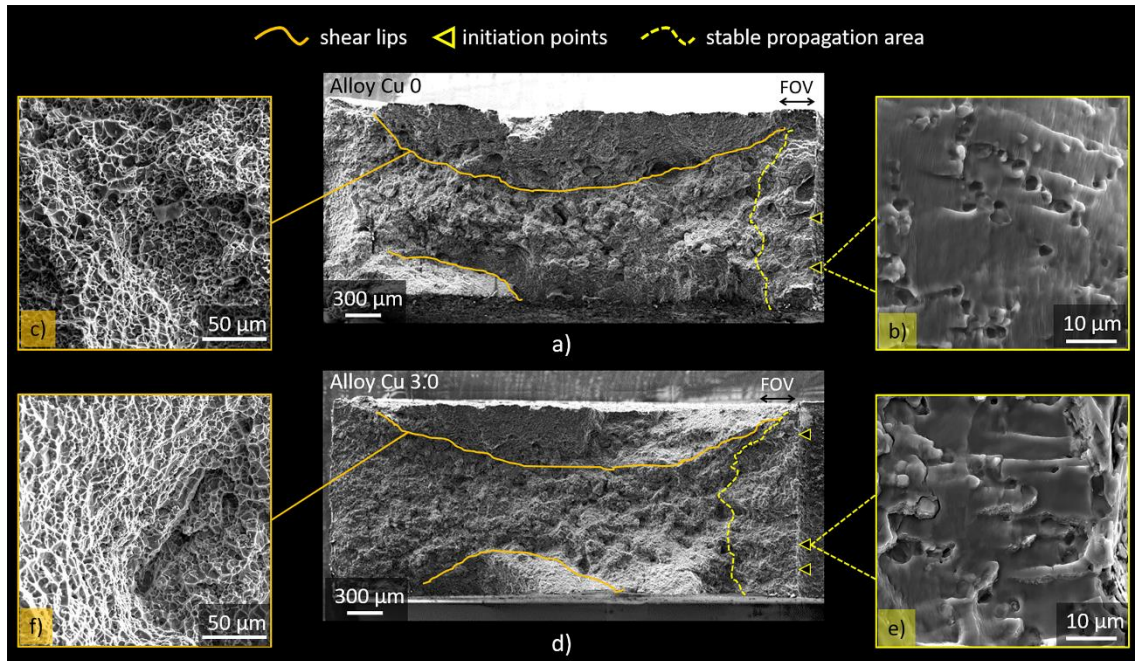


Figure 12 - Fracture surfaces of heat-treated Compact-Tension (CT) samples: a) Alloy Cu 0, b) and c) are magnified views of initiation points and shear lips, respectively, in a); d) Alloy Cu 3.0, e) and f) are magnified views of initiation points and shear lips, respectively, in d).

440 In summary, the presented results show the critical role of Cu in Al-Si-Mg cast alloys  
 441 to determine both crack initiation and propagation. The addition of Cu above 1.5  
 442 wt.% transfers the propagation from the primary  $\alpha$ -Al matrix to the eutectic regions  
 443 because of the complex interaction between the strengthened  $\alpha$ -Al matrix and  
 444 intermetallic phases.

#### 445 4. CONCLUDING REMARKS

446 This study investigated the influence of microstructural features on tensile  
 447 properties and crack development during cyclic loading in heat-treated Al-7Si-Mg  
 448 alloys with different Cu additions. The following conclusions can be drawn:

449 · The limited variation of Si particles after heat treatment, in terms of morphology  
450 and three-nearest-neighbour distance, shown that mechanical properties are  
451 affected by Cu-based phases and primary matrix to a great extent.

452 · The addition of Cu resulted in a continuous improvement in YS and UTS up to  
453 327 and 418 MPa, respectively. The parallel decrease in elongation was limited,  
454 from 11 % to 8 %, while crack tortuosity in CT samples followed the opposite  
455 trend with Cu additions.

456 · Crack initiation occurred at multiple sites in the thicknesses of the samples, as  
457 clarified by FIB sections and fracture surfaces. From the 2D perspective, crack  
458 propagation appeared mostly trans-granular in all the materials. However, the  
459 crack moved from trans-dendritic to inter-dendritic as the Cu content increased.

460 · The primary  $\alpha$ -Al matrix was the most significant feature to influence crack  
461 propagation, as the strengthening effect of Cu influenced the development of  
462 inter-dendritic secondary cracks. These formed from the coalescence of small  
463 cracks that originated in the Si particles and intermetallic phases.

464 The 2D observations were interpreted differently after the three-dimensional  
465 insights provided by FIB sections and fracture surfaces. This study provided a  
466 deeper understanding of the relationship between crack development and  
467 microstructural features, useful for optimised structural components. Future studies  
468 will investigate the variation of other microstructural features that influence the  
469 mechanical response.

470

471 **Funding:** This research did not receive any specific grant from funding agencies in the public,  
472 commercial, or not-for-profit sectors.

473 **Data availability:** The data that support the findings of this study are available from the  
474 corresponding author on reasonable request.

475 **CRedit authorship contribution statement:** Toni Bogdanoff: Investigation, Data curation, Writing -  
476 Original draft preparation. Lucia Lattanzi: Investigation, Data curation, Writing - Original draft  
477 preparation. Mattia Merlin: Supervision, Writing - Reviewing and Editing. Ehsan Ghassemali:  
478 Visualisation, Methodology, Writing - Reviewing and Editing. Anders E.W. Jarfors: Supervision,  
479 Writing - Reviewing and Editing. Salem Seifeddine: Conceptualisation, Supervision, Resources,  
480 Writing - Reviewing and Editing.

481 **Declaration of competing interest:** The authors declare that they have no known competing financial  
482 interests or personal relationships that could have appeared to influence the work reported in this  
483 paper.

484 **Acknowledgements:** The authors gratefully acknowledge Mr. Riccardo Castiglieri for help in  
485 performing part of the experimental work.

486

## 487 REFERENCES

488 [1] A.C. Serrenho, J.B. Norman, J.M. Allwood, The impact of reducing car weight  
489 on global emissions: the future fleet in Great Britain, *Phil. Trans. R. Soc. A* (2017)  
490 20160364.

491 [2] N. Hooftman, M. Messagie, J. Van Mierlo, T. Coosemans, A review of the  
492 European passenger car regulations – Real driving emissions vs local air quality,  
493 *Renewable and Sustainable Energy Reviews* 86 (2018) 1-21.

494 [3] E-mobility 2020 – Materials selection for a more sustainable automotive future,  
495 *Hydro papers*, May 2020, 1-24.



- 496 [4] R. Taghiabadi, A. Fayegh, A. Pakbin, M. Nazari, M. Ghoncheh, Quality index  
497 and hot tearing susceptibility of Al-7Si-0.35 Mg-xCu alloys, Transactions of  
498 Nonferrous Metals Society of China 28(7) (2018) 1275-1286.
- 499 [5] S. Seifeddine, E. Sjölander, T. Bogdanoff, On the role of copper and cooling rates  
500 on the microstructure, defect formations and mechanical properties of Al-Si-Mg  
501 alloys, Materials Sciences and Applications 4 (2013) 171-178.
- 502 [6] S. Shabestari, H. Moemeni, Effect of copper and solidification conditions on the  
503 microstructure and mechanical properties of Al-Si-Mg alloys, Journal of Materials  
504 Processing Technology 153 (2004) 193-198.
- 505 [7] C. Caceres, M. Djurdjevic, T. Stockwell, J. Sokolowski, The effect of Cu content  
506 on the level of microporosity in Al-Si-Cu-Mg casting alloys, Scripta Materialia 40(5)  
507 (1999) 631-637.
- 508 [8] L. Ceschini, S. Messieri, A. Morri, S. Seifeddine, S. Toschi, M. Zamani, Effect of  
509 Cu addition on overaging behaviour, room and high temperature tensile and  
510 fatigue properties of A357 alloy, Transactions of Nonferrous Metals Society of  
511 China 30 (2020) 2861-2878.
- 512 [9] E. Cerri, M.T. Di Giovanni, E. Ghio, A study of intermetallic phase stability in  
513 Al-Si-Mg casting alloy: The role of Cu additions, Metallurgia Italiana 112 (2020) 7-  
514 8, 37-47.
- 515 [10] J. Baskaran, P. Raghuvaran, S. Ashwin, Experimental investigation on the effect  
516 of microstructure modifiers and heat treatment influence on A356 alloy, Materials  
517 Today: Proceedings 37-2 (2021) 3007-3010.
- 518 [11] S. Beroual, Z. Boumerzoug, P. Paillard, Y. Borjon-Piron. Effects of heat  
519 treatment and addition of small amounts of Cu and Mg on the microstructure and  
520 mechanical properties of Al-Si-Cu and Al-Si-Mg cast alloys, Journal of Alloys and  
521 Compounds 784 (2019) 1026-1035.
- 522 [12] M.T. Di Giovanni, E.A. Mørtzell, T. Saito, S. Akhtar, M. Di Sabatino, Y. Li, E.  
523 Cerri, Influence of Cu addition on the heat treatment response of A356 foundry  
524 alloy, Materials Today Communications 19 (2019) 342-348.

- 525 [13] E.A. Mørtzell, F. Qian, C.D. Marioara, Y. Li, Precipitation in an A356 foundry  
526 alloy with Cu additions-A transmission electron microscopy study, *Journal of*  
527 *Alloys and Compounds* 785 (2019) 1106-1114.
- 528 [14] T. Saito, E.A. Mørtzell, S. Wenner, C.D. Marioara, S.J. Andersen, J. Friis, K.  
529 Matsuda, R. Holmestad, Atomic structures of precipitates in Al–Mg–Si alloys with  
530 small additions of other elements, *Adv. Eng. Mater.* 20(7) (2018) 1800125.
- 531 [15] Y. Zheng, W. Xiao, S. Ge, W. Zhao, S. Hanada, C. Ma, Effects of Cu content and  
532 Cu/Mg ratio on the microstructure and mechanical properties of Al–Si–Cu–Mg  
533 alloys, *Journal of Alloys and Compounds* 649 (2015) 291-296.
- 534 [16] C. Caceres, I.L. Svensson, J. Taylor, Strength-ductility behaviour of Al-Si-Cu-  
535 Mg casting alloys in T6 temper, *International Journal of Cast Metals Research* 15(5)  
536 (2003) 531-543.
- 537 [17] S. Roy, L.F. Allard, A. Rodriguez, T.R. Watkins, A. Shyam, Comparative  
538 Evaluation of Cast Aluminum Alloys for Automotive Cylinder Heads: Part I—  
539 Microstructure Evolution, *Metallurgical and Materials Transactions A* (2017) 1-14.
- 540 [18] S. Roy, L.F. Allard, A. Rodriguez, W.D. Porter, A. Shyam, Comparative  
541 evaluation of cast aluminum alloys for automotive cylinder heads: Part II—  
542 mechanical and thermal properties, *Metallurgical and Materials Transactions A*  
543 48(5) (2017) 2543-2562.
- 544 [19] E. Sjölander, S. Seifeddine, The heat treatment of Al–Si–Cu–Mg casting alloys,  
545 *Journal of Materials Processing Technology* 210(10) (2010) 1249-1259.
- 546 [20] K.S. Chan, P. Jones, Q. Wang, Fatigue crack growth and fracture paths in sand  
547 cast B319 and A356 aluminum alloys, *Materials Science and Engineering: A* 341(1-  
548 2) (2003) 18-34.
- 549 [21] D.A. Lados, D. Apelian, P.E. Jones, J.F. Major, Microstructural mechanisms  
550 controlling fatigue crack growth in Al–Si–Mg cast alloys, *Materials Science and*  
551 *Engineering: A* 468 (2007) 237-245.

- 552 [22] D.A. Lados, D. Apelian, Fatigue crack growth characteristics in cast Al–Si–Mg  
553 alloys: Part I. Effect of processing conditions and microstructure, *Materials Science*  
554 *and Engineering: A* 385(1-2) (2004) 200-211.
- 555 [23] D.A. Lados, D. Apelian, L. Wang, Solution treatment effects on microstructure  
556 and mechanical properties of Al-(1 to 13 pct) Si-Mg cast alloys, *Metallurgical and*  
557 *Materials Transactions B* 42(1) (2011) 171-180.
- 558 [24] D. Tomazincic, M. Borovinsek, Z. Ren, J. Klemenc, Improved prediction of low-  
559 cycle fatigue life for high-pressure die-cast aluminium alloy AlSi9Cu3 with  
560 significant porosity, *International Journal of Fatigue* 144 (2021) 106061.
- 561 [25] J. Hirsch, *Automotive Trends in Aluminium - The European Perspective*,  
562 *Materials Forum* 28 (2004) 15-23.
- 563 [26] G.K. Sigworth, R.J. Donahue, The metallurgy of Aluminum alloys for structural  
564 high-pressure die castings, *International Journal of Metal Casting* (2020).
- 565 [27] T. Lu, J. Wu, Y. Pan, S. Tao, Y. Chen, Optimising the tensile properties of Al-  
566 11Si-0.3Mg alloys: role of Cu addition, *Journal of Alloys and Compounds* 631  
567 (2015) 276-282.
- 568 [28] T. Bogdanoff, L. Lattanzi, M. Merlin, E. Ghassemali, S. Seifeddine, The  
569 Influence of Copper Addition on Crack Initiation and Propagation in an Al-Si-Mg  
570 Alloy During Cyclic Testing, *Materialia* (2020) 100787.
- 571 [29] E. Sjölander, S. Seifeddine, Artificial ageing of Al–Si–Cu–Mg casting alloys,  
572 *Materials Science and Engineering: A* 528(24) (2011) 7402-7409.
- 573 [30] J.J. Friel, *Practical guide to image analysis*, ASM international 2000.
- 574 [31] Vandersluis, E., Ravindran, C. Comparison of Measurement Methods for  
575 Secondary Dendrite Arm Spacing. *Metallogr. Microstruct. Anal.* 6, 89–94 (2017).  
576 <https://doi.org/10.1007/s13632-016-0331-8>
- 577 [32] K.A. Kasvayee, E. Ghassemali, K. Salomonsson, S. Sujakhu, S. Castagne, A.E.  
578 Jarfors, Microstructural strain mapping during in-situ cyclic testing of ductile iron,  
579 *Materials Characterization* 140 (2018) 333-339.

- 580 [33] X. Wang, J. Embury, W. Poole, S. Esmaili, D. Lloyd, Precipitation  
581 strengthening of the aluminum alloy AA6111, *Metallurgical and Materials*  
582 *Transactions A* 34(12) (2003) 2913-2924.
- 583 [34] S. Toschi, Optimisation of A354 Al-Si-Cu-Mg Alloy Heat Treatment: Effect on  
584 Microstructure, Hardness, and Tensile Properties of Peak Aged and Overaged  
585 Alloy, *Metals* 8(11) (2018) 961.
- 586 [35] E. Sjölander, S. Seifeddine, Optimisation of solution treatment of cast Al-7Si-0.3  
587 Mg and Al-8Si-3Cu-0.5 Mg alloys, *Metallurgical and Materials Transactions A* 45(4)  
588 (2014) 1916-1927.
- 589 [36] Y. Han, A. Samuel, F. Samuel, S. Valtierra, H. Doty, 08-014 Effect of Solution  
590 Heat Treatment Type on the Dissolution of Copper Phases in Al-Si-Cu-Mg Type  
591 Alloys, *Transactions of the American Foundrymen's Society* 116 (2008) 79.
- 592 [37] A.C. Magee, L. Ladani, Representation of a microstructure with bimodal grain  
593 size distribution through crystal plasticity and cohesive interface modelling,  
594 *Mechanics of Materials* 82 (2015) 1-12.
- 595 [38] S.W. Han, S. Kumai, A. Sato, Effects of solidification structure on short fatigue  
596 crack growth in Al-7%Si-0.4%Mg alloy castings, *Materials Science and Engineering*  
597 *A* 332 (2002) 56-63.

1 **The complex interaction between microstructural features and crack**  
2 **evolution during cyclic testing in heat-treated Al-Si-Mg-Cu cast alloys**

3 Toni Bogdanoff <sup>a</sup>, Lucia Lattanzi <sup>a,b</sup>, Mattia Merlin <sup>b</sup>, Ehsan Ghassemali <sup>a</sup>, Anders E.W. Jarfors

4 <sup>a</sup>, Salem Seifeddine <sup>a</sup>

5 <sup>a</sup> Department of Materials and Manufacturing, Jönköping University, Box 1026, 55111 Jönköping,

6 Sweden

7 <sup>b</sup> Department of Engineering, University of Ferrara, Via Giuseppe Saragat 1, 44122 Ferrara, Italy

8 Corresponding author: Toni Bogdanoff, +46 722066640

9 Email addresses: toni.bogdanoff@ju.se (T. Bogdanoff), lucia.lattanzi@ju.se (L.

10 Lattanzi), mattia.merlin@unife.it (M. Merlin), ehsan.ghassemali@ju.se (E.

11 Ghassemali), anders.jarfors@ju.se (A. Jarfors), salem.seifeddine@ju.se (S. Seifeddine)

12

13

14

15

16

17

18

19

20

21

22

23 **ABSTRACT**

24 The study aimed to investigate crack initiation and propagation at the micro-scale in  
25 heat-treated Al-7Si-Mg cast alloys with different copper (Cu) contents. In-situ cyclic  
26 testing in a scanning electron microscope coupled with electron back-scattered  
27 diffraction and digital image correlation was used to evaluate the complex  
28 interaction between the crack path and the microstructural features. The three-  
29 nearest-neighbour distance of secondary particles was a new tool to describe the  
30 crack propagation in the alloys. The amount of Cu retained in the  $\alpha$ -Al matrix after  
31 heat treatment increased with the Cu content in the alloy and enhanced the strength  
32 with a slight decrease in elongation. During cyclic testing, the two-dimensional (2D)  
33 crack path appeared with a mixed propagation, both trans- and inter-granular,  
34 regardless of the Cu content of the alloy. On fracture surfaces, multiple crack  
35 initiation points were detected along the thickness of the samples. The debonding of  
36 silicon (Si) particles took place during crack propagation in the Cu-free alloy, while  
37 cracking of Si particles and intermetallic phases occurred in the alloy with 3.2 wt.%  
38 Cu. Three-dimensional tomography using focused ion beam revealed that the  
39 improved strength of the  $\alpha$ -Al matrix changes the number of cracked particles ahead  
40 of the propagating crack with Cu concentration above 1.5 wt.%.

41

42 **Keywords:** aluminium alloys; electron microscopy; characterisation; casting  
43 methods; fatigue.

44

## 45 1. INTRODUCTION

46 Nowadays, the automotive sector strives for lightweight solutions for reducing gas  
47 emissions and fuel consumption [1-2]. Besides, the components of electric vehicles  
48 must meet additional requirements regarding reduced weight and optimised  
49 mechanical performance. For these reasons, it is crucial to perfectly match the  
50 selection of materials to the operational life of components [3]. Hypoeutectic Al-Si  
51 cast alloys are a valid candidate for fulfilling these requirements, particularly with  
52 the right combination of alloying elements, such as magnesium (Mg) and copper  
53 (Cu), and post solidification treatments. The addition of Mg and Cu combined with  
54 proper heat treatment provides a good compromise between the ductility of Al-Si-  
55 Mg alloys and the strength of Al-Si-Cu systems [4-6]. For this reason, over the last  
56 two decades, the literature has addressed the addition of Cu to Al-Si-Mg cast alloys  
57 for both as-cast [4-7] and heat-treated conditions to obtain high strength [8-19].  
58 The T6 heat treatment is typically applied to Al-Si-Mg and Al-Si-Cu-Mg alloys and  
59 consists of solution treatment, quenching, and ageing. These steps lead to dispersed  
60 precipitates that hinder dislocation movements and improve the strength of the  
61 material. In Al-Si-Mg alloys, the precipitation sequence during ageing results in an  
62 incoherent  $\beta$ -Mg<sub>2</sub>Si phase [17]. The addition of Cu changes the precipitation  
63 sequence of the alloy, inducing Cu-based precipitates, as reported in the literature  
64 [12-14]. For a Cu content greater than 1.5 wt.%, the incoherent  $\theta$ -Al<sub>2</sub>Cu phase ends  
65 the precipitation sequence and suppresses the  $\beta$ -Mg<sub>2</sub>Si phase [17]. The strength  
66 improvement is due to a sufficient number of precipitates of appropriate size and

67 spacing. Peak ageing generally occurs within the transition from coherent to semi-  
68 coherent precipitates when the optimal number density combined with optimal  
69 precipitate spacing is reached [18]. Natural ageing before artificial ageing is  
70 beneficial for Al-Si-Mg alloys because it promotes a microstructure with a lower  
71 number density of coarser particles compared to the directly artificially aged alloy  
72 [18,19].

73 As a consequence of heat treatment, the addition of Cu improves the Yield Strength  
74 (YS) and Ultimate Tensile Strength (UTS) of Al-Si-Mg alloys. Caceres *et al.* [16]  
75 investigated the influence of Si, Cu, and Mg on the tensile properties of heat-treated  
76 Al-Si-Mg-Cu systems. They concluded that to achieve the optimal mechanical  
77 response, Cu content should be limited to 3 wt.% when Mg content is above 1 wt.%.  
78 Zheng *et al.* [15] investigated Al-6Si-Cu-Mg alloys with Cu/Mg ratios from 1 to 4.  
79 They reported that the precipitation sequence depends on the Cu content and the  
80 Cu/Mg ratio: a low-ratio alloy tends to preferentially form the precursor of  $\beta$   
81 precipitates, whereas a high-ratio alloy will lead to the formation of Q and  $\theta$   
82 precursors. A higher Cu/Mg ratio by increasing Cu content improves both strength  
83 and elongation.

84 The effect of T6 heat treatment also influences the fatigue response of the material. In  
85 particular, crack propagation is characterised by significantly more branching and  
86 crack deflection compared to the as-cast condition due to crack-tip shielding and  
87 lower crack growth rates [20]. For this reason, Lados *et al.* [21-23] have been focusing  
88 their attention on the influence of microstructural features on long and small fatigue



89 crack growth in heat-treated Al-Si-Mg alloys. About the  $\alpha$ -Al matrix strength, they  
90 reported that the crack growth rate is higher for naturally-aged samples than for T6  
91 ones in upper Region II and lower Region III of the Paris curve. On the other hand,  
92 in upper Region III, naturally-aged material showed improved fatigue crack growth  
93 resistance due to the ductile tearing in the  $\alpha$ -Al matrix.

94 From this background, an in-depth understanding of crack initiation and  
95 propagation on the microstructural scale is crucial for developing high-performance  
96 alloys, especially for the transportation sector. In addition, structural components  
97 like suspension systems must withstand dynamic loading [24-26], and it is crucial to  
98 assess the role of the heat-treated microstructure in either promoting or shielding  
99 crack propagation.

100 The present work aimed to identify the microstructural features that significantly  
101 influence the crack initiation and propagation of a Cu-added Al-7Si-Mg alloy after  
102 T6 heat treatment. The Cu additions were selected for specific reasons: 0.5 wt.% is  
103 the Cu content in the EN-AC 45500 alloy, 1.5 wt.% is the content for the best  
104 strength-ductility compromise [4-6, 27], 3 wt.% is the Cu content in the EN-AC 46500  
105 alloy. Directional solidification enabled the control of cooling rate and grain size  
106 with a limited number of defects [5] to focus specifically on the role of Cu-related  
107 features. In-situ cyclic testing using a Scanning Electron Microscope (SEM) and  
108 Digital Image Correlation (DIC) highlighted the interaction between crack  
109 development and microstructural features. The distance between Si particles and  
110 Cu-rich phases, quantified with the three-nearest neighbour (3NN) distance, is an

111 important parameter to consider because it significantly affects the crack  
112 propagation of these alloys. Tortuosity is an additional tool to describe the crack  
113 path numerically. The results from our previous work on the same alloys before heat  
114 treatment [28] were the starting point to comprehensively understand the influence  
115 of heat treatment in the present study. Besides, previous work [28] shed light on the  
116 role of Cu-related microstructural features, highlighting that Cu is beneficial for  
117 material strengthening up to a threshold limit for ductility. The results lead to  
118 assessing the mechanical response of the heat-treated alloys, typically employed in  
119 service condition of structural cast components. To the best of the knowledge of the  
120 authors, no similar detailed investigations have been performed to evaluate the  
121 crack propagation at the microscale level on the heat-treated Cu-added Al-Si-Mg  
122 alloys during cyclic loading. This understanding will benefit the design of structural  
123 components in vehicles with optimised performance.

## 124 **2. EXPERIMENTAL PROCEDURE**

### 125 *2.1 Preparation and characterisation of alloys*

126 Pure Al ingots, pure Si, and an Al-50Mg master alloy were melted in a boron nitride-  
127 coated crucible to prepare four Al-Si-Mg alloys with different Cu concentrations. Cu  
128 contents were obtained with the addition of an Al-50Cu master alloy. After the  
129 completion of melting, grain refiner (Al-5Ti-1B) and modifier (Al-10Sr) master  
130 alloys were also added to achieve the intended contents of 650-700 ppm of titanium  
131 (Ti) and 200-250 ppm of strontium (Sr). Table 1 presents the chemical composition of

132 each alloy, which was evaluated with an optical emission spectrometer

133 (Spectromaxx CCD LMXM3, Spectro Analytical Instruments).

134 Table 1 - Nominal chemical composition [wt.%] of the investigated alloys.

Alloy	Si	Mg	Cu	Fe	Ti	Sr	Al
Cu 0	6.80	0.38	0.00	0.10	0.07	0.03	Balance
Cu 0.5	7.01	0.37	0.51	0.09	0.07	0.02	Balance
Cu 1.5	7.14	0.38	1.61	0.09	0.07	0.02	Balance
Cu 3.0	6.98	0.36	3.23	0.17	0.08	0.02	Balance

135 Cylindrical rods (length 150 mm, diameter 9 mm) were cast, re-melted, and drawn  
136 from a directional solidification furnace raising at ~6 mm/s. This technique produces  
137 a low-defect material because the solidification front pushes oxides and porosities  
138 towards the top of the samples [5]. It also enabled a targeted average Secondary  
139 Dendrite Arm Spacing (SDAS) of 10  $\mu\text{m}$  and targeted Average Grain Size (AGS) of  
140 90  $\mu\text{m}$ . Solution treatment was performed at 495 °C for 1 hour, followed by  
141 quenching in water at 50 °C. After 24 hours of natural ageing, artificial ageing  
142 followed at 210 °C for 1.5 hours. The parameters for the T6 heat treatment were  
143 selected according to the work of Sjölander and Seifeddine [29]. The heat-treatment  
144 parameters were selected to reach the peak strength of the Cu-added alloys and also  
145 applied to the Cu-free alloy, considered as a reference alloy.

146 Electron Back-Scattered Diffraction (EBSD - Hikari Plus, Eden Instruments),  
147 Wavelength Dispersive X-ray Spectroscopy (WDS - Teks HP, Edax), and Energy  
148 Dispersive X-ray Spectroscopy (EDS - Octane Pro, Edax) were employed in a SEM  
149 (Lyra3, Tescan) to determine the AGS, quantify the element composition in the

150 primary  $\alpha$ -Al matrix, and identify the secondary phases, respectively. Optical  
151 microscope (GX71, Olympus) and SEM (EVO MA15, Zeiss) were employed for  
152 microstructural investigations. Quantitative image analysis (ImageJ) on Si and Cu-  
153 containing particles was conducted to measure the 3NN distance, area, aspect ratio  
154 ( $Feret_{min}/Feret_{max}$ ) and circularity ( $4*\pi*area/perimeter^2$ ), as defined by the ISO 9276-  
155 6:2008 standard. The 3NN distance, as developed in [30], of secondary particles was  
156 measured using the x and y coordinates of each particle centroid. The field of view  
157 (FOV) in the micrographs constituted the reference system for the coordinates. Crack  
158 tortuosity was applied to describe the crack propagation, which is a dimensionless  
159 ratio between the actual crack length and its equivalent straight path. It quantifies  
160 the crack path deviation from linearity: it is equal to 1 for perfectly linear paths and  
161 higher than 1 for tortuous paths. SDAS and AGS were evaluated according to  
162 Method D from Vandersluis *et al.* [31] and the Heyn's linear intercept method from  
163 the ASTM E112 standard, respectively.

164 The influence of Cu on the  $\alpha$ -Al matrix strength was also assessed using Vickers  
165 microhardness (HV0.01) measurements (FM-110, Future Tech Corp). Tensile test  
166 specimens with a gauge length of 50 mm and a diameter of 6 mm were machined  
167 from the heat-treated rods. Tensile testing (Z100, Zwick Roell) was carried out at  
168 room temperature, following the ASTM E8 standard, with a constant cross-head  
169 speed of 0.5 mm/min. A minimum of four samples was tested for each condition  
170 with a clip-on extensometer to measure the strain.

## 171 ***2.2 In-situ cyclic testing and related techniques***

172 Miniature Compact-Tension (CT) samples were cut using electric discharge  
173 machining with a 0.25 mm wire. The miniaturised CT sample dimensions, shown in  
174 Figure 1a, were designed based on the ASTM E647-00 standard guidelines.  
175

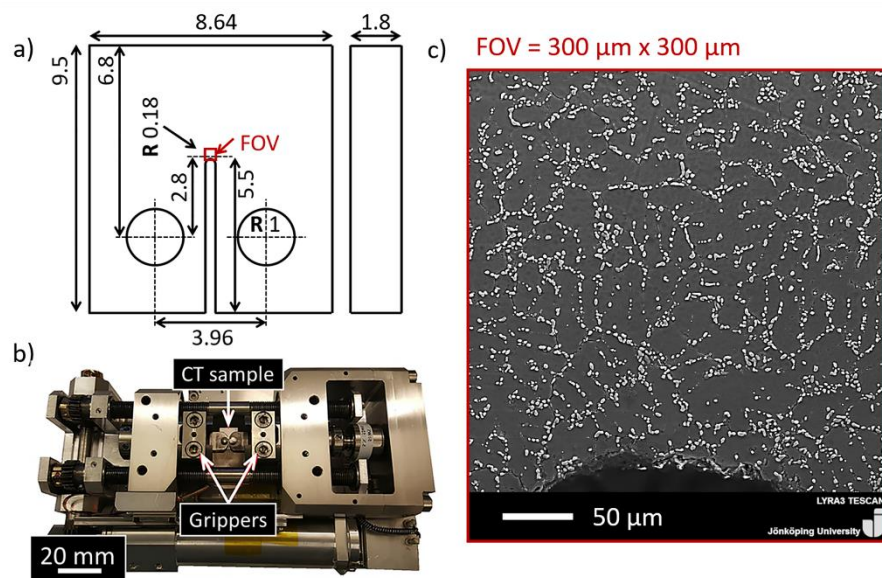


Figure 1 - a) Dimensions of the Compact-Tension (CT) sample in mm; b) miniature stage for in-situ cyclic tests; c) Field Of View (FOV) of the sample, showing the Silicon (Si) particles that formed the random pattern for subsequent Digital Image Correlation (DIC).

176 The FOV size was 300 μm x 300 μm, and it comprehended the notch tip to  
177 investigate local strain development (Fig. 1c). CT samples were electropolished (15 V  
178 for 5 s) to produce a mirror finish for SEM observations, EBSD, and DIC. EBSD maps  
179 were acquired before and after the in-situ fatigue tests to analyse the interaction  
180 between the crack and grain boundaries. In-situ cyclic tests were performed on a  
181 tensile/compression module (Kammrath & Weiss) (Fig. 1b) inside a SEM (Lyra3,  
182 Tescan) at room temperature. Before cyclic loading, the monotonic tension load to  
183 failure of the CT samples showed that the critical stress intensity factor ( $K_{Ic}$ )

184 increased with Cu content, as is shown in Table 2. The selected  $\Delta K = (1 - R) \cdot K_{\max}$  is  
 185 reported in Table 2 for each alloy, with a constant load ratio (R) of 0.2. The selected  
 186  $K_{\max}$  value is 70 % of the  $K_c$  for each alloy. The speed of loading was 8  $\mu\text{m/s}$  ( $\sim 0.1$   
 187 Hz). Two samples of each alloy were tested, and one extra sample of Alloys Cu 0  
 188 and Cu 3.0 was investigated for Focused Ion Beam (FIB) slicing.

189 Table 2 - Parameters of cyclic testing.

Alloy	$K_c$ [MPa $\cdot\sqrt{\text{m}}$ ]	Preload [N]	$P_{\max}$ [N]	$K_{\max}$ [MPa $\cdot\sqrt{\text{m}}$ ]	$\Delta K$ [MPa $\cdot\sqrt{\text{m}}$ ]
Cu 0	39.3	364	312	27.4	21.9
Cu 0.5	44.4	410	354	31.1	24.9
Cu 1.5	47.6	441	379	33.3	26.7
Cu 3.0	50.2	463	400	35.2	28.1

190 DIC was performed with the MatchID commercial software (MatchID Nv) to obtain  
 191 the strain distribution on the deformed micrographs at different cycles. Eutectic Si  
 192 particles (Fig. 1c) constituted the natural random pattern for DIC, representing a  
 193 time- and cost-saving alternative to artificial patterns. Table 3 presents the  
 194 correlation parameters used for the DIC analysis, following the work of Kasvayee *et*  
 195 *al.* [32]. The resolution of the strain distribution enabled the evaluation of the role of  
 196 grain boundaries in strain development.

197 Table 3 - Correlation parameters used for digital image correlation (DIC).

Parameter	Value
Pixel size [ $\mu\text{m}$ ]	0.24
SS = Subset size [pixel]	111
ST = Step size [pixel]	11
Correlation criterion	Zero-normalised sum of squared differences
Shape function	Quadratic

Interpolation function	Bi-cubic polynomial
Displacement standard deviation [pixel]	0.1
SW = Strain window size [pixels]	15
SSR = Strain spatial resolution [pixels]	173
SSR = SS + [(SW- 1)*ST]	

198 Three-Dimensional (3D) tomography using FIB (Cobra, Orsay Physics)-SEM (Lyra3,  
199 Tescan) was used to observe the crack path in detail, providing more information  
200 than was obtained using Two-Dimensional (2D) investigations. A location ahead of  
201 the propagating crack was selected in an unloaded state, and a rough milling of ~1.7  
202  $\mu\text{A}$  at 30 kV made a trench around the Area Of Interest (AOI). Fine polishing and  
203 slicing of the AOI were conducted using a FIB current of ~30 nA at 30 keV. The  
204 thickness of each slice was 120 nm and captured around 300 SEM images at 5 keV  
205 using a high-sensitivity in-beam back-scattered electrons detector.

### 206 3. RESULTS AND DISCUSSION

#### 207 3.1 Microstructural characterisation

208 The microstructural investigations of the alloys confirmed that the SDAS and AGS  
209 were in the 8.8 - 11  $\mu\text{m}$  and 82 - 107  $\mu\text{m}$  ranges, respectively. These parameters  
210 validate that all alloys were in the same conditions of grain refinement and  
211 solidification. The morphology of Si particles plays a crucial role in the mechanical  
212 properties of the alloys, and the solution treatment spheroidised and coarsened  
213 them. Figure 2a compares the values of the area, aspect ratio and circularity of Si  
214 particles in all the considered alloys.

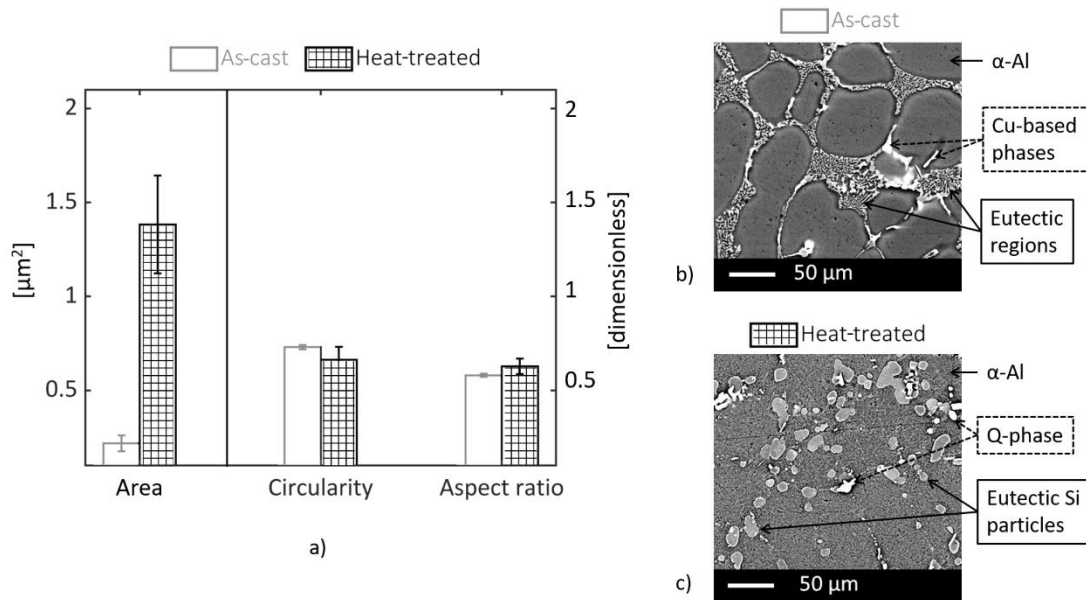


Figure 2 – Evolution of the eutectic Si particles after heat treatment: a) values of the area ( $\mu\text{m}^2$ , left y-axis) and geometrical parameters (dimensionless, right y-axis) of Si particles in the alloys; examples of microstructure for Alloy Cu 3.0 b) before and c) after heat treatment. As-cast data are reported from previous work [28]

215 The average area of the Si particles was significantly larger than in previous work  
 216 [28], up to seven times due to coarsening during heat treatment. This evolution is  
 217 evident from comparing the microstructure of Alloy Cu 3.0 before (Fig. 2b) and after  
 218 heat treatment (Fig. 2c). On the other hand, aspect ratio and circularity were not  
 219 altered much by heat treatment, as the modified Si particles already had a round  
 220 morphology in the as-cast condition [28].

221 The Si and Mg content in the centre of the primary dendrites measured by WDS  
 222 showed a slight decrease with the addition of Cu: Si changed from  $0.94 \pm 0.03$  to  $0.84$   
 223  $\pm 0.01$  wt.%, Mg went from  $0.32 \pm 0.01$  to  $0.27 \pm 0.01$  wt.%. The latter WDS  
 224 measurements confirmed the dissolution of the  $\text{Mg}_2\text{Si}$  phase in the Alloys Cu 0 and  
 225 Cu 0.5. Figure 3b presents the Cu content in the  $\alpha$ -Al dendrites measured by WDS.



226 The result for Alloy Cu 0.5 is 0.52 wt.%, and the comparison with Table 1 shows that  
 227 Cu-based phases were completely dissolved. However, traces of the Q-Al<sub>5</sub>Mg<sub>8</sub>Cu<sub>2</sub>Si<sub>6</sub>  
 228 phase were still present after heat treatment in alloys with Cu contents of 1.5 wt.%  
 229 and 3.2 wt.% (the latter depicted in Fig. 3a), while  $\theta$ -phase was dissolved. The  
 230 calculated Cu content in the remaining Q-phase (identified by EDS) summed with  
 231 the Cu content in the primary  $\alpha$ -Al matrix (measured using WDS) agree with the  
 232 overall Cu content in each alloy (Fig. 3b). This phenomenon occurred because the  
 233 solution treatment at 495 °C for one hour did not entirely dissolve the Q-phase. The  
 234 complete dissolution of the Q phases requires either a two-step solution treatment,  
 235 as presented by Wang *et al.* [33] and Toschi [34], or a treatment period longer than  
 236 one hour [35,36].

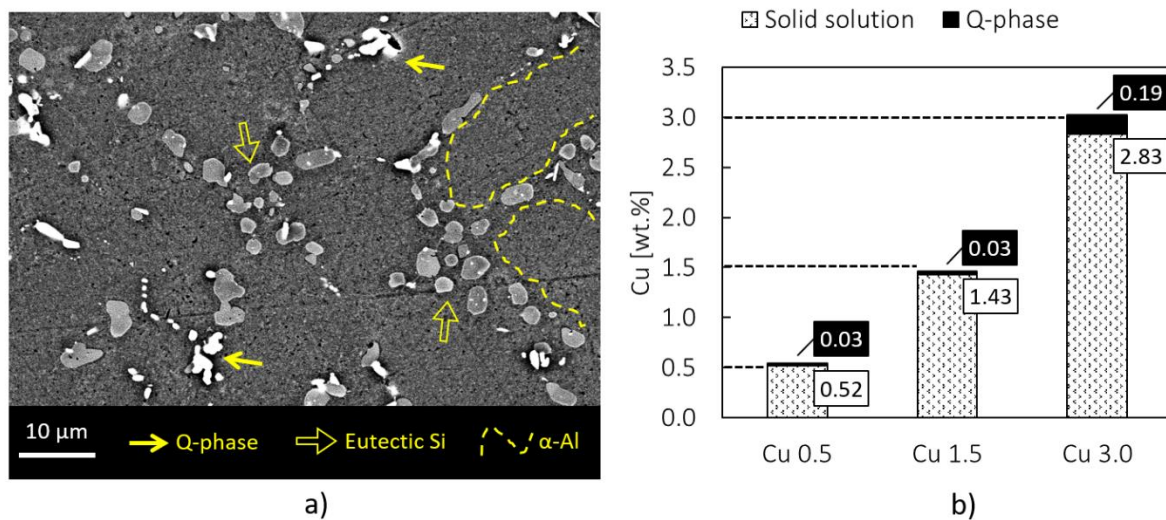


Figure 3 – a) Microstructure of heat-treated Alloy Cu 3.0; b) Cu content in solid solution and undissolved Q-phase. The latter is calculated according to the theoretical Cu content in the Q-Al<sub>5</sub>Mg<sub>8</sub>Cu<sub>2</sub>Si<sub>6</sub> phase (~20 wt.%). Dashed lines represent the overall Cu content in each alloy.

237 The heat treatment also influenced the relative distance between the secondary  
 238 phases, i.e. eutectic Si particles and Cu-based phases. Figure 4 summarise the 3NN  
 239 distance measurements.

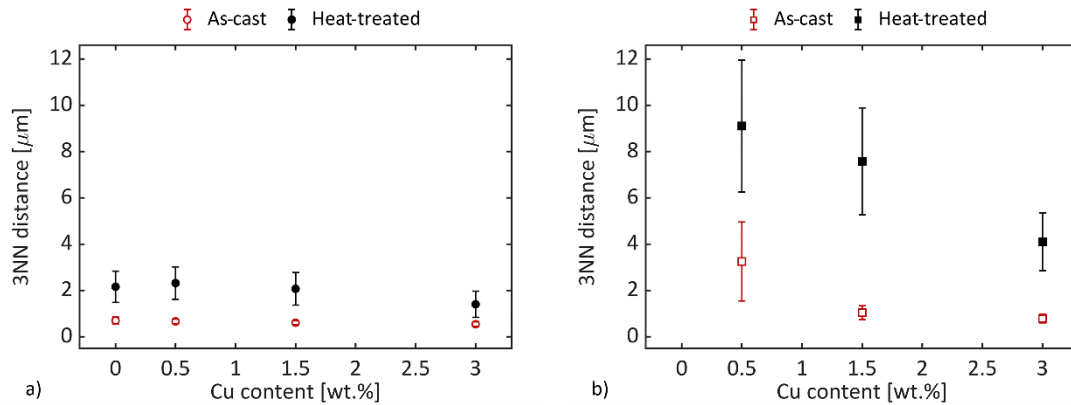


Figure 4 - Three-Nearest-Neighbour (3NN) distance of particles: a) eutectic Si; b) Q phase. The error bars represent the standard deviation.

240 Si particles (Fig. 4a) presented an average 3NN distance of 0.63 μm before heat  
 241 treatment, independent of Cu content. After heat treatment, the distance was in the  
 242 1.40 – 2.32 μm range due to the coarsening effect. On the other hand, the 3NN  
 243 distance of Q phases (Fig. 4b) decreased from 3.55 μm in Alloy Cu 0.5 to 0.78 μm in  
 244 Alloy Cu 3.0 before heat treatment. This decreasing trend mirrored the more  
 245 significant number of intermetallic particles, resulting in a closer distance to each  
 246 other. After heat treatment, the decreasing trend shifted to higher values, from 9.10  
 247 μm in Alloy Cu 0.5 to 4.10 μm in Alloy Cu 3.0 due to the partial dissolution of Q  
 248 phases.

### 249 3.2 Static mechanical properties

250 The mechanical properties showed an improvement in YS (Fig. 5a) and UTS (Fig. 5b)  
251 and a decrease in elongation (Fig. 5c) with increasing Cu concentration. The YS  
252 improved from 3 to 35 % as Cu increased from 0.5 to 3.2 wt.%, while UTS increased  
253 from 10 to 47 %. However, the reduction in elongation was negligible compared to  
254 the reduction in previous work [28], indicating the detrimental role of the Cu-rich  
255 phases. Nevertheless, the heat treatment was beneficial, particularly for alloys with  
256 Cu contents of greater than 1.5 wt.%, and in general, it homogenised the elongation  
257 response of the alloys.

258 The enhancement in YS and UTS was related to the precipitation hardening, also  
259 reported by Zheng *et al.* [15]. Comparing the increasing trend of YS and UTS after  
260 heat treatment with the WDS measurements (Fig. 3b), it is clear that the  
261 strengthening role of the Cu retained in the primary  $\alpha$ -Al matrix was coupled with  
262 the partial dissolution of the Q phases and the total dissolution of the  $\theta$  phases  
263 during heat treatment. The percentage increment in YS (Fig. 5a) mirrored the  
264 percentage improvement in HV0.01 of the primary  $\alpha$ -Al matrix (Fig. 5d), from 1 to 36  
265 %, as Cu increased from 0.5 to 3.2 wt.%. Figure 5d shows that the hardness of the  $\alpha$ -  
266 Al matrix varied in the range of 98  $\div$  130 HV0.01 for the heat-treated alloys, and the  
267 strengthening after heat treatment was related to the Cu retained in the  $\alpha$ -Al matrix  
268 (Fig. 3b).

269 The limited variation of Si morphology (aspect ratio and circularity in Fig. 2a) and  
270 3NN distance (Fig. 4a) after heat treatment was common to all of the alloys, and it  
271 underlines that the mechanical response was primarily affected by the Cu-based

272 phases in this study. The decreasing 3NN distance between Q phases (Fig. 4b)  
 273 reflected the elongation trends in both conditions. Elongation decreased with Cu  
 274 content steeply before heat treatment [28] and slightly after heat treatment, from 11  
 275 to 8 %. Similarly, the average 3NN distance of the Q phases lies in the 9 - 4  $\mu\text{m}$  range  
 276 in the heat-treated condition, while in the as-cast condition, the range was 3.5 - 1  $\mu\text{m}$   
 277 (Fig. 4b). This correlates well with the significant drop in elongation in previous  
 278 work [28].

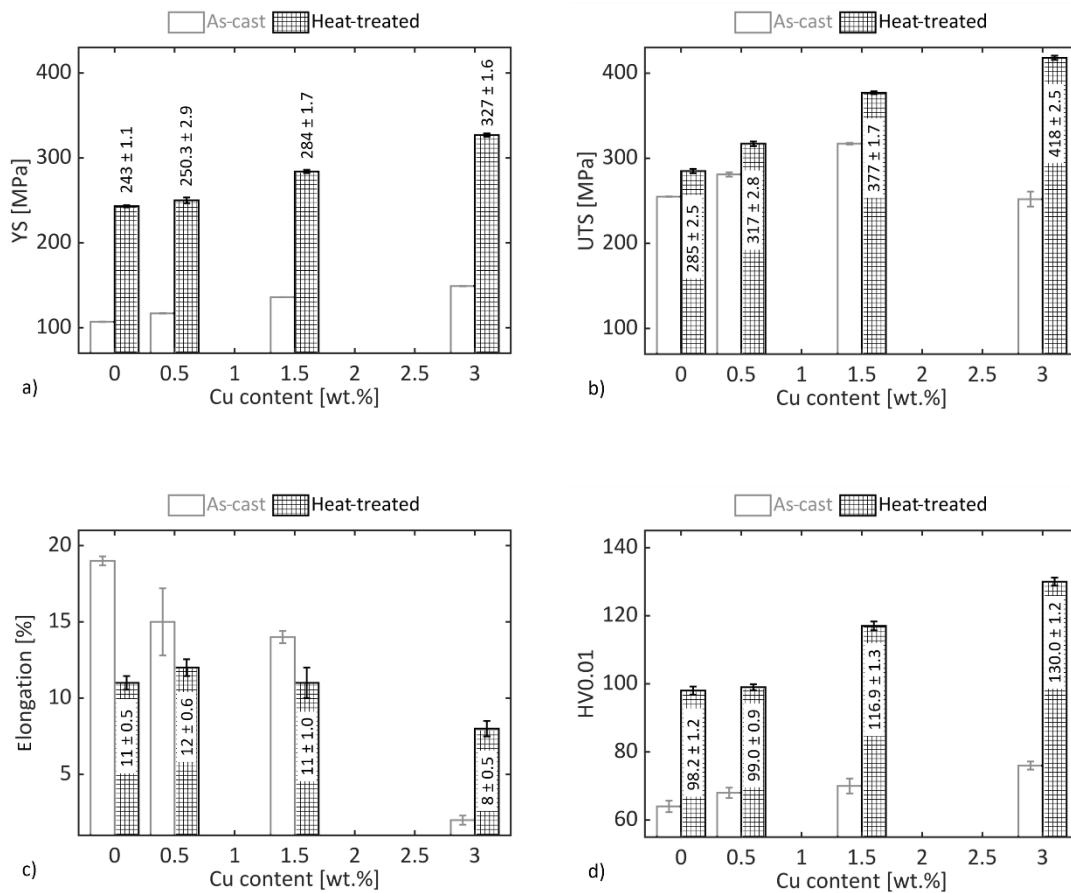


Figure 5 - Mechanical properties of the heat-treated alloys: a) Yield Strength (YS); b) Ultimate Tensile Strength (UTS); c) percentage elongation; d) Vickers microhardness (HV0.01) of the primary  $\alpha$ -Al matrix. The as-cast values from previous work [28] are depicted for direct comparison.

279 **3.3 In-situ cyclic tests – 2D observations**

280 Table 4 shows the results of the in-situ cyclic tests belong to the low-cycle fatigue  
281 regime, as the samples survived 340 - 1500 cycles. The addition of Cu content did not  
282 determine the fatigue life of the samples, as the results are randomly distributed  
283 within this range.

284 Table 4 – Summary of the in-situ cyclic tests on heat-treated CT samples.

Alloy	Sample	Cycles survived
Cu 0	A	800
	B	1500
	C	1253 (stopped for FIB milling)
Cu 0.5	A	690
	B	340
Cu 1.5	A	740
	B	1065
Cu 3.0	A	730
	B	925
	C	640 (stopped for FIB milling)

285

286 **3.3.1 Crack initiation**

287 The fatigue crack initiation in heat-treated conditions of a hypo-eutectic Al-Si cast  
288 alloy results from micro-scale defects or discontinuities at the surface and subsurface  
289 levels. A 2D perspective indicated that the crack initiation appeared in the primary  
290 dendrite in the Cu-free alloy (Fig. 6a-b and highlighted in Fig. 7a); Cu additions  
291 moved it to the interdendritic regions (Fig. 6c-h). Figure 6g-h shows that the  
292 nucleation sites were observed at the grain boundaries (dashed yellow lines, over-  
293 imposed from the EBSD maps) in Alloy Cu 3.0. Figure 6h shows two cracks that  
294 originated from the same point and follow the grain boundaries. On the other hand,

295 Figure 6a-f shows cracks in the grain centre in all of the investigated specimens with  
296 lower Cu concentrations. From observing the polished surfaces, it can be concluded  
297 that crack nucleation occurred in the grain for Cu contents up to 1.5 wt.% and  
298 aligned with the grain boundary for Alloy Cu 3.0. Moreover, defects or  
299 discontinuities at the sub-micron scale, such as precipitates, that can act as initiation  
300 sites were not observed in this work and need different investigative approaches.

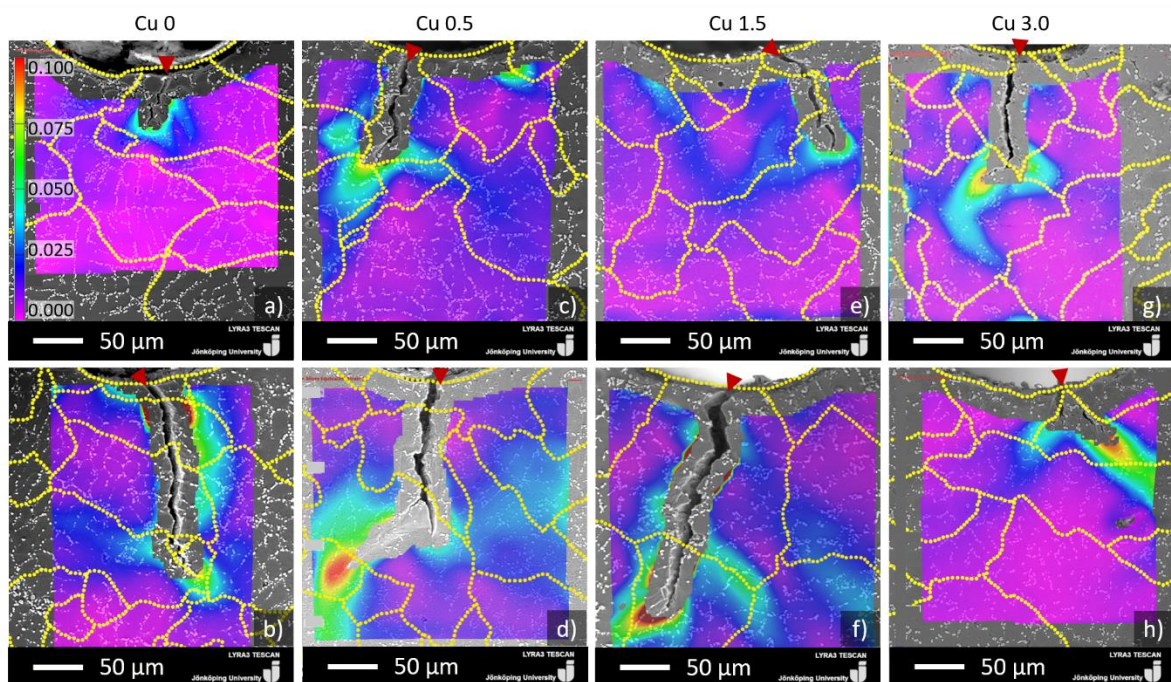


Figure 6 - Crack propagation in all heat-treated alloys combining EBSD and Digital Image Correlation (DIC): a-b) Alloy Cu 0; c-d) Alloy Cu 0.5; e-f) Alloy Cu 1.5; g-h) Alloy Cu 3.0. The dashed yellow lines represent grain boundaries, super-imposed from EBSD, and red arrows point to the initiation sites. The colour bar represents the von Mises equivalent strain and is valid for all the frames.

### 301 3.3.2 Crack propagation

302 Crack propagation is generally expected to follow the least resistance path, offered  
303 by weak or damaged microstructural features ahead of the crack tip. The EBSD maps  
304 generated were super-imposed on the SEM micrograph, and the dashed yellow lines  
305 in Figure 6 represent the grain boundaries.

306 In Alloy Cu 0 (Fig. 6b), the crack propagated along trans-granular paths for the first  
307 150  $\mu\text{m}$  in the FOV, then continued following the grain boundaries. The propagation  
308 followed a mixed path that crossed the dendrite arms and followed the eutectic Si  
309 particles.

310 Crack propagation shifted slightly to the interdendritic regions with the Cu addition  
311 of 0.5 wt.% (Fig. 6c-d). This shift occurred due to the enhanced strength in  $\alpha\text{-Al}$   
312 matrix strength due to the retained Cu, evidenced by WDS measurements in Figure  
313 3b and hardness values in Figure 5d. The DIC results for Alloy Cu 0.5 highlighted  
314 that increment of strain concentration occurred at the grain boundaries. However,  
315 the main propagation path was trans-granular.

316 In Alloy Cu 1.5 (Fig. 6e-f), the propagation is mainly trans-granular with some  
317 intergranular segments, despite the increased strain concentration at the grain  
318 boundaries.

319 Concerning Alloy Cu 3.0 (Fig. 6g-h), the 2D perspective showed that crack growth  
320 tended to follow the grain boundaries. Figure 6g shows that the propagation later  
321 continued across the grains. In Figure 6h, two cracks are propagated under the  
322 dashed yellow lines along the grain boundaries and determined the higher strain  
323 highlighted by the DIC.

324 The crack propagation appears to be mixed on the surface, most as trans-granular  
325 and some inter-granular paths were present in all alloys. DIC in Figure 6 highlighted  
326 that grain boundaries could determine localised strain, and it can ease crack  
327 propagation by determining the occurrence of intergranular segments (Fig. 6h).  
328 More often, the highest strain path is not determined by the grain boundaries (Fig.  
329 6d). Other works [37,38] concluded that grain boundaries serve to distribute  
330 deformation in the microstructure, aligning with what is observed about crack  
331 propagation in Figure 6. Han *et al.* [38] investigated short fatigue crack growth in Al-  
332 7Si-0.4Mg alloy and reported that the grain boundaries deaccelerate crack  
333 propagation by a shielding effect. Nevertheless, the role of grain boundaries is based  
334 only on limited 2D data in the present study, and more investigation is required for a  
335 comprehensive assessment.

336 The increased Cu content in the  $\alpha$ -Al matrix, as precipitates, provide significant  
337 obstacles for the dislocation movement, as shown by Roy *et al.* [17] and Saito *et al.*  
338 [14]. This phenomenon transfers the propagation from the  $\alpha$ -Al matrix in Alloy Cu 0  
339 (yellow arrows in Fig. 7a) to the eutectic regions in Alloy Cu 3.0 (red arrows in Fig.  
340 7b), with an increased number of damaged Si particles and Q phases. This  
341 phenomenon is related to the primary matrix strengthening observed previously  
342 (Fig. 5d) in the present work. Similar behaviour was observed in Alloy Cu 1.5,  
343 whereas the propagation changed from trans-dendritic to inter-dendritic.



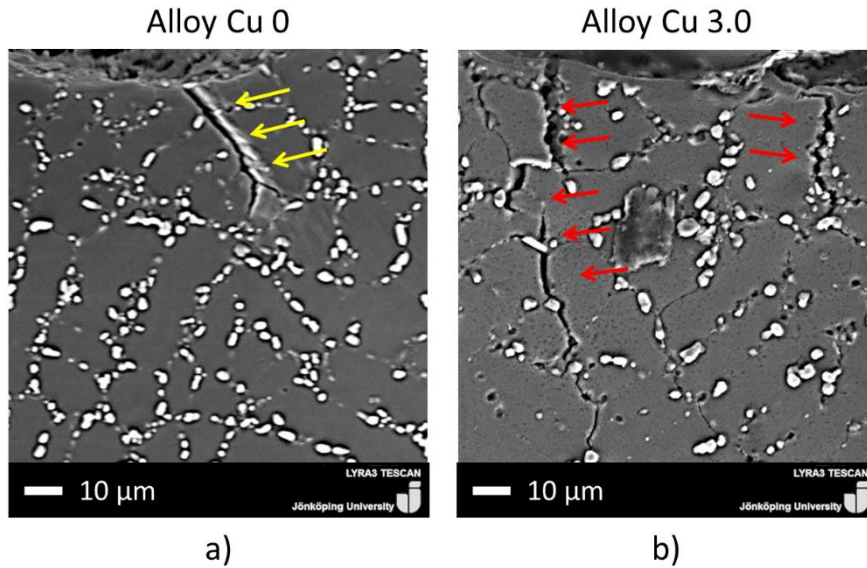


Figure 7 – Examples of crack path: a) trans-dendritic in Alloy Cu 0, pointed by yellow arrows; b) inter-dendritic in Alloy Cu 3.0, pointed by red arrows.

344 Another significant change was the presence of multiple secondary cracks appearing  
 345 in the FOV during cyclic loading, indicated by arrows in Figure 8. These secondary  
 346 cracks followed the Si particles and Q phases (Fig. 8a) and opened up as cyclic  
 347 loading continued (Fig. 8b). The cracks followed the interdendritic regions and  
 348 connected the secondary phases due to the reduced 3NN distance between the Q  
 349 phases, as shown in Figures 8c and d.

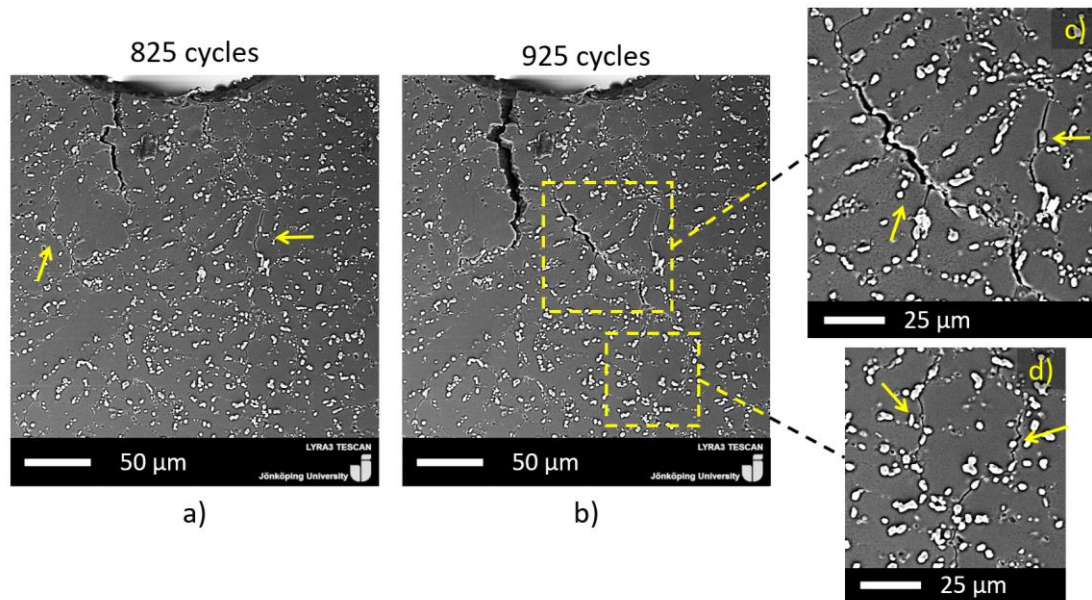


Figure 8 - Development of secondary cracks (indicated by yellow arrows) in heat-treated Alloy Cu 3.0: a) 825 cycles; b) 925 cycles; c-d) magnified micrographs of secondary cracks in (b).

350 Secondary cracks were not evident in the FOV of Alloy Cu 0 and Cu 0.5. Moreover,  
 351 some cracks were detected in Cu 1.5, and many secondary cracks developed in Alloy  
 352 Cu 3.0 (Fig. 8). The  $\alpha$ -Al matrix strength governed the stress concentrations in the  
 353 alloy and, consequently, the propagation behaviour. Inter-dendritic secondary  
 354 cracks developed along the lateral dendrite tips with increasing  $\alpha$ -Al matrix  
 355 strength. The material within the FOV was involved in dissipating the deformation  
 356 that resulted from the cyclic loading, not only the primary crack but also the  
 357 secondary cracks in the interdendritic regions (Fig. 8c-d). This increasing trend of  
 358 secondary crack development aligns well with the decreasing 3NN distance between  
 359 Cu-based phases (Fig. 4b), which enabled the connection between small cracks.  
 360 The influence of the strengthened  $\alpha$ -Al matrix on the evolution of the crack path can  
 361 also be assessed with crack tortuosity. Figure 9 shows that tortuosity varied within

362 1.1-1.2 for the heat-treated alloys, a more limited range than what found in previous  
 363 work [28]. Given the constant values of AGS and SDAS for the alloys in all  
 364 conditions, the evolution of tortuosity with the Cu content accords well with the  
 365 elongation results in Figure 5c.

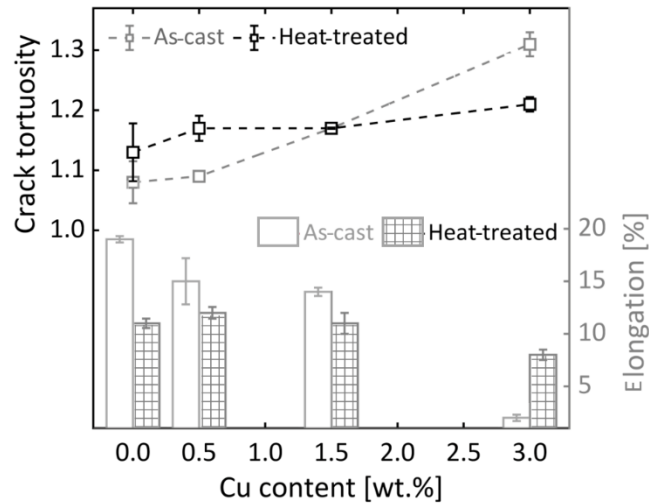


Figure 9 - Comparison of crack tortuosity and elongation trends in the as-cast and heat-treated conditions. The trend lines are meant to guide the eye. The as-cast values from previous work [28] are depicted for direct comparison.

366 In the heat-treated alloys, the constant crack tortuosity trend was related to a  
 367 constant ductility trend. The values for tortuosity for Alloy Cu 1.5 were the same  
 368 before [28] and after heat treatment, with a limited difference in elongation (Fig. 9).  
 369 In previous work [28], Alloy Cu 3.0 had a rapid failure without any previously  
 370 detectable deformation. However, after heat treatment, the crack propagation was  
 371 not sudden and could be followed in the FOV during in-situ cyclic loadings at all  
 372 levels of Cu concentration. Furthermore, the improved elongation (Fig. 5c) coupled  
 373 with the enhanced hardness of the primary  $\alpha$ -Al matrix (Fig. 5d) compared to  
 374 previous work [28] highlights that Cu-containing alloys benefit from an excellent

375 balance between strength and ductility with heat treatment. With this condition, the  
376 damage is progressive during cyclic loading rather than sudden, as was previously  
377 reported [28].

378

### 379 *3.4 In-situ cyclic tests – 3D evaluations*

#### 380 *3.4.1 FIB slicing*

381 The 3D evaluation using FIB slicing of the extreme conditions, Alloys Cu 0 and Cu  
382 3.0, was performed to investigate the development of secondary cracks in Figure 8.

383 Figures 10a and d show the AOI (white rectangles) for the FIB sections investigated

384 of Alloy Cu 0 (Fig. 6a) and Cu 3.0 (Fig. 6h). A 2D perspective showed that crack

385 propagation stopped at the grain boundary during the cyclic testing of Alloy Cu 0.

386 At the beginning of the FIB sections (Fig. 10b), no crack was visible in the thickness

387 but was evident on the surface (white arrow). The bright phases in Section 1 (black

388 arrows in Fig. 10b) are Fe-containing phases, as confirmed by EDS measurements.

389 Moreover, investigating the sections moving toward the crack showed a limited

390 amount of cracked or debonding phases. In Section 170 (Fig. 10c), a crack opened

391 from the underlying volume (red arrows), indicating crack initiation below the

392 surface.

393 As the Cu concentration increased to 3.2 wt.% (Fig. 10d), multiple cracks were visible

394 on the surface of the sample. The white arrow in Figure 10e points to the surface

395 crack, which extended to the material underneath. In the FIB sections, a significant

396 amount of cracked and debonded phases was present ahead of the crack tip

397 compared to Alloy Cu 0. Moreover, the sections toward the crack (Section 250 in Fig.  
 398 10f) clearly shows that the crack propagated from below (red arrows) in the Cu  
 399 phases, which were close to each other 4  $\mu\text{m}$  on average (Fig. 4b).  
 400 These insights on crack propagation from subsurface material also support the  
 401 appearance of the secondary cracks visible in Figure 8b. These might be the final  
 402 parts of cracks that developed underneath, from coalescence between cracked  
 403 particles, and ultimately reached the polished surface appearing as secondary cracks.

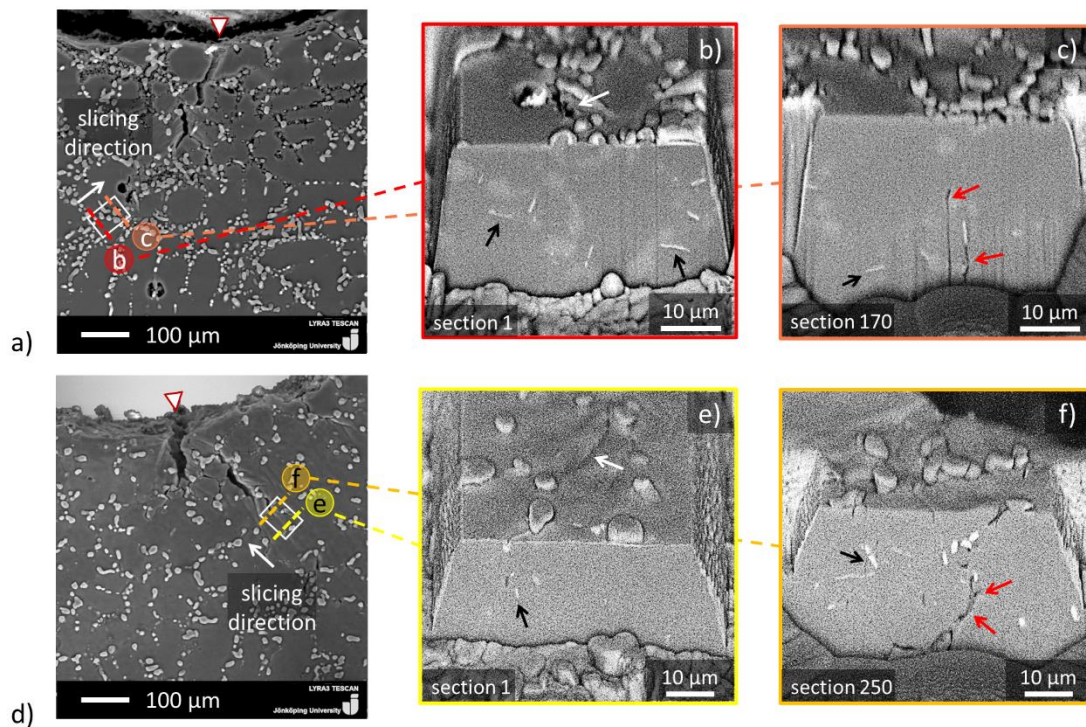


Figure 10 - FIB sections used to investigate the material around the crack in heat-treated alloys. a) Alloy Cu 0, test stopped at 1253 cycles; b) and c) show related sections; d) Alloy Cu 3.0, test stopped at 640 cycles; e) and f) show related sections. The black arrows point to Fe compounds, the white arrows point to superficial cracks, and the red arrows point to the crack coming from underneath.

404 Figure 11b and d shows the 3D reconstruction of the volume removed by FIB slicing,  
 405 showing cracks as red and intermetallic phases as blue in the alloys. Moreover, the  
 406 arrows in the 2D view Figure 11a and c follow the same colour legend. Alloy Cu 0



407 (Fig. 11a) has few cracks in the investigated AOI, while Alloy Cu 3.0 (Fig. 11c)  
 408 contains significantly more cracks. In Alloy Cu 0 (Fig. 11b), the crack appears from  
 409 below, as visualised in Fig 10c. In alloy Cu 3.0 (Fig. 11d), more connected  
 410 microcracks are observed in the AOI. Furthermore, the 3D reconstruction confirms  
 411 that cracks are frequently visible in connection with intermetallic phases, as  
 412 previously observed in 2D slicing (Fig. 10f).

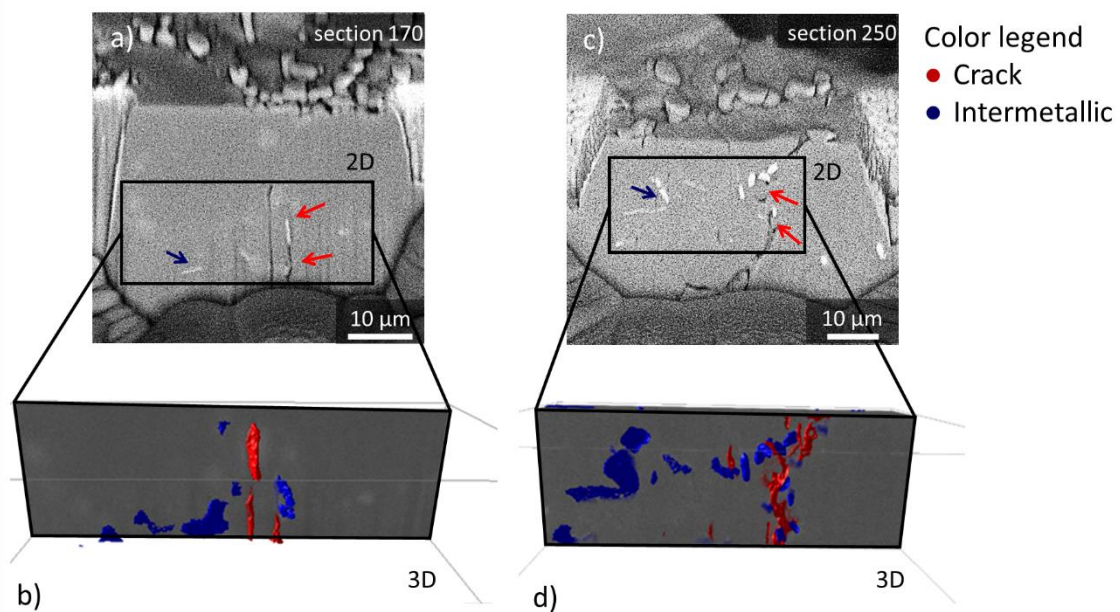


Figure 11 – 3D reconstruction of the FIB sections of the crack in heat-treated alloys. a) FIB section of Alloy Cu 0, test stopped at 1253 cycles, and b) related 3D reconstruction; c) FIB section in Alloy 3.0 Cu, test stopped at 640 cycles, and d) related 3D reconstruction. The red arrows show the cracks, and the blue arrows show the intermetallic phases.

### 413 3.4.2 Fracture surface analyses of CT samples

414 Investigations of fracture surfaces showed that initiation sites were distributed along  
 415 with the thickness of the CT samples. This outcome aligns with the FIB sections in  
 416 Figures 10 and 11, which showed cracks originating in the subsurface area. The  
 417 supposed initiation points observed in the 2D view in Figures 6a and h are a later

418 stage of the crack propagation because of the triaxial stress state. The crack  
419 propagation zone (highlighted with the dashed yellow line in Fig. 12a and d) was  
420 distinct from the final fracture zone in the investigated alloys. Moreover, all of the  
421 samples show shear lips (solid yellow lines in Fig. 12a and d, showing Alloys Cu 0  
422 and Cu 3.0) with significant height differences. Magnified views are depicted in  
423 Figures 12c and 12f for Alloys Cu 0 and Cu 3.0, respectively. The fracture  
424 morphology of shear lips indicated a ductile behaviour, and similar dimples  
425 characterised the entire final failure zone in all of the alloys.

426 In Alloy Cu 0, the fracture surface at the notch showed that initiation started at two  
427 locations, each with a different crack propagation orientation. The magnified view of  
428 the propagation zone (Fig. 12b) shows Si particles rising from the surface. This  
429 feature suggests that the Si particles were debonded and pulled out from the  $\alpha$ -Al  
430 matrix during crack propagation.

431 In Alloy Cu 3.0, the initiation started at multiple points, and several cracks appeared  
432 in the propagation zone. In the enlarged view (Fig. 12e), a mixture of debonded Si  
433 particles and cracking around particles are visible; these occurred due to the  
434 enhanced strength of the  $\alpha$ -Al matrix. The difference from previous work [28] was  
435 significant for the alloy with 3.2 wt.% Cu, in which a rapid failure occurred due to  
436 the presence of a significantly greater quantity of Q and  $\theta$  phases. However, the  
437 reduction in the number of Cu-rich particles in Alloy Cu 3.0 after heat treatment  
438 changed the propagation behaviour of the alloy, and the crack path was visible in  
439 Figure 6g-h.

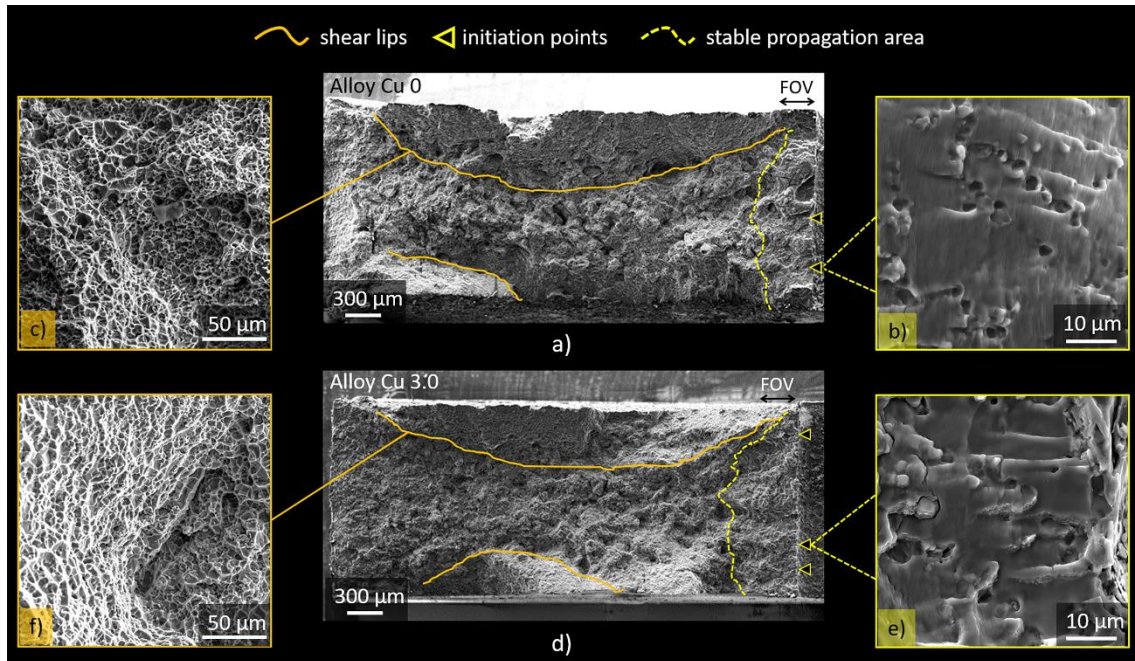


Figure 12 - Fracture surfaces of heat-treated Compact-Tension (CT) samples: a) Alloy Cu 0, b) and c) are magnified views of initiation points and shear lips, respectively, in a); d) Alloy Cu 3.0, e) and f) are magnified views of initiation points and shear lips, respectively, in d).

440 In summary, the presented results show the critical role of Cu in Al-Si-Mg cast alloys  
 441 to determine both crack initiation and propagation. The addition of Cu above 1.5  
 442 wt.% transfers the propagation from the primary  $\alpha$ -Al matrix to the eutectic regions  
 443 because of the complex interaction between the strengthened  $\alpha$ -Al matrix and  
 444 intermetallic phases.

#### 445 4. CONCLUDING REMARKS

446 This study investigated the influence of microstructural features on tensile  
 447 properties and crack development during cyclic loading in heat-treated Al-7Si-Mg  
 448 alloys with different Cu additions. The following conclusions can be drawn:



449 · The limited variation of Si particles after heat treatment, in terms of morphology  
450 and three-nearest-neighbour distance, shown that mechanical properties are  
451 affected by Cu-based phases and primary matrix to a great extent.

452 · The addition of Cu resulted in a continuous improvement in YS and UTS up to  
453 327 and 418 MPa, respectively. The parallel decrease in elongation was limited,  
454 from 11 % to 8 %, while crack tortuosity in CT samples followed the opposite  
455 trend with Cu additions.

456 · Crack initiation occurred at multiple sites in the thicknesses of the samples, as  
457 clarified by FIB sections and fracture surfaces. From the 2D perspective, crack  
458 propagation appeared mostly trans-granular in all the materials. However, the  
459 crack moved from trans-dendritic to inter-dendritic as the Cu content increased.

460 · The primary  $\alpha$ -Al matrix was the most significant feature to influence crack  
461 propagation, as the strengthening effect of Cu influenced the development of  
462 inter-dendritic secondary cracks. These formed from the coalescence of small  
463 cracks that originated in the Si particles and intermetallic phases.

464 The 2D observations were interpreted differently after the three-dimensional  
465 insights provided by FIB sections and fracture surfaces. This study provided a  
466 deeper understanding of the relationship between crack development and  
467 microstructural features, useful for optimised structural components. Future studies  
468 will investigate the variation of other microstructural features that influence the  
469 mechanical response.

470

471 **Funding:** This research did not receive any specific grant from funding agencies in the public,  
472 commercial, or not-for-profit sectors.

473 **Data availability:** The data that support the findings of this study are available from the  
474 corresponding author on reasonable request.

475 **CRedit authorship contribution statement:** Toni Bogdanoff: Investigation, Data curation, Writing -  
476 Original draft preparation. Lucia Lattanzi: Investigation, Data curation, Writing - Original draft  
477 preparation. Mattia Merlin: Supervision, Writing - Reviewing and Editing. Ehsan Ghassemali:  
478 Visualisation, Methodology, Writing - Reviewing and Editing. Anders E.W. Jarfors: Supervision,  
479 Writing - Reviewing and Editing. Salem Seifeddine: Conceptualisation, Supervision, Resources,  
480 Writing - Reviewing and Editing.

481 **Declaration of competing interest:** The authors declare that they have no known competing financial  
482 interests or personal relationships that could have appeared to influence the work reported in this  
483 paper.

484 **Acknowledgements:** The authors gratefully acknowledge Mr. Riccardo Castiglieri for help in  
485 performing part of the experimental work.

486

## 487 REFERENCES

488 [1] A.C. Serrenho, J.B. Norman, J.M. Allwood, The impact of reducing car weight  
489 on global emissions: the future fleet in Great Britain, *Phil. Trans. R. Soc. A* (2017)  
490 20160364.

491 [2] N. Hooftman, M. Messagie, J. Van Mierlo, T. Coosemans, A review of the  
492 European passenger car regulations – Real driving emissions vs local air quality,  
493 *Renewable and Sustainable Energy Reviews* 86 (2018) 1-21.

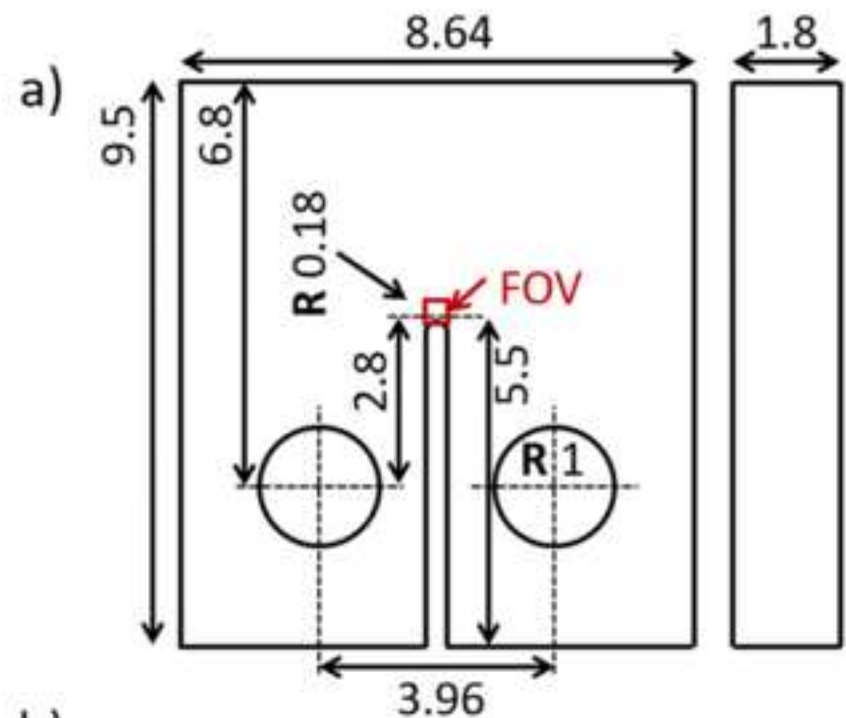
494 [3] E-mobility 2020 – Materials selection for a more sustainable automotive future,  
495 *Hydro papers*, May 2020, 1-24.

- 496 [4] R. Taghiabadi, A. Fayegh, A. Pakbin, M. Nazari, M. Ghoncheh, Quality index  
497 and hot tearing susceptibility of Al-7Si-0.35 Mg-xCu alloys, Transactions of  
498 Nonferrous Metals Society of China 28(7) (2018) 1275-1286.
- 499 [5] S. Seifeddine, E. Sjölander, T. Bogdanoff, On the role of copper and cooling rates  
500 on the microstructure, defect formations and mechanical properties of Al-Si-Mg  
501 alloys, Materials Sciences and Applications 4 (2013) 171-178.
- 502 [6] S. Shabestari, H. Moemeni, Effect of copper and solidification conditions on the  
503 microstructure and mechanical properties of Al-Si-Mg alloys, Journal of Materials  
504 Processing Technology 153 (2004) 193-198.
- 505 [7] C. Caceres, M. Djurdjevic, T. Stockwell, J. Sokolowski, The effect of Cu content  
506 on the level of microporosity in Al-Si-Cu-Mg casting alloys, Scripta Materialia 40(5)  
507 (1999) 631-637.
- 508 [8] L. Ceschini, S. Messieri, A. Morri, S. Seifeddine, S. Toschi, M. Zamani, Effect of  
509 Cu addition on overaging behaviour, room and high temperature tensile and  
510 fatigue properties of A357 alloy, Transactions of Nonferrous Metals Society of  
511 China 30 (2020) 2861-2878.
- 512 [9] E. Cerri, M.T. Di Giovanni, E. Ghio, A study of intermetallic phase stability in  
513 Al-Si-Mg casting alloy: The role of Cu additions, Metallurgia Italiana 112 (2020) 7-  
514 8, 37-47.
- 515 [10] J. Baskaran, P. Raghuvaran, S. Ashwin, Experimental investigation on the effect  
516 of microstructure modifiers and heat treatment influence on A356 alloy, Materials  
517 Today: Proceedings 37-2 (2021) 3007-3010.
- 518 [11] S. Beroual, Z. Boumerzoug, P. Paillard, Y. Borjon-Piron. Effects of heat  
519 treatment and addition of small amounts of Cu and Mg on the microstructure and  
520 mechanical properties of Al-Si-Cu and Al-Si-Mg cast alloys, Journal of Alloys and  
521 Compounds 784 (2019) 1026-1035.
- 522 [12] M.T. Di Giovanni, E.A. Mørtzell, T. Saito, S. Akhtar, M. Di Sabatino, Y. Li, E.  
523 Cerri, Influence of Cu addition on the heat treatment response of A356 foundry  
524 alloy, Materials Today Communications 19 (2019) 342-348.

- 525 [13] E.A. Mørtzell, F. Qian, C.D. Marioara, Y. Li, Precipitation in an A356 foundry  
526 alloy with Cu additions-A transmission electron microscopy study, *Journal of*  
527 *Alloys and Compounds* 785 (2019) 1106-1114.
- 528 [14] T. Saito, E.A. Mørtzell, S. Wenner, C.D. Marioara, S.J. Andersen, J. Friis, K.  
529 Matsuda, R. Holmestad, Atomic structures of precipitates in Al–Mg–Si alloys with  
530 small additions of other elements, *Adv. Eng. Mater.* 20(7) (2018) 1800125.
- 531 [15] Y. Zheng, W. Xiao, S. Ge, W. Zhao, S. Hanada, C. Ma, Effects of Cu content and  
532 Cu/Mg ratio on the microstructure and mechanical properties of Al–Si–Cu–Mg  
533 alloys, *Journal of Alloys and Compounds* 649 (2015) 291-296.
- 534 [16] C. Caceres, I.L. Svensson, J. Taylor, Strength-ductility behaviour of Al-Si-Cu-  
535 Mg casting alloys in T6 temper, *International Journal of Cast Metals Research* 15(5)  
536 (2003) 531-543.
- 537 [17] S. Roy, L.F. Allard, A. Rodriguez, T.R. Watkins, A. Shyam, Comparative  
538 Evaluation of Cast Aluminum Alloys for Automotive Cylinder Heads: Part I—  
539 Microstructure Evolution, *Metallurgical and Materials Transactions A* (2017) 1-14.
- 540 [18] S. Roy, L.F. Allard, A. Rodriguez, W.D. Porter, A. Shyam, Comparative  
541 evaluation of cast aluminum alloys for automotive cylinder heads: Part II—  
542 mechanical and thermal properties, *Metallurgical and Materials Transactions A*  
543 48(5) (2017) 2543-2562.
- 544 [19] E. Sjölander, S. Seifeddine, The heat treatment of Al–Si–Cu–Mg casting alloys,  
545 *Journal of Materials Processing Technology* 210(10) (2010) 1249-1259.
- 546 [20] K.S. Chan, P. Jones, Q. Wang, Fatigue crack growth and fracture paths in sand  
547 cast B319 and A356 aluminum alloys, *Materials Science and Engineering: A* 341(1-  
548 2) (2003) 18-34.
- 549 [21] D.A. Lados, D. Apelian, P.E. Jones, J.F. Major, Microstructural mechanisms  
550 controlling fatigue crack growth in Al–Si–Mg cast alloys, *Materials Science and*  
551 *Engineering: A* 468 (2007) 237-245.

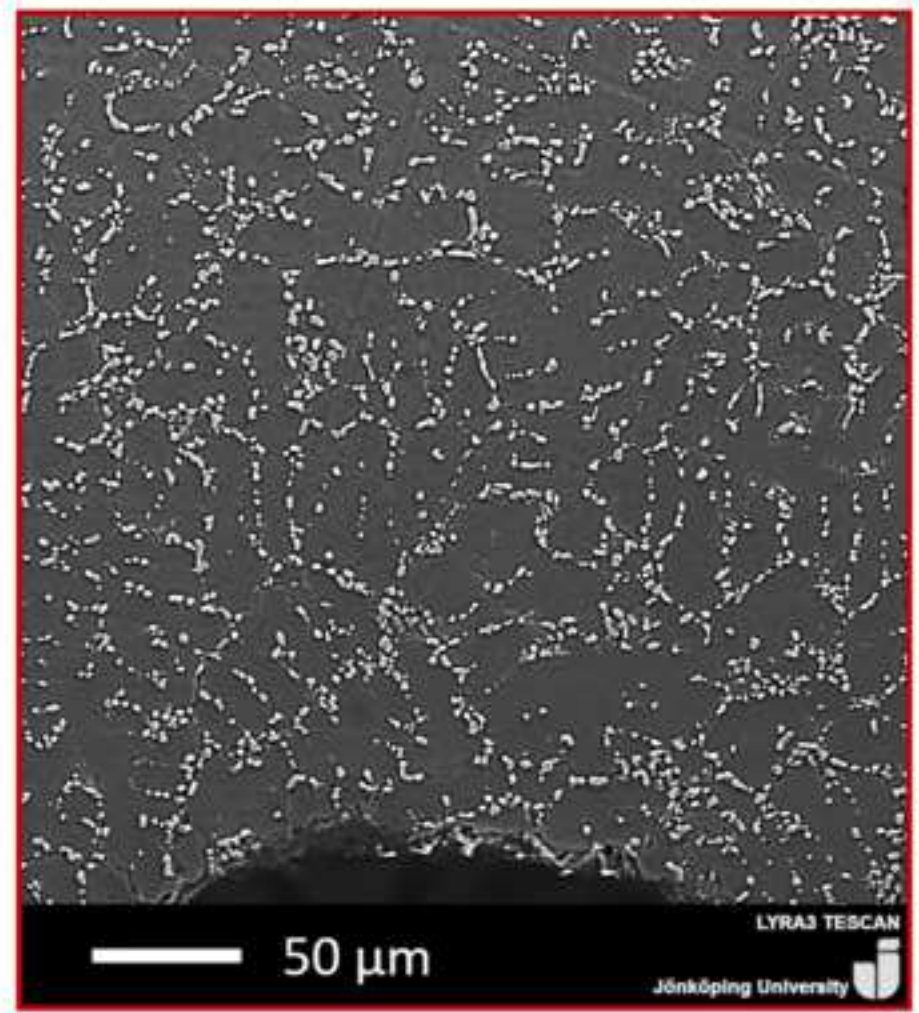
- 552 [22] D.A. Lados, D. Apelian, Fatigue crack growth characteristics in cast Al–Si–Mg  
553 alloys: Part I. Effect of processing conditions and microstructure, *Materials Science*  
554 *and Engineering: A* 385(1-2) (2004) 200-211.
- 555 [23] D.A. Lados, D. Apelian, L. Wang, Solution treatment effects on microstructure  
556 and mechanical properties of Al-(1 to 13 pct) Si-Mg cast alloys, *Metallurgical and*  
557 *Materials Transactions B* 42(1) (2011) 171-180.
- 558 [24] D. Tomazincic, M. Borovinsek, Z. Ren, J. Klemenc, Improved prediction of low-  
559 cycle fatigue life for high-pressure die-cast aluminium alloy AlSi9Cu3 with  
560 significant porosity, *International Journal of Fatigue* 144 (2021) 106061.
- 561 [25] J. Hirsch, *Automotive Trends in Aluminium - The European Perspective*,  
562 *Materials Forum* 28 (2004) 15-23.
- 563 [26] G.K. Sigworth, R.J. Donahue, The metallurgy of Aluminum alloys for structural  
564 high-pressure die castings, *International Journal of Metal Casting* (2020).
- 565 [27] T. Lu, J. Wu, Y. Pan, S. Tao, Y. Chen, Optimising the tensile properties of Al-  
566 11Si-0.3Mg alloys: role of Cu addition, *Journal of Alloys and Compounds* 631  
567 (2015) 276-282.
- 568 [28] T. Bogdanoff, L. Lattanzi, M. Merlin, E. Ghassemali, S. Seifeddine, The  
569 Influence of Copper Addition on Crack Initiation and Propagation in an Al-Si-Mg  
570 Alloy During Cyclic Testing, *Materialia* (2020) 100787.
- 571 [29] E. Sjölander, S. Seifeddine, Artificial ageing of Al–Si–Cu–Mg casting alloys,  
572 *Materials Science and Engineering: A* 528(24) (2011) 7402-7409.
- 573 [30] J.J. Friel, *Practical guide to image analysis*, ASM international 2000.
- 574 [31] Vandersluis, E., Ravindran, C. Comparison of Measurement Methods for  
575 Secondary Dendrite Arm Spacing. *Metallogr. Microstruct. Anal.* 6, 89–94 (2017).  
576 <https://doi.org/10.1007/s13632-016-0331-8>
- 577 [32] K.A. Kasvayee, E. Ghassemali, K. Salomonsson, S. Sujakhu, S. Castagne, A.E.  
578 Jarfors, Microstructural strain mapping during in-situ cyclic testing of ductile iron,  
579 *Materials Characterization* 140 (2018) 333-339.

- 580 [33] X. Wang, J. Embury, W. Poole, S. Esmaili, D. Lloyd, Precipitation  
581 strengthening of the aluminum alloy AA6111, *Metallurgical and Materials*  
582 *Transactions A* 34(12) (2003) 2913-2924.
- 583 [34] S. Toschi, Optimisation of A354 Al-Si-Cu-Mg Alloy Heat Treatment: Effect on  
584 Microstructure, Hardness, and Tensile Properties of Peak Aged and Overaged  
585 Alloy, *Metals* 8(11) (2018) 961.
- 586 [35] E. Sjölander, S. Seifeddine, Optimisation of solution treatment of cast Al-7Si-0.3  
587 Mg and Al-8Si-3Cu-0.5 Mg alloys, *Metallurgical and Materials Transactions A* 45(4)  
588 (2014) 1916-1927.
- 589 [36] Y. Han, A. Samuel, F. Samuel, S. Valtierra, H. Doty, 08-014 Effect of Solution  
590 Heat Treatment Type on the Dissolution of Copper Phases in Al-Si-Cu-Mg Type  
591 Alloys, *Transactions of the American Foundrymen's Society* 116 (2008) 79.
- 592 [37] A.C. Magee, L. Ladani, Representation of a microstructure with bimodal grain  
593 size distribution through crystal plasticity and cohesive interface modelling,  
594 *Mechanics of Materials* 82 (2015) 1-12.
- 595 [38] S.W. Han, S. Kumai, A. Sato, Effects of solidification structure on short fatigue  
596 crack growth in Al-7%Si-0.4%Mg alloy castings, *Materials Science and Engineering*  
597 *A* 332 (2002) 56-63.

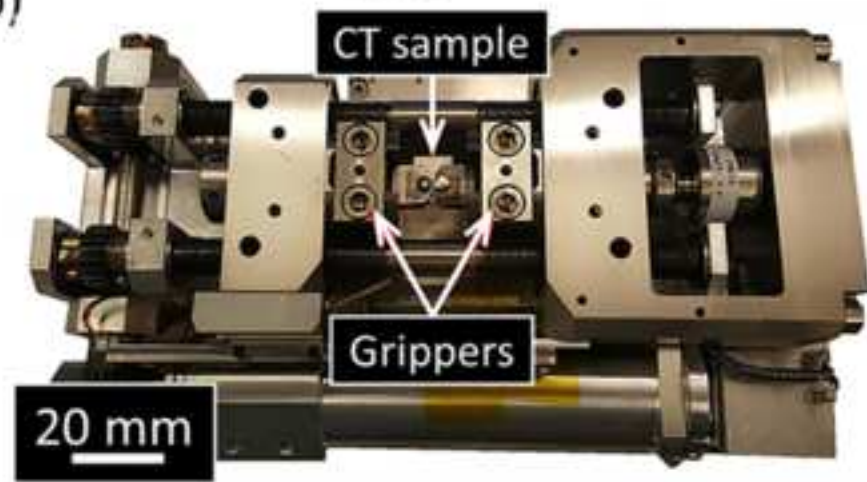


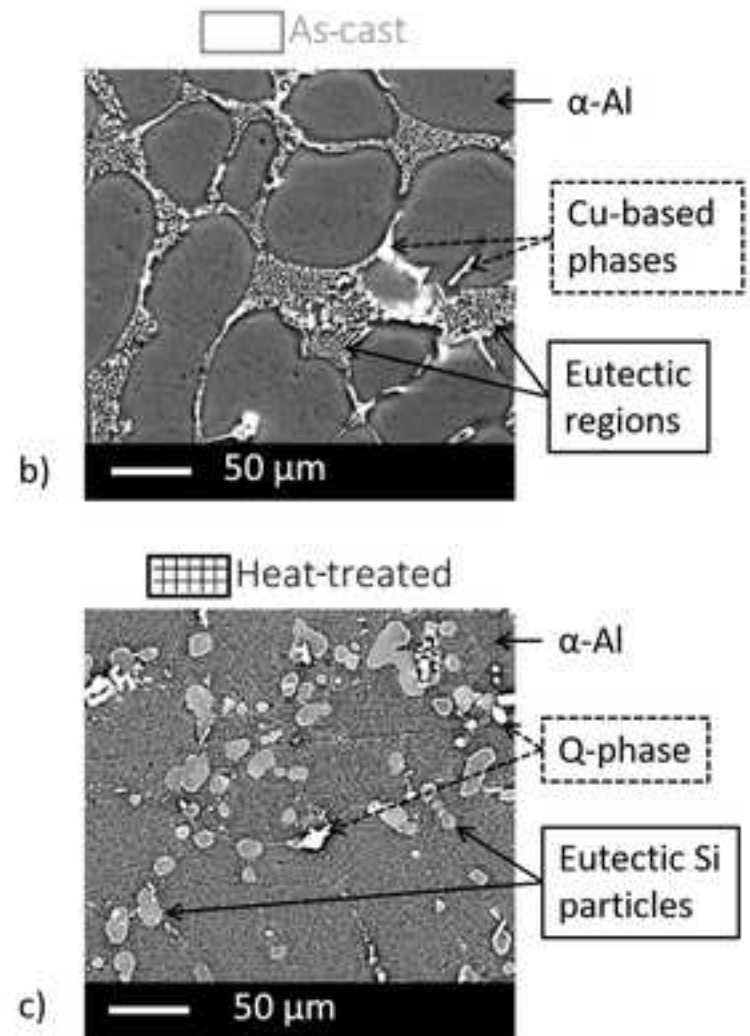
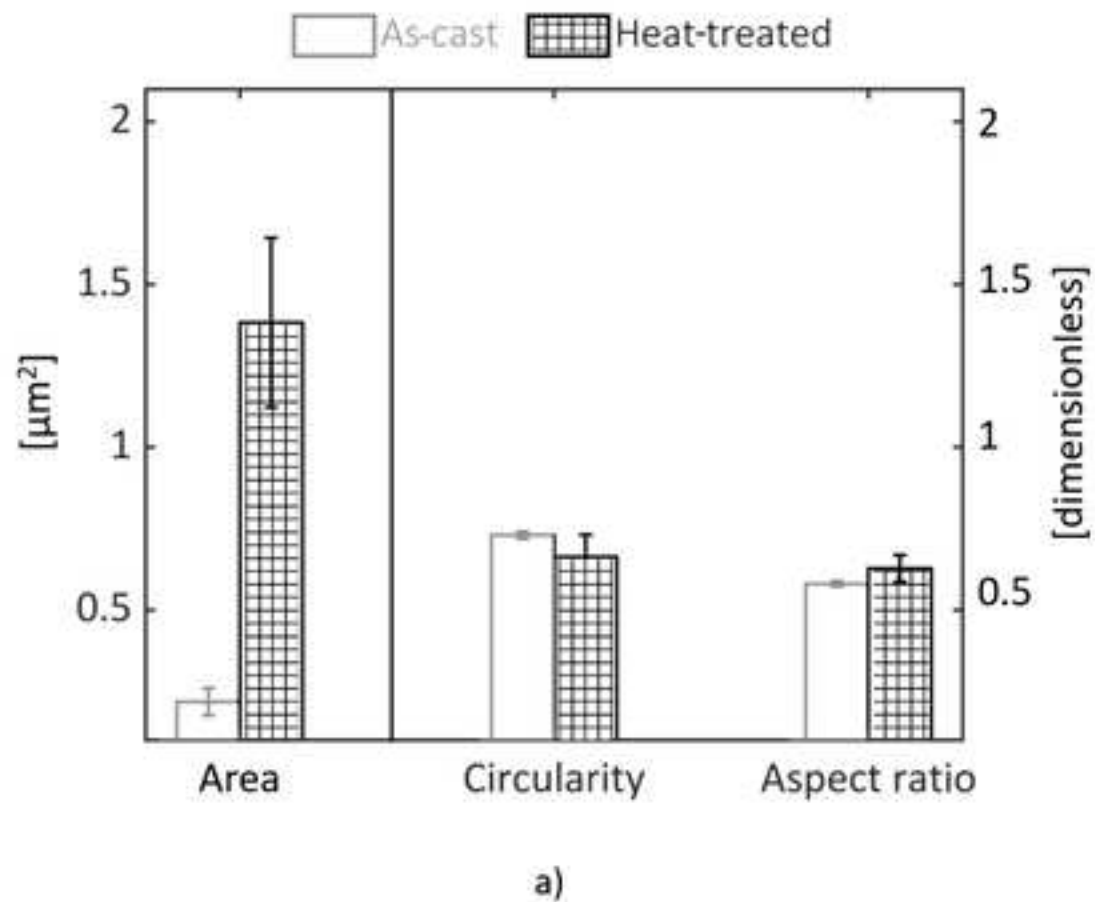
c)

FOV = 300  $\mu$ m x 300  $\mu$ m

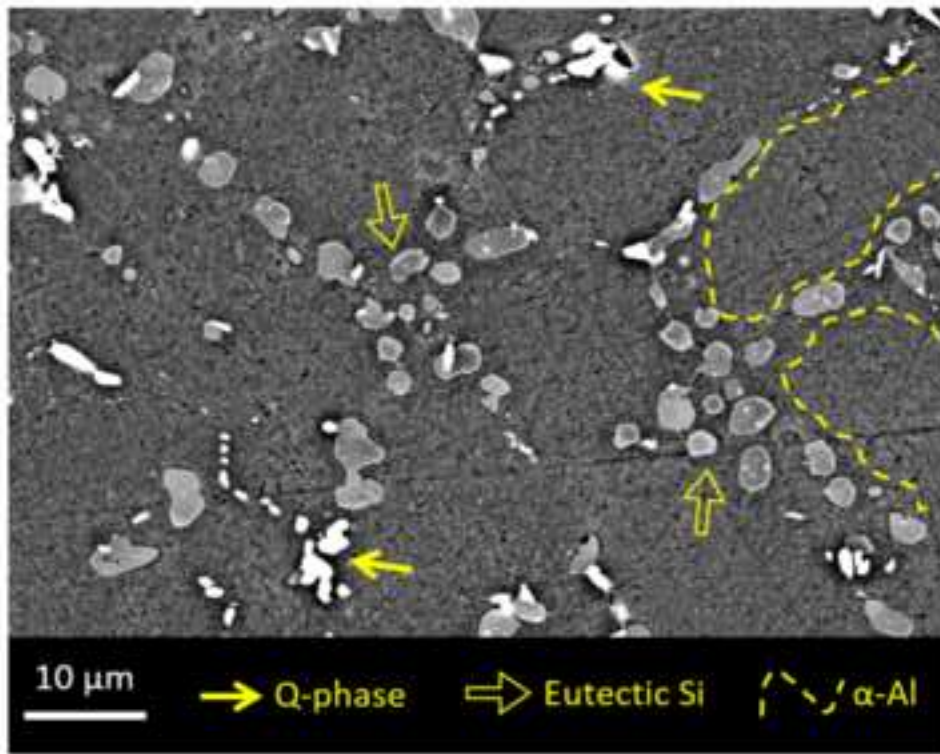


b)

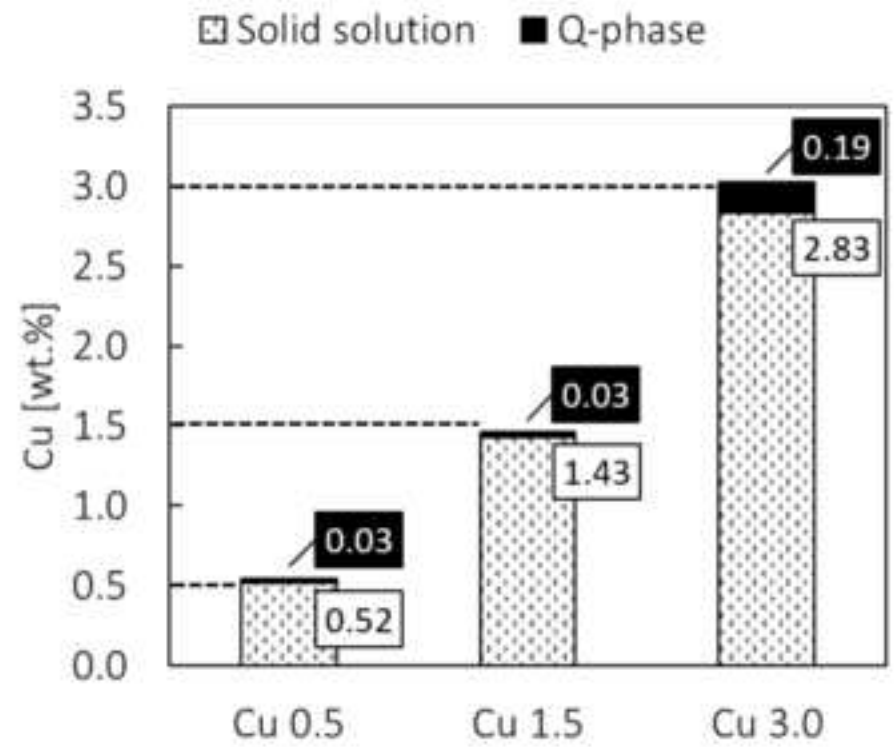




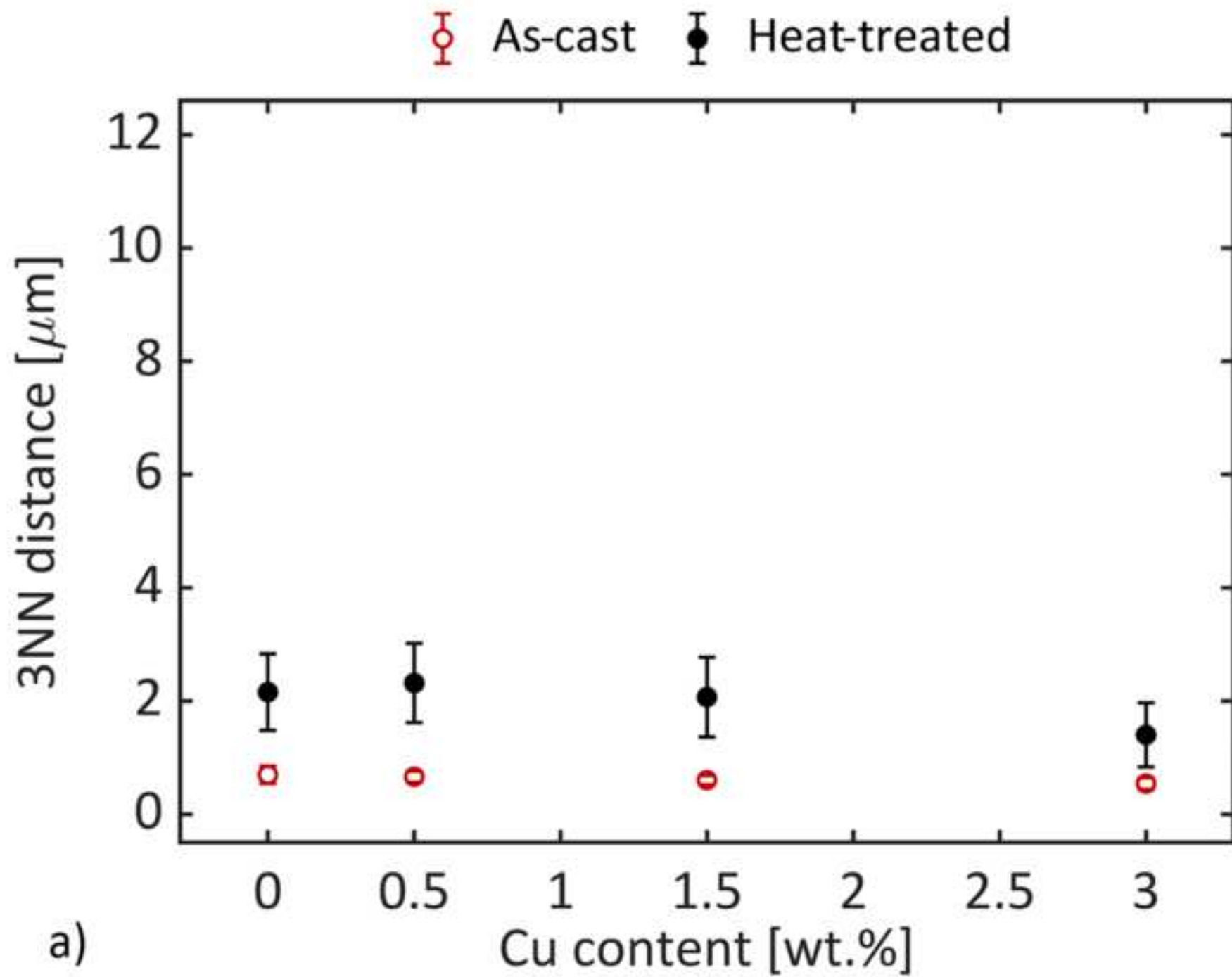




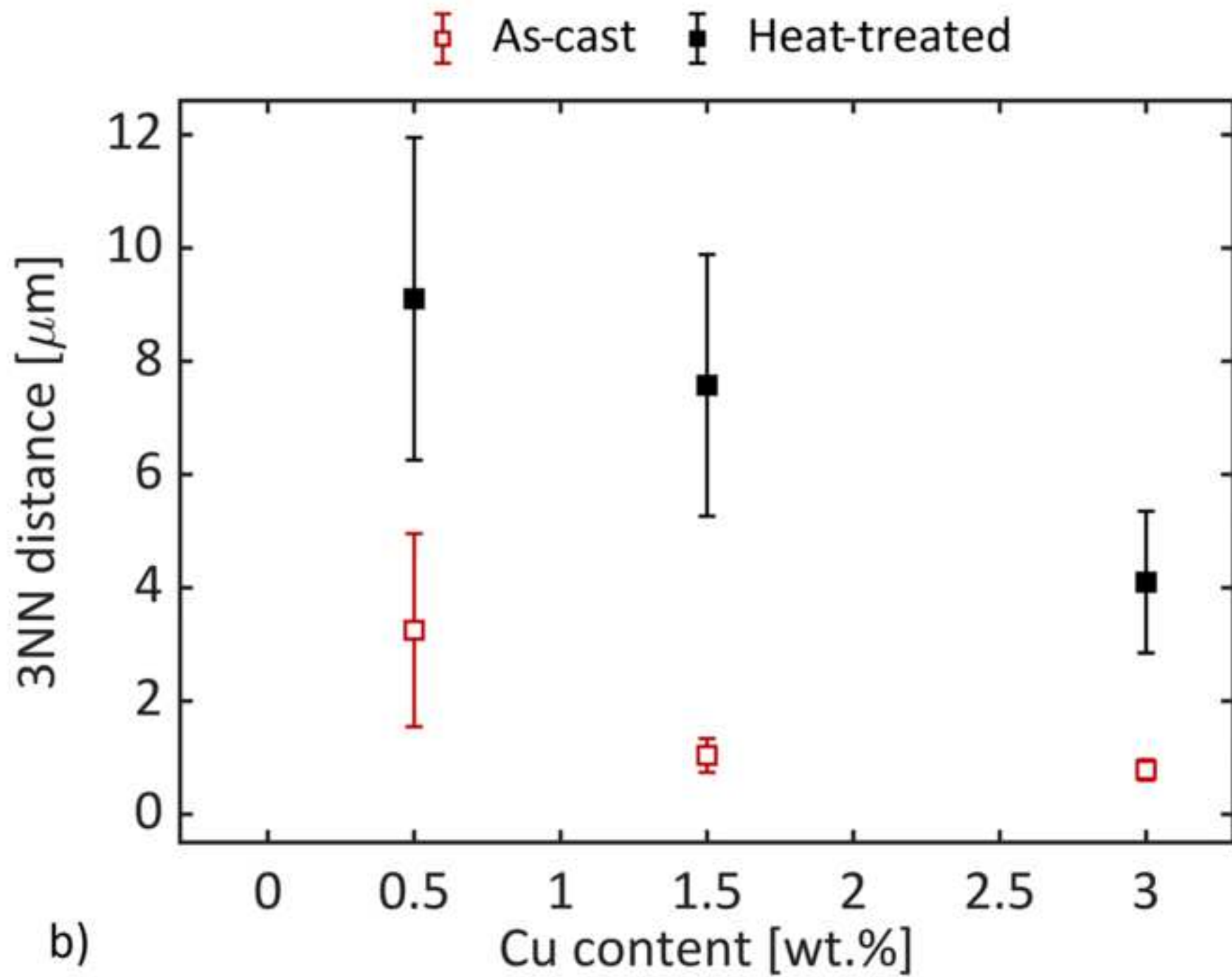
a)



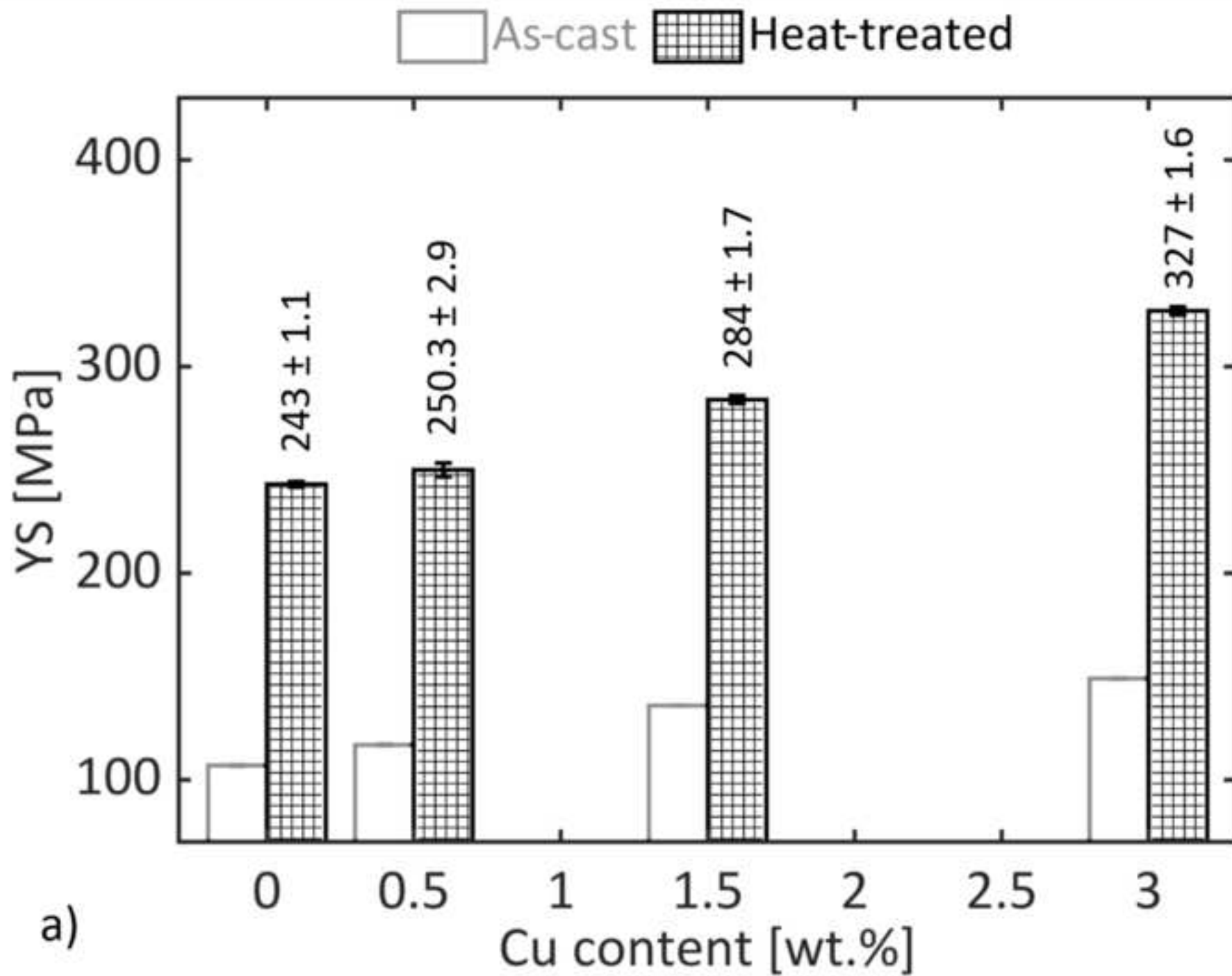
b)

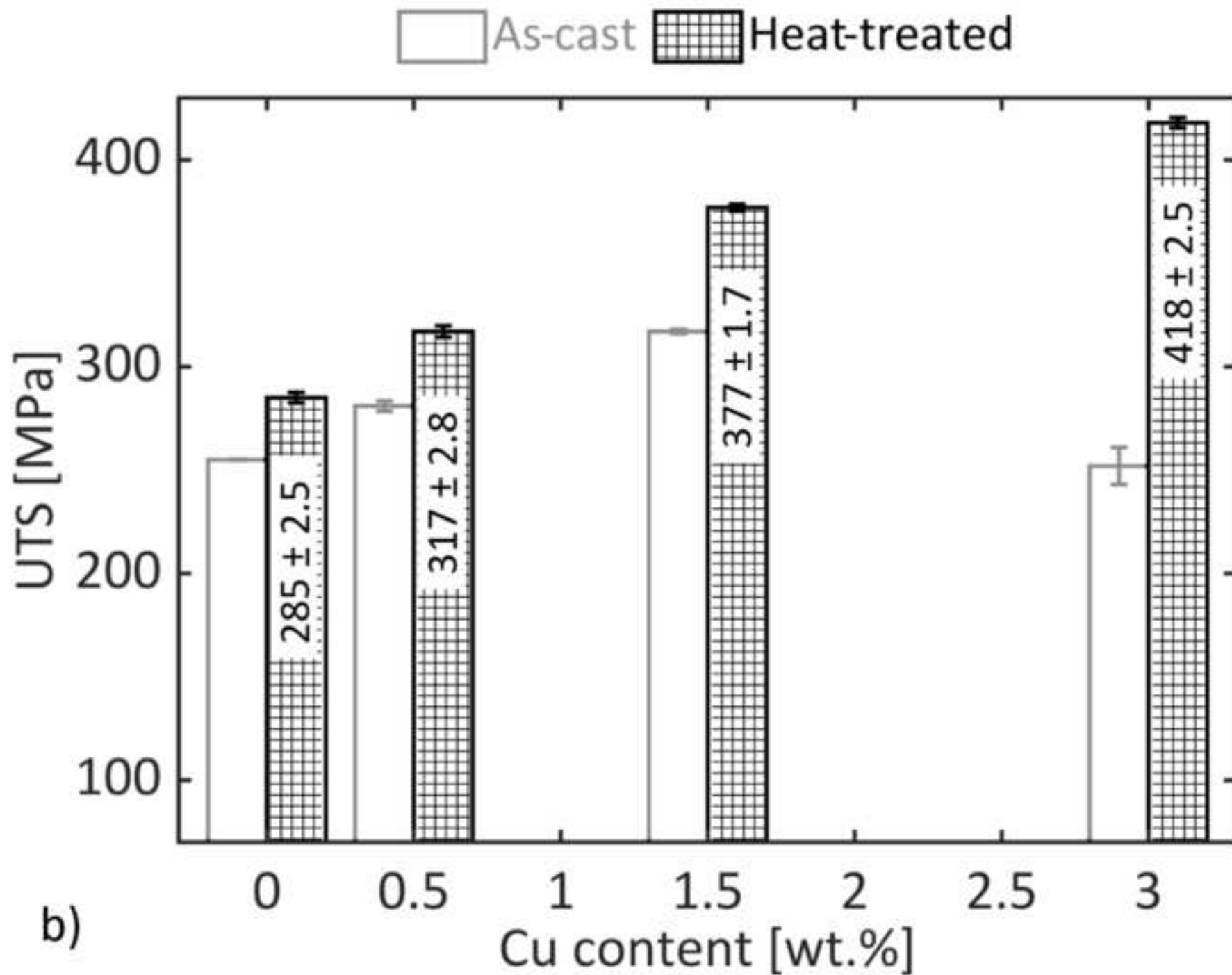


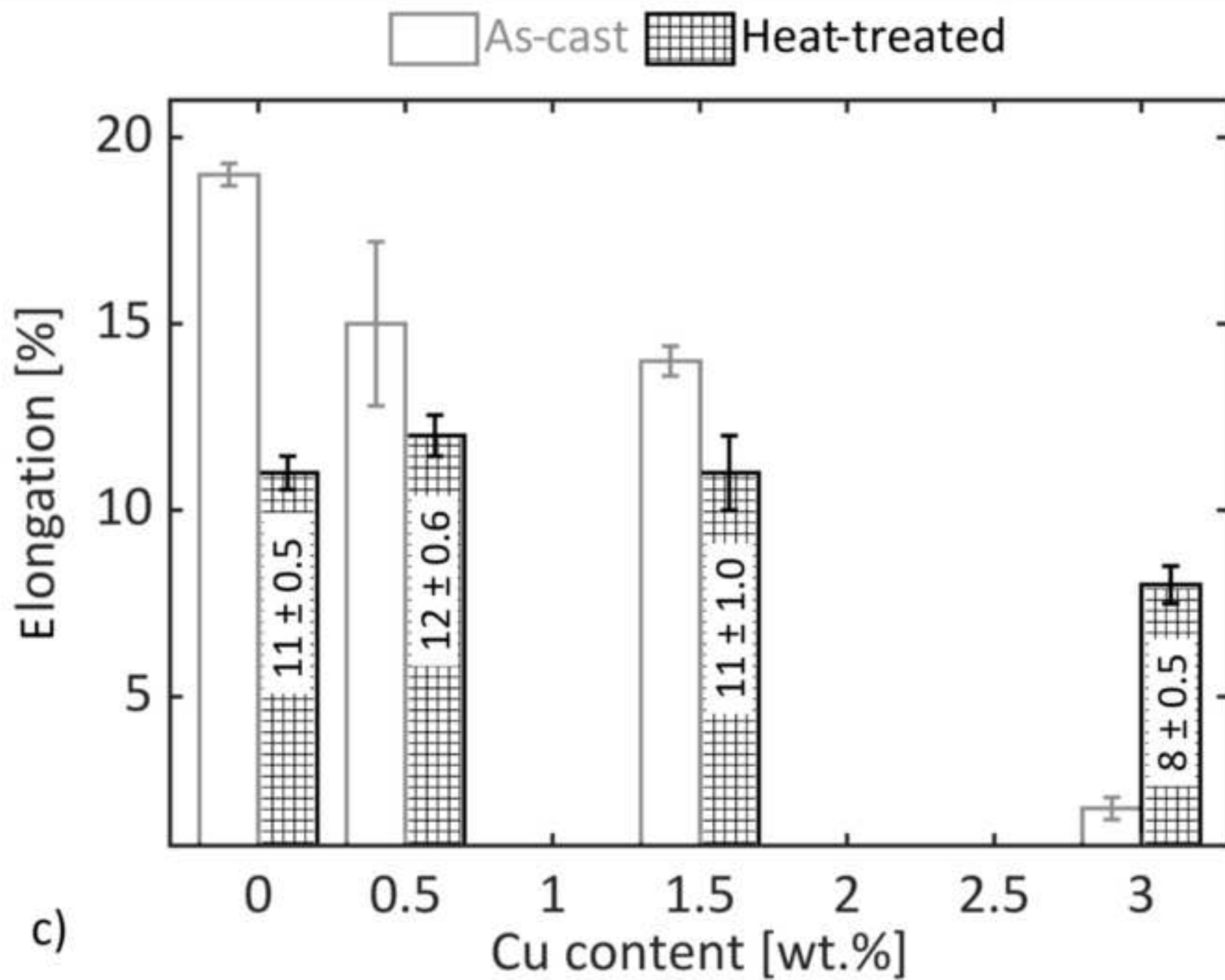
a)

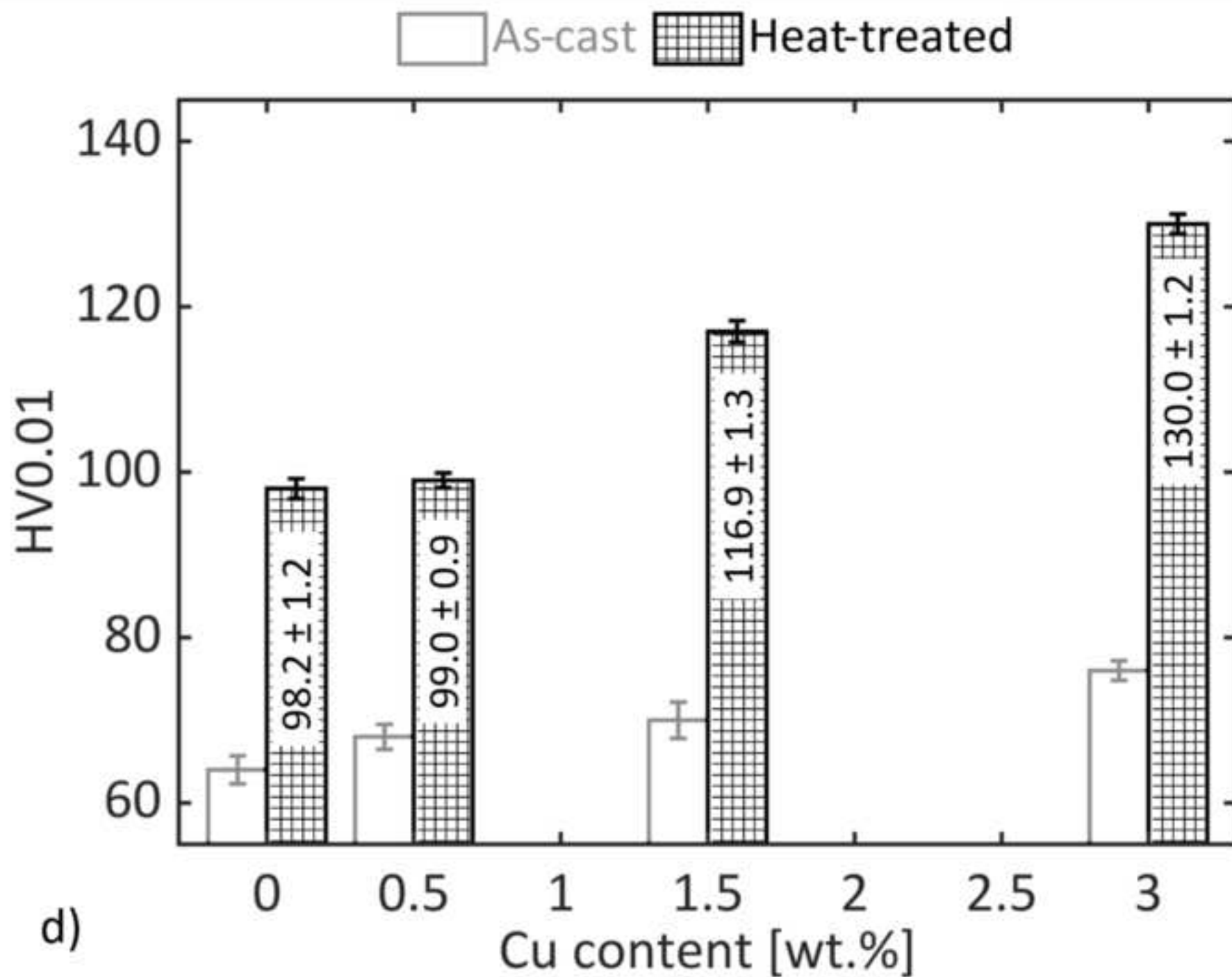


b)

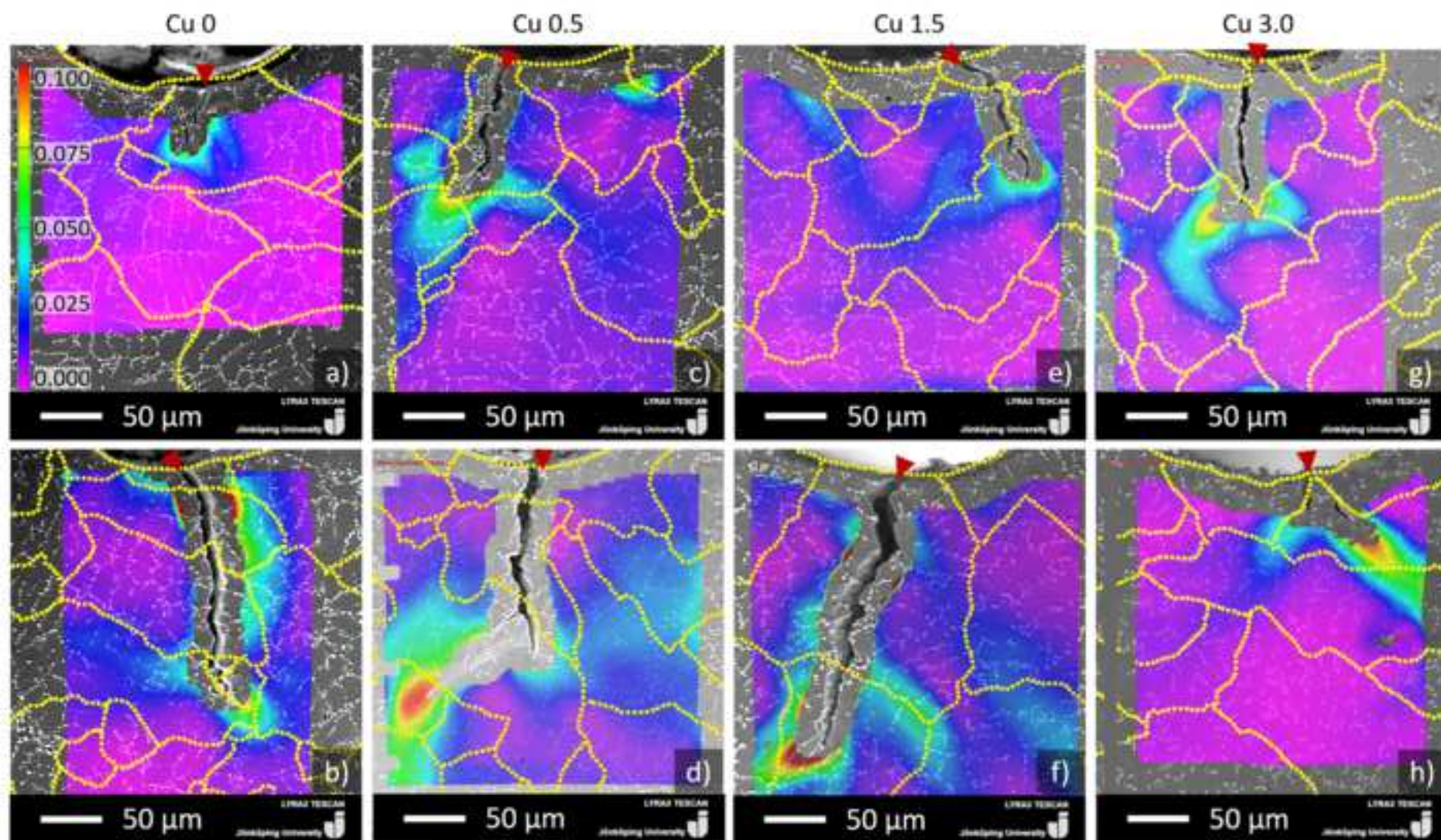






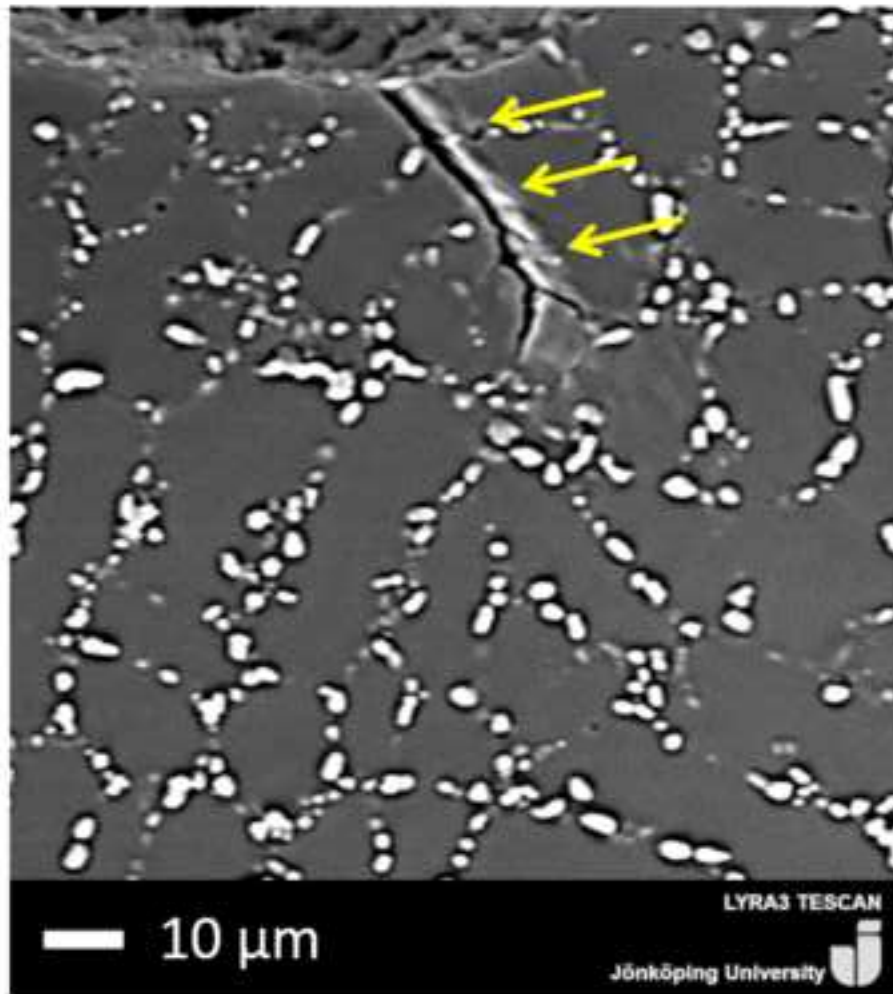






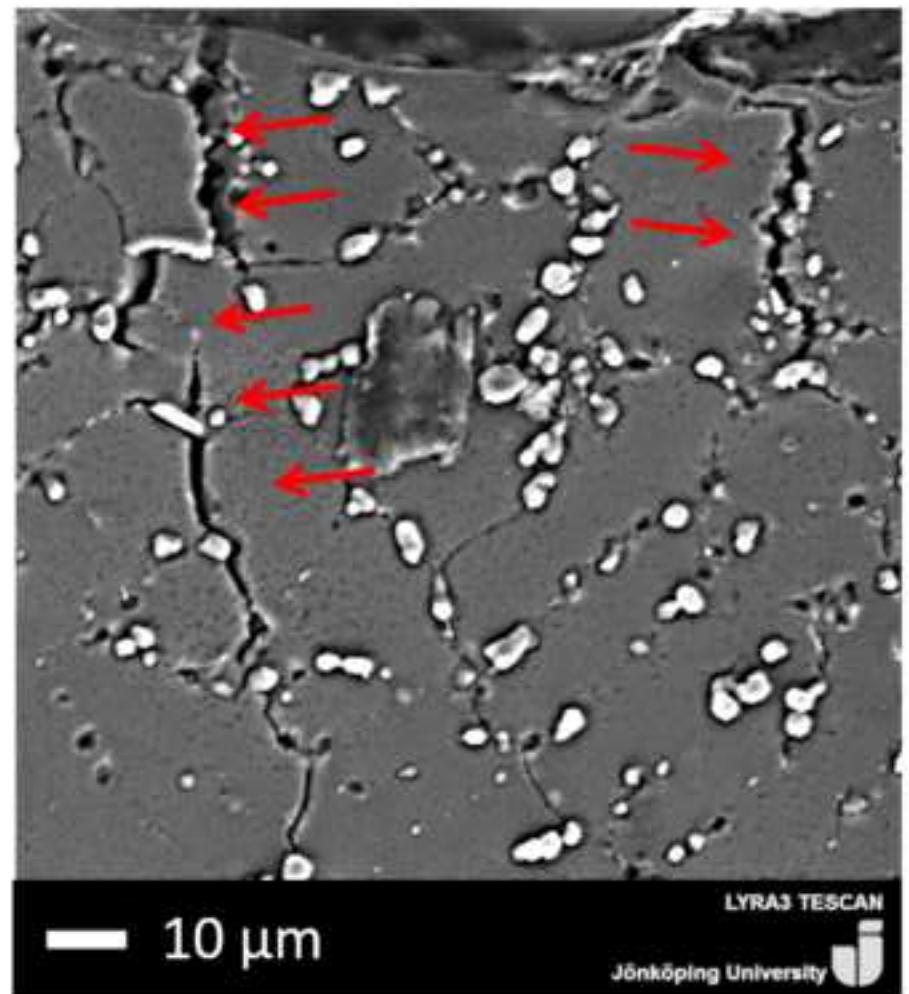


Alloy Cu 0

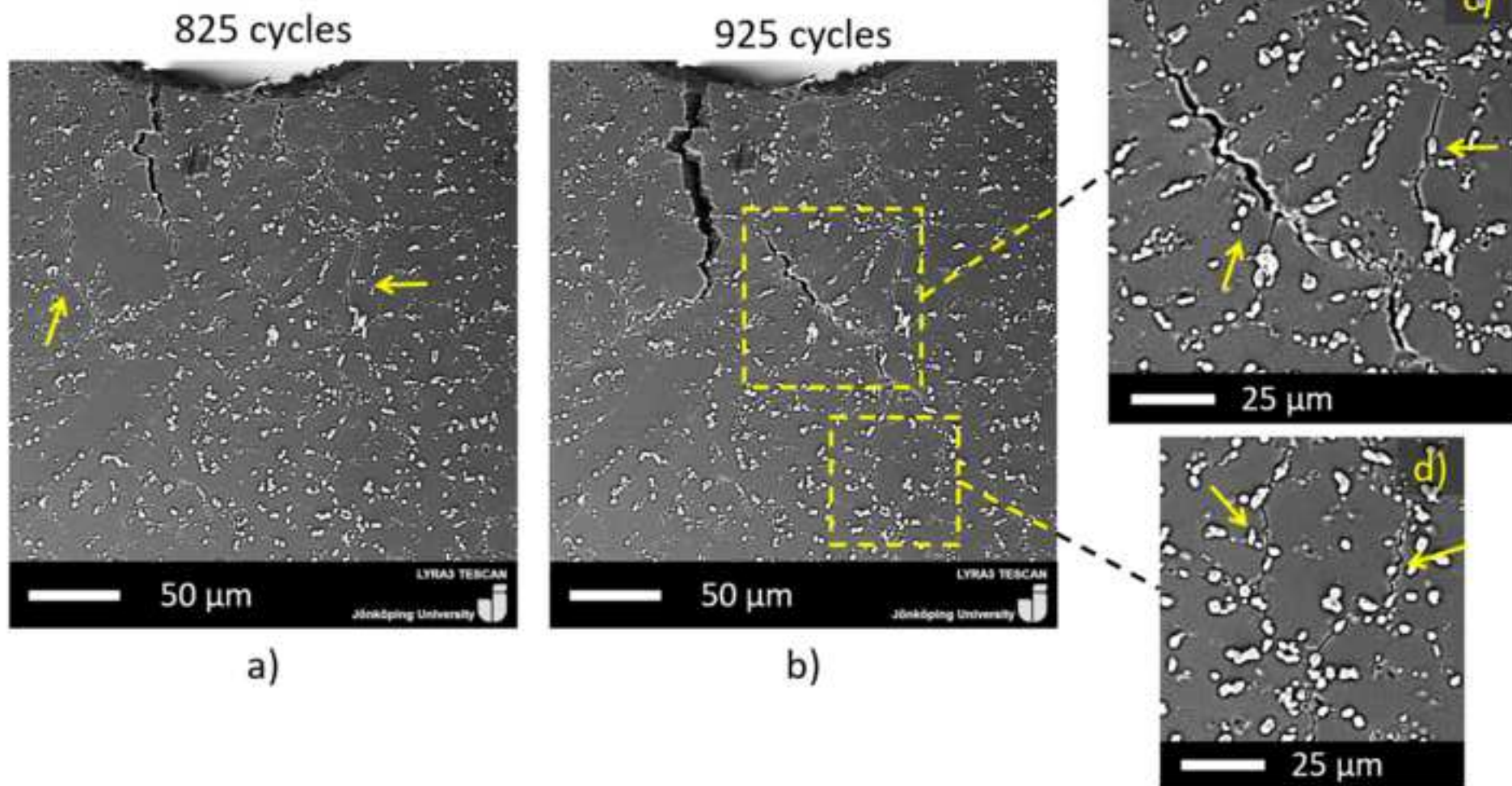


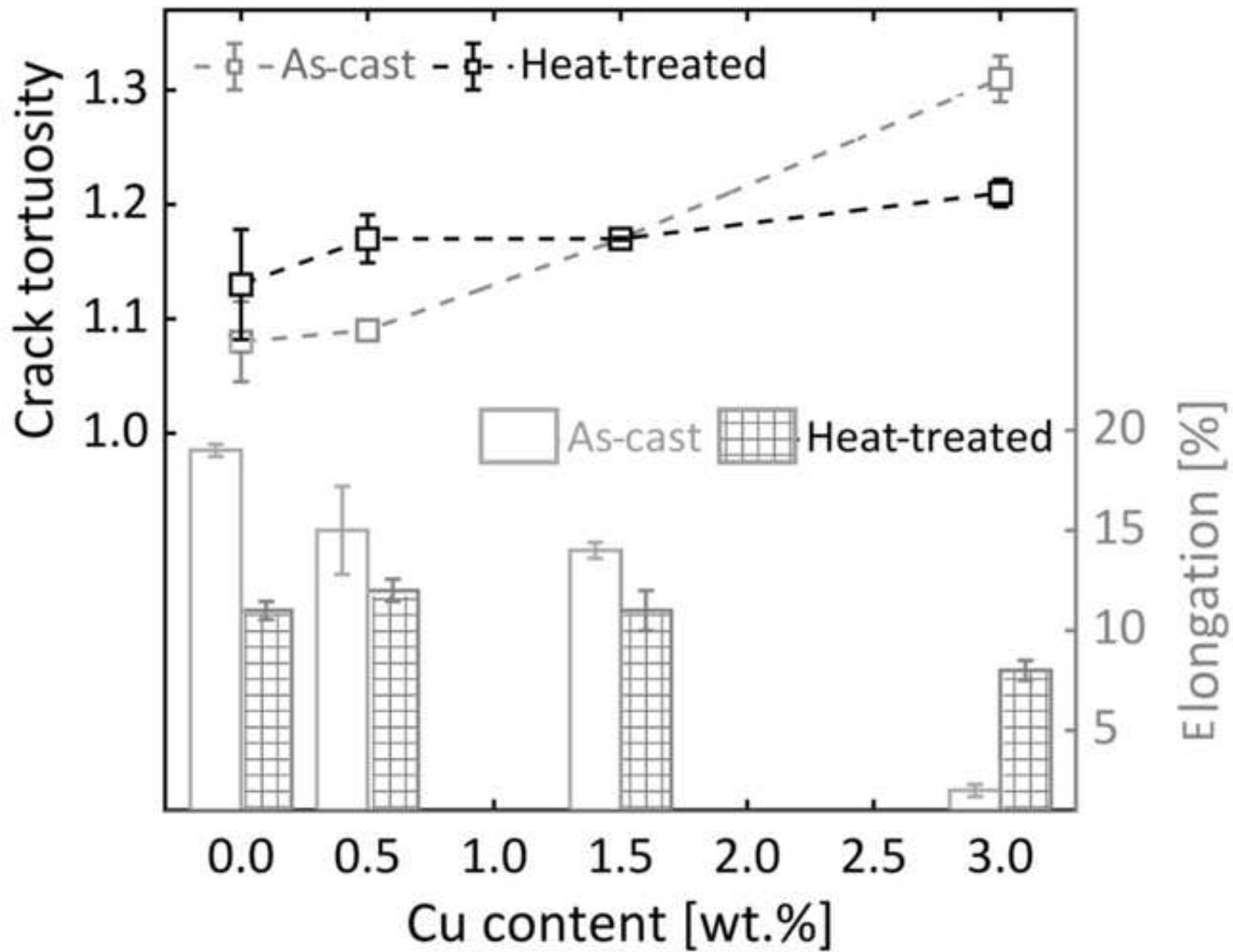
a)

Alloy Cu 3.0

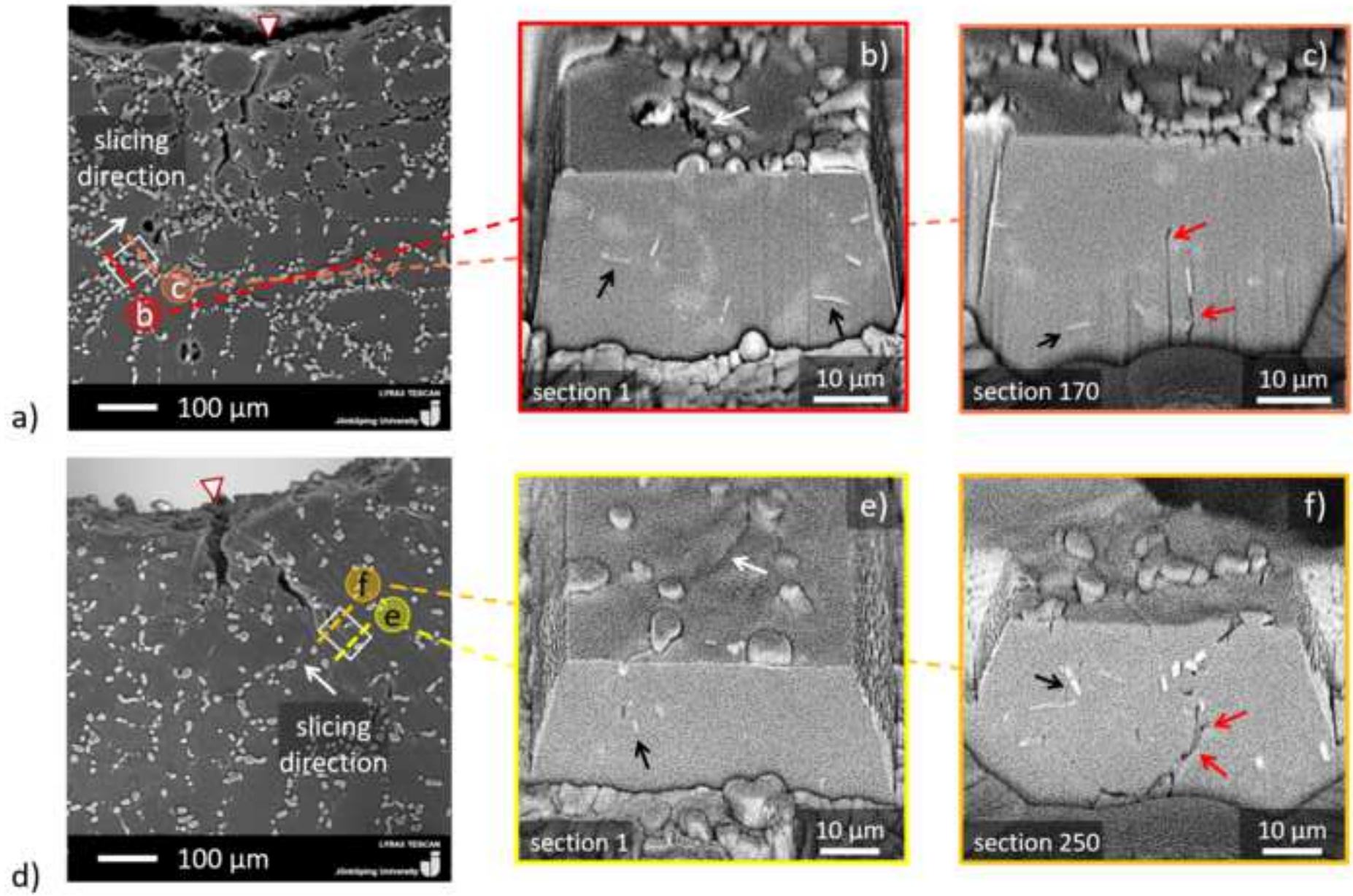


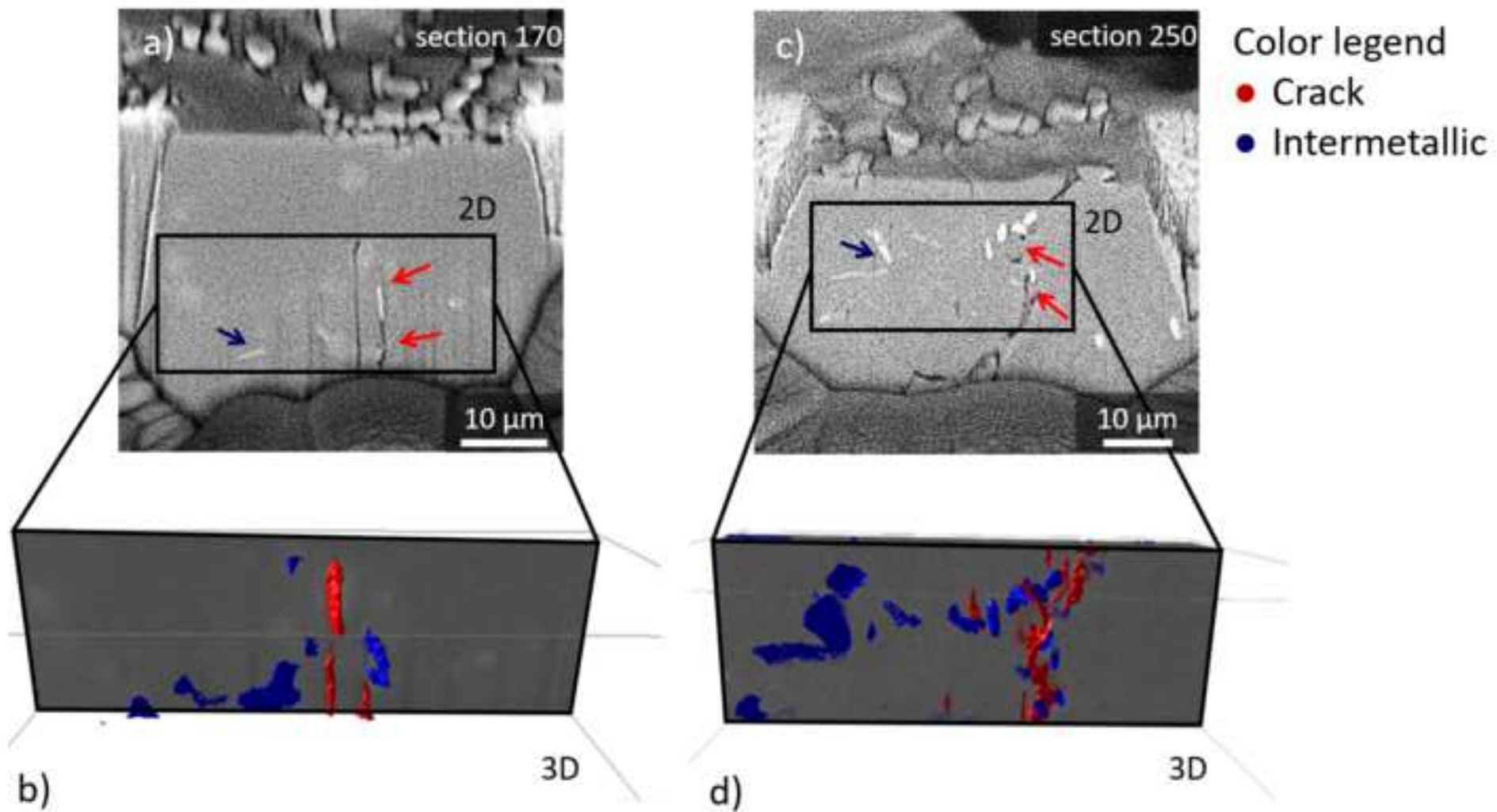
b)



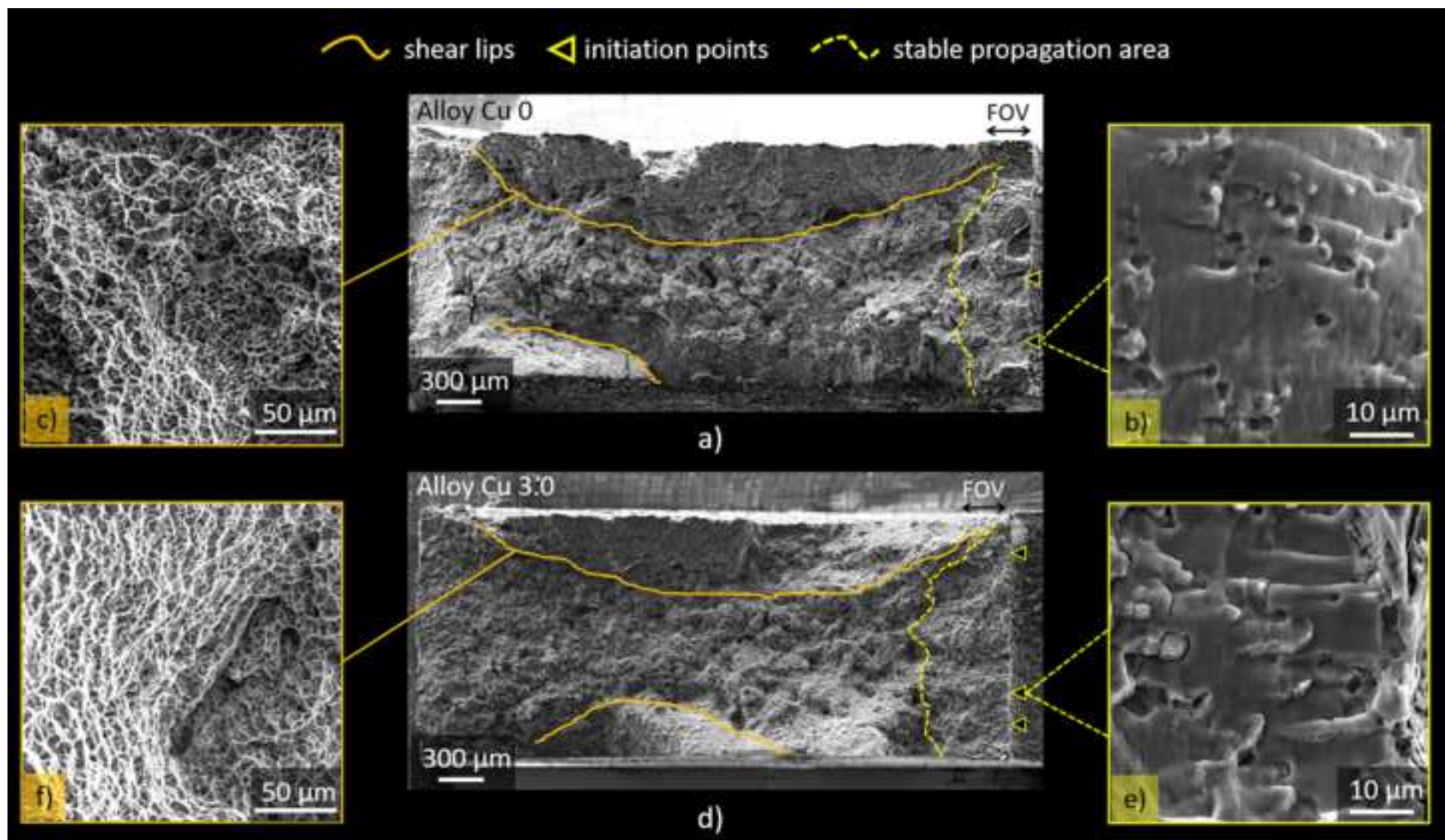














[Click here to access/download](#)

**Video**

**Alloy Cu 0.mp4**





[Click here to access/download](#)

**Video**

**Alloy Cu 3.0.mp4**

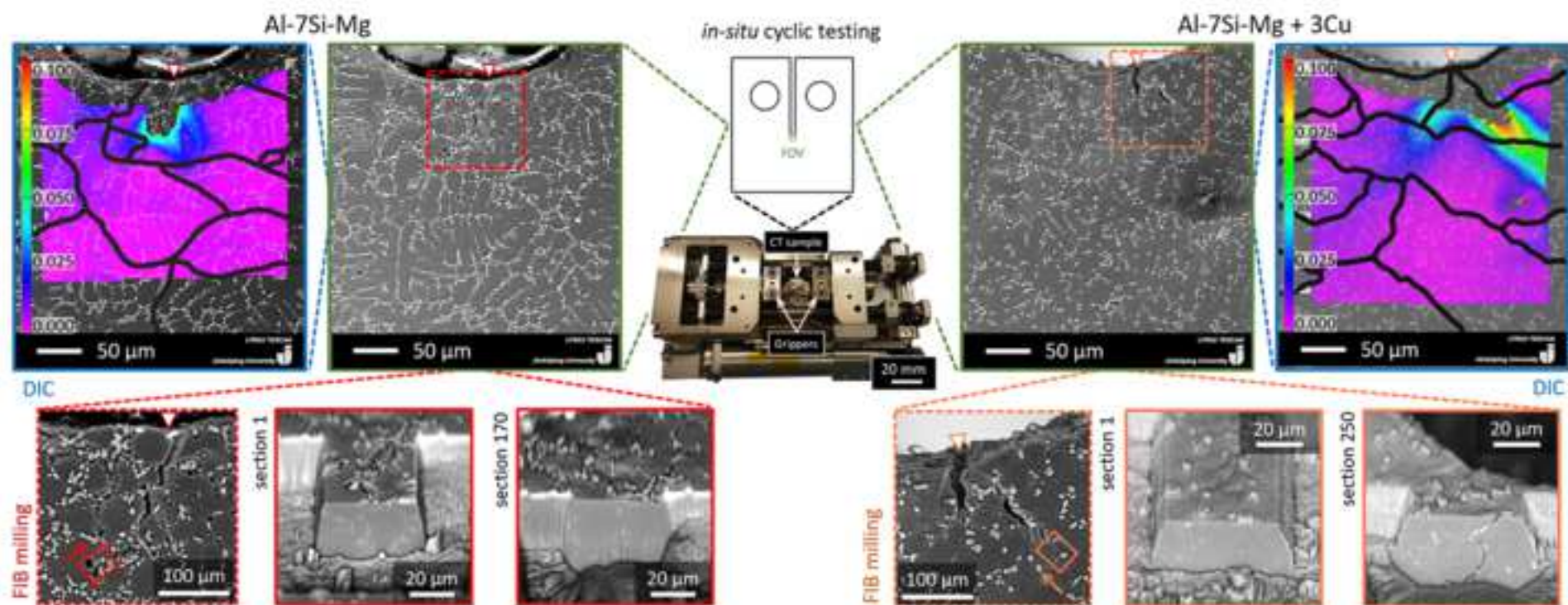




**Declaration of interests**

The authors declare that they have no known competing financial interests or personal relationships that could have appeared to influence the work reported in this paper.

The authors declare the following financial interests/personal relationships which may be considered as potential competing interests:



## **Author contributions**

Toni Bogdanoff: Investigation, Data curation, Writing - Original draft preparation. Lucia Lattanzi: Investigation, Data curation, Writing - Original draft preparation. Mattia Merlin: Supervision, Writing - Reviewing and Editing. Ehsan Ghassemali: Visualization, Methodology, Writing - Reviewing and Editing. Anders E.W. Jarfors: Supervision, Writing - Reviewing and Editing. Salem Seifeddine: Conceptualization, Supervision, Resources, Writing - Reviewing and Editing. All the authors contributed to and read the final manuscript.